META AIRCRAFT FLIGHT DYNAMICS AND CONTROLS

A Dissertation
Presented to
The Academic Faculty

by

Carlos Montalvo

In Partial Fulfillment
of the Requirements for the Degree
DOCTOR OF PHILOSOPHY in the
School of AEROSPACE ENGINEERING

Georgia Institute of Technology

May 2014

META AIRCRAFT FLIGHT DYNAMICS AND CONTROLS

Approved by:

Dr. Mark Costello,Advisor
School of Aerospace Engineering
School of Mechanical Engineering
Georgia Institute of Technology

Dr. William Singhose
School of Mechanical Engineering
Georgia Institute of Technology

Dr. Eric Johnson
School of Aerospace Engineering
Georgia Institute of Technology

Dr. Joseph Schetz
Department of Aerospace and Ocean Engineering
Virginia Polytechnic Institute and State University

Dr. Eric Feron
School of Aerospace Engineering
Georgia Institute of Technology

Date Approved: March 27th,2014

To my growing family...

Acknowledgments

Without the guidance and support of many people, this research would not have been possible. First, I would like to thank my advisor, Dr. Mark Costello. I have been working with Mark since the Fall of 2007. He has been more than a research advisor and has helped form me into a strong researcher and for that I thank him a lot.

I would also like to thank the members of my committee for reviewing this thesis. Without peer review, progress would be limited. I have had the benefit of taking classes with most of the members of my committee so I also thank them for teaching me the basics of aerospace engineering since I started here at Georgia Tech in 2005.

Many of my fellow graduate students at Georgia Tech have provided significant support over the last five years. Emily Leylek, Thomas Herrmann, Edward Scheuermann, Michael Abraham, Eric Beyer, Jonny Rogers, Kyle French, and Sam Zarovy have significantly contributed to my research by either grabbing a drink after work, brainstorming ideas or just sharing conversation in the lab. Without these people surrounding me, I never would have finished. I am especially thankful for being able to work closely with Emily Leylek. It was a fortunate coincidence that much of our research overlapped and we were able to work together through numerous tough research problems. I am also thankful to all other members of the Center for Advanced Machine Mobility.

Lastly, but certainly not least I have to thank my family, my sister Jeanne, her husband Ernesto, my parents and of course my wife Bonnie. Without their continual support, I never would have motivated myself to finish. My parents were incredible role models, having a mother with a PhD in chemistry and a father with a masters in Civil Engineering, this type of career was always in my future. My wife however, has been extremely supportive these last few months even with being pregnant with our first child and now with our three month old daughter. All those nights staying up with me and helping me manage my time are priceless and I will always be grateful. Without this support I may have never finished. My wife becoming pregnant definitely put a fire under me as well to push forward and complete my degree but these are blessings and I

am grateful for them. It's been three months since I defended my thesis and I am now the father of a three month old daughter Elena. Completing this thesis with a newborn was extremely difficult so I have to give even more thanks to my wife again for now taking care of a baby while I finish this document.

To those who read this in the future I say to you that there are only 24 hrs in a day. It is important to decide how you wish to use those hours in the day. I have spent the last few months spending 16 hours a day working on my thesis and I now hope to occupy my time with more of a balance. Perhaps 8 hours of sleep, 8 hours of work, and the other 8 hours spent with my family and friends because without them none of this is worth it.

Contents

List of Tables

List of Figures

List of Abbreviations

UAS	Unmanned Aerial System
UAV	Unmanned Aerial Vehicle
SEAD	Suppression of Enemy Air Defense
CAT	Compound Aircraft Transport
AR	Aerial Refueling
AAR	Autonomous Aerial Refueling
MV	Machine Vision
DFA	Distributed Flight Array
6DOF	Six-Degrees of Freedom
CG	Center of Gravity
SE	Surface Element
LED	Light Emitting Diode
WRF	Weather Research and Forecasting
CBL	Convective Boundary Layer
LES	Large Eddy Simulation
PID	Proportional Integral Derivative Control
MPC	Model Predictive Control
NMPC	Nonlinear Model Predictive Control
MILP	Mixed Integer Linear Programming
MRAC	Model Reference Adaptive Controller
GPS	Global Positioning System
IMU	Inertial Measurement Unit
NN	Neural Networks

ICE	Innovative Control Effectors
VISNAV	Vision Based Navigation Sensor
SOI	Sphere of Influence
CFD	Computational Fluid Dynamics
L/D	Lift to Drag Ratio
AOA	Angle of Attack

List of Symbols

x_i, y_i, z_i	components of the mass center position vector in the inertial frame of aircraft i (m)
ϕ_i, θ_i, ψ_i	Euler roll,pitch, and yaw of aircraft i (rad)
u_i, v_i, w_i	components of the mass center velocity vector in the body frame of aircraft i (m/s)
p_i, q_i, r_i	components of the mass center angular velocity vector in the body frame of aircraft i (rad/s)
$\vec{r}_{A\to B}$	position vector from a generic point A to a generic point B(m)
$\vec{V}_{A/B}$	velocity vector of a generic point A with respect to frame B (m/s)
$\mathbf{T}_{AB}$	generic transformation matrix rotating a vector from the frame B to frame A
$\mathbf{H}_i$	relationship matrix of Euler angle derivatives to body angular velocity components of aircraft i
m_i	mass of aircraft i (kg)
I_i	moment of inertia matrix of aircraft i taken about the mass center in the body frame($kg - m^2$)
X_i, Y_i, Z_i	components of the total force applied to aircraft i in body frame(N)
L_i, M_i, N_i	components of the total moment applied to aircraft i in body frame(N-m)
X_{Wi}, Y_{Wi}, Z_{Wi}	total weight force applied to aircraft i (N)
X_{Ai}, Y_{Ai}, Z_{Ai}	total aerodynamic force applied to aircraft i (N)
X_{Mi}, Y_{Mi}, Z_{Mi}	total magnetic force applied to aircraft i(N)
X_{Ci}, Y_{Ci}, Z_{Ci}	total contact force applied to aircraft i(N)
L_{Ai}, M_{Ai}, N_{Ai}	total aerodynamic moment applied to aircraft i (N-m)
L_{Mi}, M_{Mi}, N_{Mi}	total magnetic moment applied to aircraft i(N-m)
L_{Ci}, M_{Ci}, N_{Ci}	total contact moment applied to aircraft i(N-m)
g	gravitational constant on Earth (m/s^2)
X_{Ei}, Y_{Ei}, Z_{Ei}	total aerodynamic force applied to aircraft i of all lifting surface elements(N)
X_{Fi}, Y_{Fi}, Z_{Fi}	total aerodynamic force applied to aircraft i of fuselage(N)
N	Number of main wing lifting surface elements

ρ	atmospheric density(kg/m^3)
S_i	reference area of wing on aircraft i (m^2)
b_i	Wingspan of aircraft i (m)
c_i	mean chord of wing on aircraft i (m)
α	Angle of attack (rad)
β	Slideslip angle (rad)
C_L, C_D	Lift and Drag coefficients
V_x, V_y, V_z	components of the atmospheric winds in the inertial frame(m/s)
u_{In}, v_{In}, w_{In}	components of the induced velocity caused by a horseshoe vortex in the local element frame (m/s)
$\delta_t, \delta_a, \delta_r, \delta_e$	thrust, aileron, rudder, and elevator control inputs(rad)
Γ_n	strength of vortex filament at panel n
$W_{AB,C}$	Induced velocity at point C of a vortex filament from point A to point B (m/s)
μ_0	permeability of free space($kg\ m/(A^2 s^2)$)
$\vec{M}_A$	magnetization vector of a generic magnet centered at point(A), $kg/(A\ s^2)$
$\vec{H}_{ext}$	magnetic field vector(A/m)
NW	number of magnetic elements
a_i, b_i, c_i	half size of a magnet i(m)
J	magnetization strength of magnet($kg/(A\ s^2)$)
$\vec{F}_{Mi}, \vec{T}_{Mi}$	Total force and torque applied to a magnet Mi(N,N-m)
F_{max}	maximum applied force of magnet when touching (N)
$S_B(\vec{r})$	skew symmetric matrix operator on a vector expressed in the body frame.
	This is equivalent to a cross product
$k_{1t}, k_{2t}, c_{1t}, c_{2t}$	tangential spring and damper coefficients($N/m, N\ s/m$)
$k_{1n}, k_{2n}, c_{1n}, c_{2n}$	normal spring and damper coefficients($N/m, N\ s/m$)
$\vec{u}_j$	absolute velocity of jth contact point(m/s)
$\vec{w}_j$	absolute velocity of jth surface element(m/s)

$\vec{s}_{1n}, \vec{s}_{1t}$	normal and tangential spring distance vectors associated with body vertices(m)
$\vec{s}_{2n}, \vec{s}_{2t}$	normal and tangential spring distance vectors associated with leader contact cube(m)
$\vec{F}_{nj}, \vec{F}_{tj}$	normal and tangential force component at jth contact point(N)
NC	Number of contact points for soft contact model
Θ	3-Dimensional Dryden turbulence spectrum
$\vec{\Omega}$	The wave vector in Dryden turbulence spectrum
E	Energy density function of Dryden turbulence spectrum
NW	Number of waves used in numerical realization of Dryden turbulence spectrum
K_p, K_d, K_I	proportional, derivative, and integral control gains
η	lead distance used for model following(m)
A, B, C	Linear matrices used in Model predictive controller
K_{CA}, K_{CAB}	Model predictive control matrices
Q, R	Model predictive control gain matrices
Δt_d	discrete timestep used to discretize non-linear system(sec)
Δt	timestep used in simulation(sec)
f_x	frequency of static gust(rad/m)

Summary

The field of mobile robotic systems has become a rich area of research and design. These systems can navigate difficult terrain using multiple actuators with conventional ambulation, by hopping, jumping, or for aerial vehicles, using flapping wings, propellers, or engines to maintain aerial flight. Unmanned Aerial Systems (UAS) have been used extensively in both military and civilian applications such as reconnaissance or search and rescue missions. For air vehicles, range and endurance is a crucial design parameter as it governs which missions can be performed by a particular vehicle. In addition, when considering the presence of external disturbances such as atmospheric winds, these missions can be even more challenging. A meta aircraft is an aircraft composed of smaller individual aircraft connected together through a similar connection mechanism that can potentially transfer power, loads, or information. Meta aircraft technologies is one area of research that can increase range and endurance by taking advantage of an increase in Lift to Drag ratio (L/D).

This dissertation examines meta aircraft flight dynamics and controls for a variety of different configurations. First, the dynamics of meta aircraft systems are explored with a focus on the changes in the aircraft flight dynamic modes and flexible modes of the system. Specifically, when aircraft are connected, basic flight dynamic modes such as the phugoid, short period, dutch roll, spiral and roll modes change as a function of the number of connected aircraft. In addition, connected aircraft exhibit complex flexible modes that change based on the characteristics of the connection joint and the number of connected aircraft. For example, the longitudinal modes of the system are constant when aircraft are connected wing tip to wing tip. When aircraft are connected tip to tail, the longitudinal modes become over damped and even unstable. The lateral modes change in any type of configuration. Furthermore, connected aircraft exhibit flapping, lead lag, and twisting modes.

Second, the connection dynamics are explored for meta aircraft where the vehicles are connected wing tip to wing tip using passive magnets with a particular focus on modeling the connection event between aircraft in a practical environment. It is found that a multi-stage connection control law with position and velocity feedback from GPS and connection point image feedback from a camera yields adequate connection

performance in the presence of realistic sensor errors and atmospheric winds. Furthermore, atmospheric winds with low frequency gusts at the intensity normally found in a realistic environment pose the most significant threat to the success of connection. The frequency content of the atmospheric disturbance is an important variable to determine success of connection. This system is relatively insensitive to axial wind disturbances, mildly sensitive to lateral wind disturbances and very sensitive to vertical wind disturbances. Flying faster can mitigate maximum angle of attack perturbation and increase connection rates. Finally, the geometry of magnets that create the connection force field can alter connection rates. Square magnets create a connection force field that leads to the highest connection rates. Furthermore, creating an actuator that can propel the magnet from one wing tip to another can increase percent connection rates by 15%.

Finally, the performance of a generic meta aircraft system is explored. Using a simplified rigid body model to approximate any meta aircraft configuration adequate control is achieved in the presence of realistic winds. A rigid body model is used to alter inner and outer loop configuration dependent gains and an optimization routine is used to allocate individual control surfaces on individual aircraft. Provided each aircraft can maintain inner loop pitch and roll commands, control is shown to be robust to atmospheric winds for different configurations. Using this controller, overall performance is studied. First tracking performance is investigated for different meta aircraft configurations. In addition, the aerodynamic benefit of different configurations are investigated. Wing tip to wing tip connected flight provides the most benefit in terms of average increased Lift to Drag ratio while tip to tail configurations drop the Lift to Drag ratio as trailing aircraft fly in the downwash of the leading aircraft. As more aircraft are connected the benefit or loss is increased.

1 Introduction

Mobile robotic systems are becoming a more and more common part of society. These systems are envisioned to perform a wide variety of tasks from ground vehicles that can automatically traverse a route to autonomous aircraft that can robotically take-off, fly a mission and land. Modular robots, which consist of identical building blocks connected in a variety of different configurations, have the ability to accomplish new missions, adapt to a changing environment or recover from damage or failures[44–48]. A modular aerial robot, or meta aircraft is a large aircraft composed of individual smaller aircraft where the connection joint is envisioned to be able to transfer power, information and/or aircraft loads, while each individual aircraft is capable of flying independently. These aircraft are designed to attach and detach in flight using a wing tip to wing tip, tip to tail or a lattice structure configuration as shown in Figure 1. By allowing highly specialized vehicles

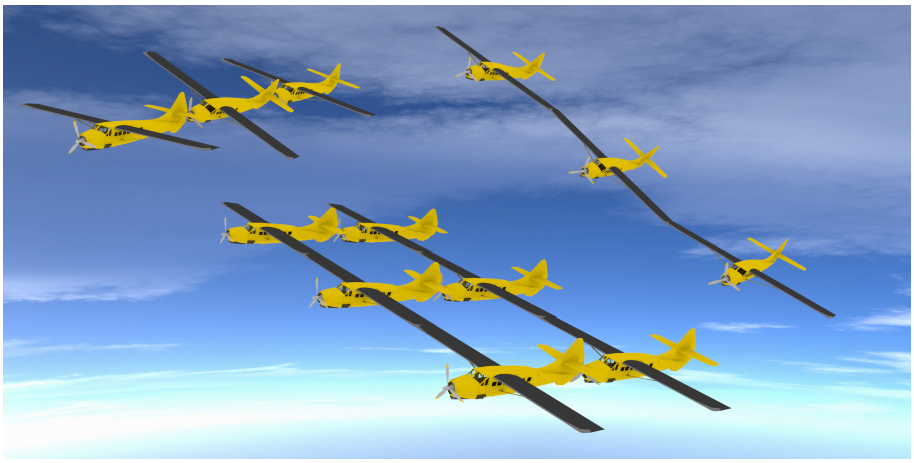

Figure 1: Different Meta Aircraft Configurations

to connect in flight, a meta aircraft could conceivably fly to a target area, break apart, perform multiple missions, and reconnect to fly home. If a search and rescue mission is conducted, search vehicles fixed with radar equipment scanning a certain region could connect with other aircraft fixed with weaponry to defend against any hostile entity while further connecting with more aircraft that are designed to carry most of the fuel/power supply. Figure 2 shows a typical mission profile that a meta aircraft could perform.

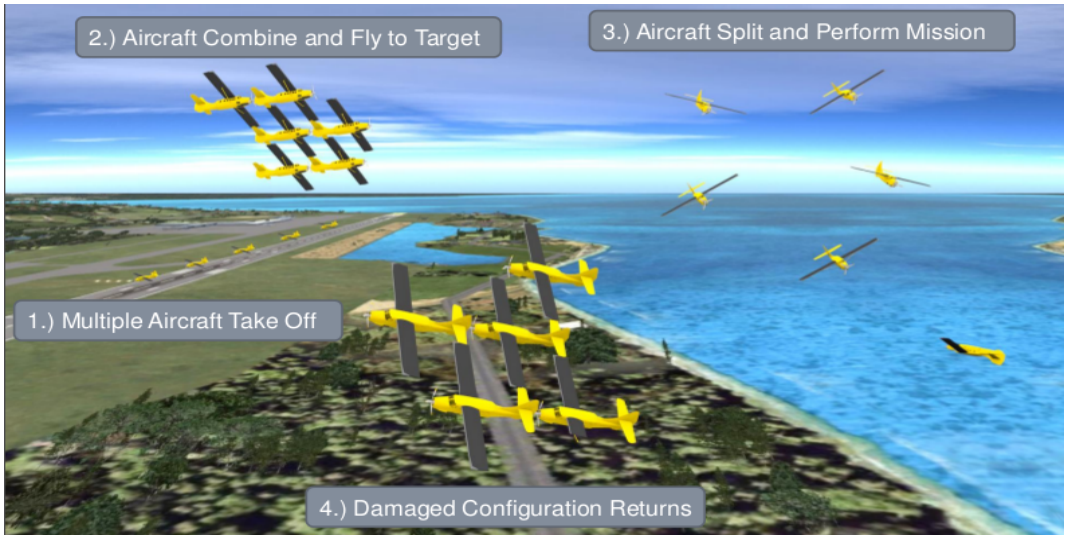

Figure 2: Typical Mission Profile of a Meta Aircraft

In addition to an increase in adaptability, connected aircraft have the benefit of reducing the effect of wing tip vortices thus increasing L/D which directly impacts range and endurance. Meta aircraft also increases the effective mass of the aircraft to reduce the sensitivity of atmospheric disturbances. In the past, these types of aircraft have been very simple, on the order of 2 or 3 aircraft or been permanently connected such as Compound Aircraft Transport (CAT)[50−54].

Range and endurance is a key design variable for UAVs whose primary task is to maintain perpetual flight. Numerous research programs have been developed to increase range and endurance of UAVs from formation flight[7−17] to autonomous aerial refueling[18−23]. Both of these methods require very precise navigation techniques to accurately stay either in the wake of the leading vehicle or interface with the probe. Precise path planning techniques have been created to try and minimize failure rates of these missions[29−36] while camera sensing technologies have been created to decrease sensor inaccuracies for autonomous refueling missions[24−27].

With limited real estate on board the aircraft, trade offs must be considered when designing an aircraft to either add more sensors, fuel capacity, or other major design features. With these trade offs comes a lack of adaptation for aircraft. For challenging missions, highly specialized robotic vehicles are needed for successful

operation. In suppression of enemy air defense missions (SEAD) missions, two types of aircraft are needed. One for disrupting air defenses and the other to perform the actual mission[1]. Both of these aircraft are highly specialized. Creation of specialized aircraft for a narrow task or mission can be both expensive and time-consuming.

Conventional aircraft also have the problem of recovering from in flight damage that can come from hostile weaponry or atmospheric disturbances. Small, lighter aircraft, which usually fly slower, have the added benefit of being more maneuverable while at the same time increasing their sensitivity to gusts. Large gusts create large angle of attack perturbations that wreak havoc on trajectory control and overall performance. Work has been accomplished to try and reject these atmospheric disturbances; however, knowledge of the type of disturbance must be known a priori[40−43].

Meta aircraft is a technology that can be used to increase range, endurance and adaptability while decreasing wind gust sensitivity. This dissertation focuses on flight dynamics, control, and connection mechanics of meta aircraft for a variety of different configurations. The following subsections provide a comprehensive overview on research performed on the areas related to meta aircraft flight starting with the related field of modular robots discussed in Section 1.1 to the related problem of aerial refueling discussed in Section 1.4.

1.1 Modular Robots

Modular, reconfigurable robots, as the name implies, is a set of robots that can reconfigure themselves into a variety of different shapes to accomplish different mission types. These robots could morph into a snake like creature to navigate a small opening using a snake like motion for locomotion. The robot could then reconfigure to morph into a hand like structure and pick up an object. These robots outperform other robots in that they can accomplish more than just 1 type of mission. Still, with this added ability comes the challenge of both modeling and control of this system. The control algorithms needed must be able to adapt to a completely different system when new building blocks are added while also having the ability to reconfigure the robot.

The control and simulation of multibody systems is not new. Wendlant's dissertation in 1997 provides a

comprehensive study of the control and simulation of multibody systems to that date[80]. The basic control structure used is a recursive multibody dynamics algorithm. After creating a simple reduced order model, the joint torques are computed to control the degrees of freedom of the entire system.

Yim, Zhang and Duff created a modular robot called the PolyBot, pictured in Figure 3, with simulation results dating as far back as 1994. This robot is made of a simple square building block with a single actuator and connection interface[46]. This robot can connect together in any configuration along this connection interface and completely reconfigure itself to adapt to a new mission.

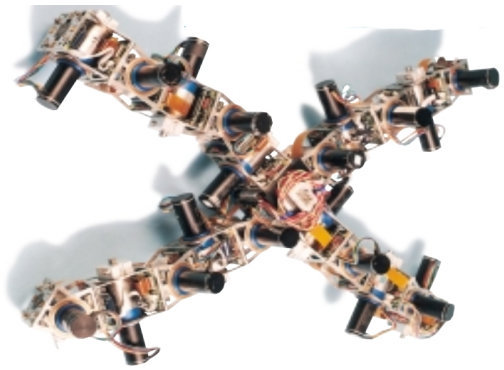

Figure 3: PolyBot - Xerox Palo Alto Research Center

Control of the Polybot robot required complete, local and parallel reconfiguration algorithms. Vassilvitkii, Yim, and Suh used 2x2x2 meta-modules to achieve reconfiguration using only local rules to control the robot[44].

Reconfigurable control techniques used on UASs usually involve some sort of closed loop plant matching. These types of controls are mainly used as fault-tolerant based systems that activate when a fault is detected. The closed loop response is then analyzed before and after the fault using some sort of numerical model[74][75]. If the same closed loop response can be guaranteed, then stability can be proven for a variety of different faults. Although simple as an overview, numerous texts have been created detailing all different types of reconfigurable control[70]. These include techniques such as neural networks (NN), parameter estimation, kalman filters or system dynamic inversion to name a few.

Some examples of reconfigurable control on mechanical systems include the work by Enns and Si, who

created a reconfigurable controller for a main rotor failure in helicopters by positioning the cyclic controls in a certain geometry to over actuate the system. When an actuator fault was detected, the controller would reconfigure itself to maintain cyclic control of the aircraft[72].

Yang, Blanke and Verhaegen used a similar technique on a generic robot system using model matching of H_∞ control. The basic idea is to match the systems before and after the fault through H_∞ control and use this to augment the control system. Stability and performance is shown to be robust when certain conditions are satisfied[69].

Mclean and Asiam-Mir created a simple reconfigurable control law of an over actuated fighter aircraft. The control system uses feedback control matching assuming a linear plant $\dot{x} = Ax + Bu$ where $u = Kx$. In this simple control law, the closed loop system is then $\dot{x} = (A + BK)x$. When a fault is detected, the B matrix conceivably changes to B_f; thus, the only requirement is that the K matrix should be updated accordingly such that $u = K_f x$. The task then requires the controller to compute K_f given B_f such that $B_f K_f = BK$. To do this, an optimization routine is performed since a complete closed loop match can often not be computed.

Morphing aircraft is a similar area of research that involves the need of an adaptive controller. Liu, Li and He created an adaptive controller for the Innovative Control Effectors (ICE) aircraft. This aircraft contains hundreds of morphing actuators in an array on each wing. The adaptive controller presented uses a Model Reference Adaptive Controller (MRAC) which requires the system to follow a desired reference model. Although, the dissertation here does not use an adaptive control technique the use of control allocation is needed. This ICE aircraft uses a similar control allocation scheme as the one presented in this thesis. In order to control an increased number of actuators, an allocation module is derived by a recursive update law such that the control effort of all controls is equal to the model and that each control actuator does not saturate. The basic idea is that $u = Tv$, where u is the input to the MRAC system and v is a vector of the over actuated controls. A recursive update law is performed at each control cycle to allocate all the controls v[67].

The control of the Distributed Flight Array (DFA), pictured in Figure 4, uses a similar approach as the

control law above. The DFA is a set of ground based rovers equipped with a single ducted fan and wheels to maneuver on the ground. Each rover drives independently, connects to other robots using mechanical connections and takes off as a unit. Since the configuration of the DFA is known, the relationship between v and u can be explicitly derived such that the matrix T is explicitly known regardless of the number of modules present or the configuration of the DFA. The pitch, roll and altitude dynamics are then decoupled using the configuration matrix T and the thrust of each module is computed for each control axis (pitch, roll and altitude) and summed together to get total control[56][57].

On Ground **In Flight**

Figure 4: Distributed Flight Array

1.2 Meta Aircraft

Derivatives of meta aircraft flight have been around for almost a century. Trapeze flight or hitchhiker flight has been investigated as early as 1934 as shown in Figure 5. Here two F9C-2 bi-planes attach to the bottom of the USS Macon blimp before performing their mission.

After WWII, the concept of Compound Aircraft Transport (CAT) was investigated for its benefit in range and endurance. As shown in Figure 6, the project *TipTow* involved two F-84s linking with a larger B-29. The two F-84s connect to the B-29 with a mechanical connection and subsequently power down their engines to hitchhike using the B-29. All of these tests were pilot in the loop flight tests and not autonomous. During one of the flight tests, one of the F-84s entered an unstable oscillation which resulted in a catastrophic failure. The project was subsequently canceled[50].

Figure 5: Trapeze Mission - Two F9C-2s attach to USS Macon - 1934

Figure 6: Project TipTow - 1953

Another example of CAT flight is the work by Moore and Maddalon who considered a multibody transport aircraft that consisted of two passenger jets permanently connected at the wing tips. The analysis showed a direct decrease in weight due to lower bending moment of the connected wing as well as an L/D increase of 8-10% from the single vehicle configuration[53]. A concept of this aircraft is shown in Figure 7.

Another meta aircraft is Aurora's Odysseus concept as pictured in Figure 8. This aircraft consists of three independent aircraft that connect in mid air, wing tip to wing tip. Each aircraft is equipped with solar panels to maintain a constant power supply. The primary goal of this three body meta aircraft was to remain airborne and sample the wind environment continuously. Unfortunately, no simulation or prototype has been developed for this concept[54].

Although not technically a modular robot, NASA's Helios demonstrated the capability of a highly flexible UAV to maintain hours of perpetual flight using solar power. It is also the first aircraft since 1976 to break the world record for highest altitude flight of 96,863 feet. This UAV, pictured in Figure 9, unfortunately

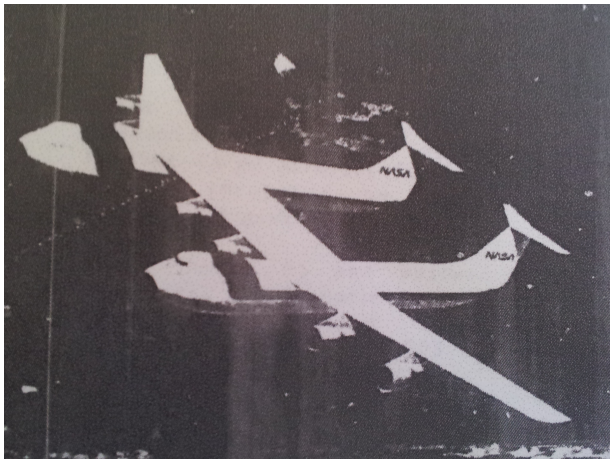

Figure 7: Permanently Connected Aircraft Transport

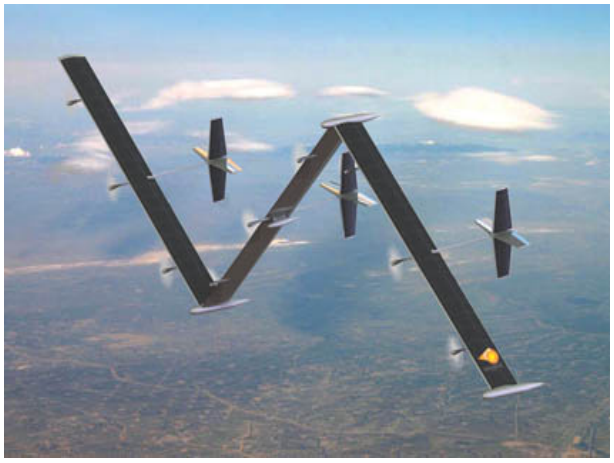

Figure 8: Odysseus Concept - Aurora

suffered a mishap in 2003 due to atmospheric turbulence and instability and crashed during a high altitude flight test[55].

1.3 Formation Flight

Unmanned Aerial Vehicles (UAVs) have found uses in a variety of civilian and military applications. The Raven and Predator are two examples of UAVs that assist soldiers in search and rescue missions or SEAD missions which requires multiple types of aircraft to complete[1]. The Raven, pictured in Figure 10 (Left), is primarily used for close-in support reconnaissance missions whereas the Predator, pictured in Figure 10

Figure 9: Helios Prototype - NASA

(Right), is the most combat-proven UAS in the world[2][3]. This UAS is able to fly up to 25,000 feet with an endurance of over 40 hours and can accept a variety of different payloads.

Raven - AeroEnvironment Inc

Predator - General Atomics

Figure 10: UAVs Primarily Used for Military Missions

In addition, NASA's Ikhana, pictured in Figure 11 (Left), as well as NASA's Globalhawk (Right) are two UAVs that are mainly used for weather surveillance as well as image sensing for crop farmers or firefighters[4]. The Globalhawk has recently been announced to start missions to accurately measure the dynamics of hurricanes[5].

Although numerous aircraft have been used in a variety of different missions, research has continuously been performed to try and increase range and endurance of these aircraft. Formation flight has been known as a way to increase range and endurance since the first time scientists and biologists noticed the flying "V" configuration often utilized by birds, pictured in Figure 12. These birds fly in this formation to increase L/D

Ikhana - NASA

GlobalHawk - NASA

Figure 11: UAVs Primarily Used for Weather Research and Image Sensing

on the trailing birds to reduce workload by flying in the upwash of the leading birds. For aircraft, flying in such close proximity must be done carefully and precisely to avoid collisions between aircraft thus adequate performance is needed to lower technology and pilot risks. With the increase in performance of aircraft control systems, formation flight has been re-investigated as a means of increasing range and endurance. In addition, numerous research projects have been created to use autonomous systems for formation flight[7−17].

Figure 12: Snow-Geese Flying in "V" Formation

Wieselberger was the first to attempt to quantify the benefits of flying in formation. Using Prandlt's lifting-line theory and horseshoe vortices, Wieselberger showed that a flying "V" formation can increase range and endurance by up to 70% from that of a lone bird[6]. Aircraft flying in formation will have different performance increases, because birds use their wings for both thrust, lift and control as opposed to aircraft which use their wings for lift and control and an engine or propeller for thrust. In the last decade, the

benefits of aircraft flying in a similar formation as birds has been well documented.

Magill, Schetz and Mason performed wind tunnel tests on a scaled F-84E connected to a B-36 to analyze the L/D benefits of CAT flight. Their wind tunnel measurements showed an increase in L/D of 20-40%[51,53]. In addition, a vortex lattice method computer tool was developed and showed agreement between experimental results and this simulation tool.

Vachon, Ray, Walsh, and Ennix investigated performance benefits from formation flight of an F/A-18 under the Autonomous Formation Flight (AFF) project at the NASA Dryden Flight Research Center[12]. The trailing pilot required use of a station-keeping control system to maintain flight in the wake of the leading aircraft[13], pictured in Figure 13. Their measurements revealed a drag reduction of over 20% and a fuel flow reduction of 18%.

Figure 13: F/A-18 Autonomous Formation Flight Project - NASA Dryden Research Center

Gibbs, Vlachos, and Telionis created an experimental method for determining lift and drag distributions for wings in formation flight. These experiments led to direct modeling of close formation flight as well as wing tip-docked flight[11].

Ning, Flanzer, and Kroo explored a more practical approach to formation flight using commercial aircraft coined extended formation flight[16]. Extended formation flight involves flying in formation with a separation distance of at least 10 wingspans. It was found that the induced drag can be reduced by up to 30%. This increased distance between aircraft has the added benefit of decreasing the hazard of flying in such close

proximity as in conventional formation flight.

Venkataramanan, Dogan, and Blake also created a modified lifting line model that could be incorporated into a 6DOF simulation model. Wind tunnel test results agreed well with this modified model[17]. King and Gopalarathnam created a method for determining the optimum lift distribution for a given formation flight geometry with formations of up to 25 aircraft[14]. Their analysis, involved a minimization routine to obtain the optimal lift distribution on the wings of the aircraft flying in formation. This analysis exhibited good agreement with experimental results and provides techniques that allow aircraft to increase L/D to its maximum potential.

Although formation flight has many benefits, there are many design challenges that inhibit its widespread implementation. Slater has conducted research to propose control laws which make self-spacing in commercial aircraft a viable option[7]. This control law technique was geared towards formation flight with separation distances of hundreds of meters. Fowler and D'Andrea analyzed three separate formation control laws on a large array of wings with roll and lateral degrees of freedom. The analysis showed that a centralized controller had the smallest closed-loop gains but the decentralized controller had the best performance[10]. Dunbar and Murray created a generalized model predictive control (MPC) formulation to control multi-vehicle formations. This control system was carried out on a 6DOF model with a formation of three vehicles and desirable stability and performance were obtained[38]. Shim and Kim extended this MPC technique using a nonlinear model predictive control technique (NMPC) for multiple autonomous helicopters. Their technique uses a similar stabilization of vehicle dynamics with decentralized trajectory generation. The successful flight test of three autonomous helicopters showed success of this technique which included avoidance routines to navigate the helicopters in an urban environment[39]. Seanor, Campa, Gu, Napolitano, Rowe, and Perhinschi reported on a flight demonstration of a formation control scheme using three scaled YF-22 aircraft[15]. The formation flight control law consisted of a set of inner and outer loop control schemes using a combination of feedback linearization and PID control. Adequate formation was achieved; however, no data on L/D increase or performance characteristics were obtained.

A key problem of control of formation flight is the introduction of time-delay between the lead aircraft and

the followers created by decentralized controllers. Allen, Ryan, Hanson, and Parle examined the propagation of error between the lead aircraft and the follower aircraft often called string stability of formation flight. Their analysis found ways to analyze string systems and provide metrics for unstable string formations with results for up to 7 aircraft[9]. In addition, Weitz and Hurtado created a method to determine the maximum allowable time delay for an N formation system[8].

1.4 Aerial Refueling

Aerial refueling (AR) is a commonly used method to increase range, payload and endurance of an aircraft. In certain AR missions, a tanker aircraft flies steady and level and releases a drogue that trails the tanker aircraft. The following aircraft must then rendezvous with the drogue to begin receiving fuel using a probe that extends in front of the aircraft. Although difficult, this is often necessary for fighter aircraft to accomplish long range missions as fuel on board is limited. The design of creating a maneuverable aircraft while increasing fuel capacity are often competing designs; thus, increasing the benefit of AR. Although widely used, AR is still a difficult task that requires the pilot to perform precise maneuvers to interface with the refueling device. This is even more challenging when attempting an AR mission using autonomous vehicles. In the last decade, autonomous aerial refueling (AAR) has been a topic of interest as flight control systems and sensor feedback performance has improved, increasing the feasibility of these missions. Figure 14 shows an example autonomous aerial refueling flight test using two Global Hawks as a part of DARPA's Autonomous High-Altitude Refueling program.

Similar to formation flight, AAR requires the aircraft to fly in formation giving rise to the need for complex control systems to navigate multiple flying vehicles. Numerous path planning techniques have been developed for UAVs using many types of nonlinear control systems from Mixed Integer Linear Programming (MILP) to MPC[29−36]. However, without the use of precise feedback these algorithms are not sufficiently precise for AAR missions given the practicality of sensor inaccuracies.

Numerous docking maneuvers have been successful by using machine vision (MV) feedback. In 1994, Murray and Basu created a simple motion tracking control law using an active camera[24]. This technology

Figure 14: Autonomous Aerial Refueling Test - DARPA's Autonomous High Altitude Refueling program

has been extended to UAVs with incredible results. Wenzel, Rosset, and Zell created a visual feedback control law that successfully hovers a rotorcraft and chooses a landing zone with low-cost sensors[26].

The most similar problem to the meta aircraft problem is creating a successful rendezvous between two bodies. Goldin created a perching control law using a quadrotor and on board cameras to navigate this complicated perching maneuver[25]. In addition, Morris created an autonomous spacecraft docking controller using a vision-based relative navigation sensor[27].

In terms of AAR, MV technology is required for the successful docking of the probe and drogue system. Fravolini, Ficola, Campa, Napolitano, and Seanor first reported a composite docking control scheme blending overall Global Positioning System (GPS) data with MV[22]. Valasek, Gunnam, Kimmett, Tandale and Junkins pursued a similar line of research and used a vision based navigation system called VisNav, chosen for its high-precision six-degree-of-freedom information for realtime navigation applications. The sensor weighed about $500g$ and used a timing scheme of 4 to 6 light emitting diodes (LEDs) that fire onto a receiving surface. The LEDs are mounted on one body with a fixed orientation with respect to the body frame. The sensor is fixed to another body and reads the inputs of the LEDs. Using a nonlinear optimization algorithm, the position and attitude of the body with respect to the first body is obtained in real time. This navigation sensor is sufficiently accurate to be well suited to the aerial refueling problem[20]. Tandale, Bowers and Valasek reported using the VisNav sensor with a reference-observer-based tracking controller. The drogue

location is estimated by the VisNav sensor and translated into smooth trajectory generation. Feasibility and performance of this controller were demonstrated by simulating docking maneuvers in the presence of varying levels of atmospheric turbulence[18]. The results show that performance degrades as atmospheric turbulence is increased. Mammarella, Campa, Napolitano, Seanor and Fravolini also created a simulation environment for a GPS/MV based approach for the problem of AAR[19].

1.5 Contributions of Thesis

The contributions of this thesis involve three distinct research areas that are related in that they all involve meta aircraft systems. The three research areas are:

1. Exploration of the flight dynamics of meta aircraft configurations including rigid body modes and flexible mode shapes
2. Creation of a robust two-stage connection control law with an exploration of methods to increase percent connection rate in realistic wind disturbances with sensors errors
3. Analysis of meta aircraft performance in winds by using a meta aircraft control law that adequately controls meta aircraft in drastically different conditions as well an analysis of lift to drag ratio changes

1.6 Thesis Outline

This thesis is composed of six chapters. A brief description of each chapter follows:

1. **Chapter 1: Introduction.** A description of the problem statement and the previous work on related research are described.
2. **Chapter 2: Meta Aircraft Simulation Tool.** A simulation tool that accurately models key aspects of a meta aircraft system is developed. All parameters used in the following chapters are detailed as well.
3. **Chapter 3: Meta Aircraft Flight Dynamics.** An exploration of the flight dynamics of meta aircraft configurations with a focus on the flight dynamic modes and mode shapes. This chapter

begins with the flight dynamic modes of motion for meta aircraft and then moves on to the flexible modes of motion for meta aircraft.

4. **Chapter 4: Meta Aircraft Connection Dynamics.** This chapter explores connection flight dynamics for a two body meta aircraft system where the vehicles are connected wing tip to wing tip using passive magnets with a particular focus on modeling the connection event between aircraft in a practical environment. The work reported in this chapter presents a two stage air vehicle connection control law driven by conventional 6 degree of freedom aircraft feedback plus relative position feedback of the lead aircraft.

5. **Chapter 5: Meta Aircraft Flight Performance.** This chapter explores the control of meta aircraft in numerous configurations with a focus on the performance of different types of configurations in a realistic wind environment. A control law is formed that adequately controls meta aircraft in a variety of different configurations by using a simplified rigid body dynamics model that alters inner and outer loop configuration dependent gains. This control law is then used to explore the benefits of a meta aircraft from a stability and lift to drag performance perspective.

6. **Chapter 6: Conclusions and Future Work.** Conclusions from the previous three research contributions are summarized and future work relating to several areas is proposed.

2 Meta Aircraft Simulation Tool

In order to explore meta aircraft dynamics, a simulation tool that accurately models key aspects of this system was developed. The flight dynamic simulation is formed by modeling each aircraft in the meta aircraft system independently. Each aircraft is excited by typical loads that an individual aircraft experiences including gravitational and aerodynamic forces and moments. The basic connection mechanism for this meta aircraft is passive magnets placed at the wing tips of each aircraft. When aircraft are close, collisions can occur giving rise to contact forces and moments. The simulation is thus extended to include a non-linear magnetic routine and a soft contact model. Furthermore, when aircraft wing tips are close, wing tip vortices can interact changing the overall lift distribution of the wings. To model this effect, all wings are split into aerodynamic elements and a horseshoe vortex is placed at each element. These vortices are used to compute the aerodynamic interaction between aircraft by using strip theory coupled to a vortex lifting line wake model. Figure 15 is a graphic highlighting all aspects of the connection simulation of the meta aircraft which are explained in the following subsections.

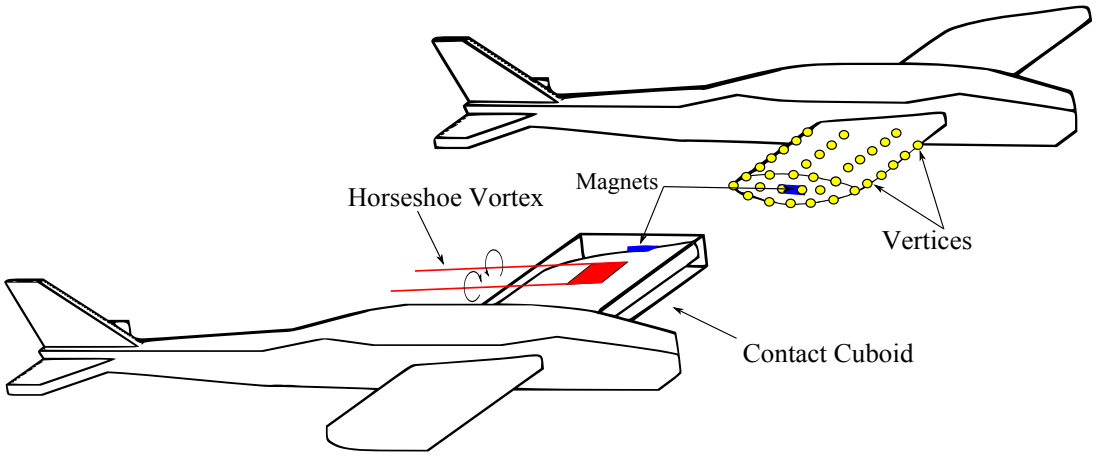

Figure 15: Close Up Representation of All Interaction Effects

2.1 Flight Dynamics

Figure 16 shows a schematic of two bodies approaching for connection where the subscripts denote the Inertial (I), Magnet (M), Leader (L) and Follower (F) reference frames. The follower and leader reference frames are both body fixed and centered at the mass center of each aircraft. Similarly, the magnet frame is attached to the magnet and aligned with its natural axis on the follower aircraft.

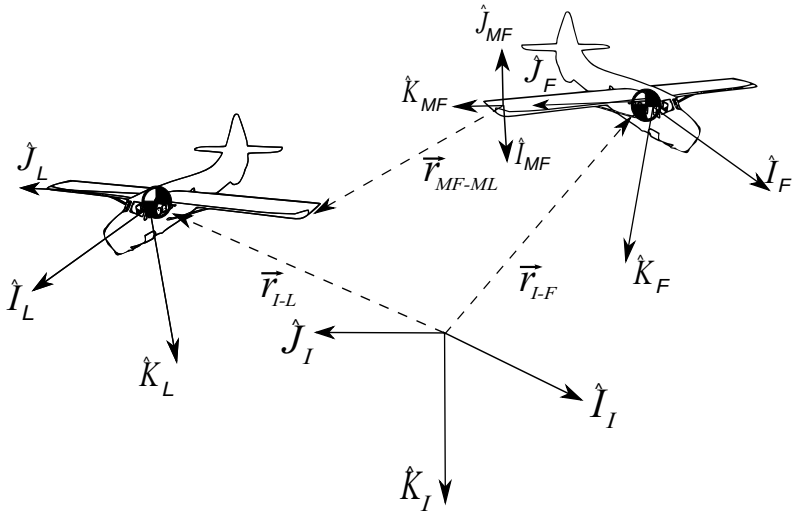

Figure 16: Meta Aircraft Two Body Schematic

The kinematic equations of motion for aircraft i are taken about the mass center of each aircraft with the body frame aligned using standard aerospace convention. These equations are standard rigid body equations and have been reported in many sources[84].

$$\begin{Bmatrix} \dot{x}_i \\ \dot{y}_i \\ \dot{z}_i \end{Bmatrix} = [\mathbf{T}_{IB_i}] \begin{Bmatrix} u_i \\ v_i \\ w_i \end{Bmatrix} \tag{1}$$

$$\begin{Bmatrix} \dot{\phi}_i \\ \dot{\theta}_i \\ \dot{\psi}_i \end{Bmatrix} = [\mathbf{H}_i] \begin{Bmatrix} p_i \\ q_i \\ r_i \end{Bmatrix} \tag{2}$$

The matrix $\mathbf{T}_{IB_i}$ represents the transformation matrix from the ith body reference frame to the inertial reference frame, which is constructed using the standard aerospace rotation sequence. The matrix $\mathbf{H}_i$ relates the body angular velocity components to the time derivative of the Euler angles. Standard shorthand notation is used for trigonometric functions: $cos(\alpha) \equiv c_\alpha$, $sin(\alpha) \equiv s_\alpha$, and $tan(\alpha) \equiv t_\alpha$.

$$\mathbf{T}_{IB_i} = \begin{bmatrix} c_{\theta_i} c_{\psi_i} & s_{\phi_i} s_{\theta_i} s_{\psi_i} - c_{\phi_i} s_{\psi_i} & c_{\phi_i} s_{\theta_i} c_{\psi_i} + s_{\phi_i} s_{\psi_i} \\ c_{\theta_i} s_{\psi_i} & s_{\phi_i} s_{\theta_i} s_{\psi_i} + c_{\theta_i} c_{\psi_i} & c_{\phi_i} s_{\theta_i} s_{\psi_i} - s_{\phi_i} c_{\psi_i} \\ -s_{\theta_i} & s_{\phi_i} c_{\theta_i} & c_{\phi_i} c_{\theta_i} \end{bmatrix} \tag{3}$$

$$\mathbf{H}_i = \begin{bmatrix} 1 & s_{\phi_i} t_{\theta_i} & c_{\phi_i} t_{\theta_i} \\ 0 & c_{\phi_i} & -s_{\phi_i} \\ 0 & s_{\phi_i}/c_{\theta_i} & c_{\phi_i}/c_{\theta_i} \end{bmatrix} \tag{4}$$

The dynamic equations are formed by summing forces and moments about the system mass center in the body reference frame and equating the result to the time derivative of linear and angular momentum. The translational and rotational dynamic equations of motion are expressed below.

$$\begin{Bmatrix} \dot{u}_i \\ \dot{v}_i \\ \dot{w}_i \end{Bmatrix} = \frac{1}{m_i} \begin{Bmatrix} X_i \\ Y_i \\ Z_i \end{Bmatrix} - \begin{bmatrix} 0 & -r_i & q_i \\ r_i & 0 & -p_i \\ -q_i & p_i & 0 \end{bmatrix} \begin{Bmatrix} u_i \\ v_i \\ w_i \end{Bmatrix} \tag{5}$$

$$\begin{Bmatrix} \dot{p}_i \\ \dot{q}_i \\ \dot{r}_i \end{Bmatrix} = [I_i]^{-1} \left(\begin{Bmatrix} L_i \\ M_i \\ N_i \end{Bmatrix} - \begin{bmatrix} 0 & -r_i & q_i \\ r_i & 0 & -p_i \\ -q_i & p_i & 0 \end{bmatrix} [I_i] \begin{Bmatrix} p_i \\ q_i \\ r_i \end{Bmatrix} \right) \tag{6}$$

The mass moment of inertia matrix I_i is taken about the center of mass of the aircraft. The applied forces and moments expressed in equations (5) and (6) contain contributions from weight *(W)*, aerodynamics *(A)*, magnet *(M)*, and contact *(C)* loads. The total forces and moments applied to the vehicle expressed in the body reference frame are given below.

$$\begin{Bmatrix} X_i \\ Y_i \\ Z_i \end{Bmatrix} = \begin{Bmatrix} X_{Wi} + X_{Ai} + X_{Mi} + X_{Ci} \\ Y_{Wi} + Y_{Ai} + Y_{Mi} + Y_{Ci} \\ Z_{Wi} + Z_{Ai} + Z_{Mi} + Z_{Ci} \end{Bmatrix} \tag{7}$$

$$\begin{Bmatrix} L_i \\ M_i \\ N_i \end{Bmatrix} = \begin{Bmatrix} L_{Ai} + L_{Mi} + L_{Ci} \\ M_{Ai} + M_{Mi} + M_{Ci} \\ N_{Ai} + N_{Mi} + N_{Ci} \end{Bmatrix} \tag{8}$$

The weight contribution is given by:

$$\begin{Bmatrix} X_{Wi} \\ Y_{Wi} \\ Z_{Wi} \end{Bmatrix} = m_i g \begin{Bmatrix} -s_{\theta_i} \\ s_{\phi_i} c_{\theta_i} \\ c_{\phi_i} c_{\theta_i} \end{Bmatrix} \tag{9}$$

The aerodynamic force for all lifting surfaces on the body (main wing, horizontal tail, and vertical tail) are calculated using well documented strip theory coupled to a vortex lifting line wake model. All lifting surfaces are split into a discrete number of elements and lift and drag is computed for each element. The aerodynamic forces and moments associated with the fuselage are computed using a standard aerospace expansion.

$$\begin{Bmatrix} X_{A_i} \\ Y_{A_i} \\ Z_{A_i} \end{Bmatrix} = \begin{Bmatrix} X_{E_i} \\ Y_{E_i} \\ Z_{E_i} \end{Bmatrix} + \begin{Bmatrix} X_{F_i} \\ Y_{F_i} \\ Z_{F_i} \end{Bmatrix} \tag{10}$$

In the equation above, the subscripts denote contributions from all the lifting surface elements (E) and the

fuselage(F). The equation below details the computation of aerodynamic forces produced by the lifting surface element (main wing and tail surfaces). In this analysis the horizontal and vertical tails contain one element. Thus the first term is summed from 0 to N+2 where N is the number of lifting surface elements on the main wing and the extra two terms are for the horizontal and vertical tails. Note that the matrix $\mathbf{T}_{nB_i}$ is a transformation matrix from the local nth element frame to the ith body aircraft frame. This allows for inclusion of wing sweep and dihedral effects.

$$\begin{Bmatrix} X_{E_i} \\ Y_{E_i} \\ Z_{E_i} \end{Bmatrix} = \frac{1}{2}\rho \sum_{n=0}^{N+2} (\mathbf{T}_{nB_i})^T S_n {V_n}^2 \begin{Bmatrix} C_{Ln}s_{\alpha_n} - C_{Dn}c_{\alpha_n} \\ 0 \\ -C_{Ln}c_{\alpha_n} - C_{Dn}s_{\alpha_n} \end{Bmatrix} \tag{11}$$

The lift and drag coefficients for each element are:

$$\begin{Bmatrix} C_{Ln} \\ C_{Dn} \end{Bmatrix} = \begin{Bmatrix} C_{L0n} + C_{L\alpha n}\alpha_n \\ C_{D0n} + C_{D\alpha n}{\alpha_n}^2 \end{Bmatrix} \tag{12}$$

Using the aircraft velocity with respect to atmospheric winds, it is possible to compute the total velocity, angle of attack and sideslip for each element

$$V_n = \sqrt{{u_n}^2 + {v_n}^2 + {w_n}^2} \tag{13}$$

$$\alpha_n = tan^{-1}\left(\frac{w_n}{u_n}\right) \tag{14}$$

$$\beta_n = sin^{-1}\left(\frac{v_n}{V_n}\right) \tag{15}$$

These velocity components include the effects due to aircraft motion, atmospheric winds, and induced velocity

and are expressed in the local element frame.

$$\begin{Bmatrix} u_n \\ v_n \\ w_n \end{Bmatrix} = \mathbf{T}_{nB_i} \left[\begin{Bmatrix} u_i \\ v_i \\ w_i \end{Bmatrix} + \begin{bmatrix} 0 & -r_i & q_i \\ r_i & 0 & -p_i \\ -q_i & p_i & 0 \end{bmatrix} \begin{Bmatrix} r_{xn} \\ r_{yn} \\ r_{zn} \end{Bmatrix} + (\mathbf{T}_{IB_i})^T \begin{Bmatrix} V_x \\ V_y \\ V_z \end{Bmatrix} \right] + \begin{Bmatrix} u_{In} \\ v_{In} \\ w_{In} \end{Bmatrix} \tag{16}$$

The equation above contains contributions from 4 sources. The first is the aerodynamic velocity of the mass center of aircraft i. The second term is due to aircraft rotational motion where r_{xn}, r_{yn}, r_{zn} are the scalar distances from the computation point of the nth element to the center of mass of aircraft i. The third term includes atmospheric winds (V_x, V_y,V_z) which are arbitrary functions of both space and time. The final term is the induced velocity produced by all other lifting surface elements in the meta aircraft system. The fuselage is modeled using an aerodynamic expansion taken about the center of mass of the aircraft

$$\begin{Bmatrix} X_{F_i} \\ Y_{F_i} \\ Z_{F_i} \end{Bmatrix} = \frac{1}{2}\rho S_i {V_i}^2 \begin{Bmatrix} C_{Lf}s_{\alpha_i} - C_{Df}c_{\alpha_i} + C_{x_{\delta_t}}\delta_{t_i} \\ C_{yf} \\ -C_{Lf}c_{\alpha_i} - C_{Df}s_{\alpha_i} \end{Bmatrix} \tag{17}$$

where the fuselage coefficients are

$$\begin{Bmatrix} C_{Lf} \\ C_{Df} \\ C_{yf} \end{Bmatrix} = \begin{Bmatrix} C_{L0f} + C_{L\alpha f}\alpha + \frac{c}{2V_\infty}C_{Lqf}q + C_{L\delta_e}\delta_e \\ C_{D0f} + C_{D\alpha f}\alpha^2 \\ C_{y\beta f}\beta + C_{y\delta_r}\delta_r + \frac{b}{2V_\infty}(C_{ypf}p + C_{yrf}r) \end{Bmatrix} \tag{18}$$

The body aerodynamic moment is then computed by pitch moments from all lifting surfaces as well as

including the effect of forces offset from the center of mass.

$$\begin{Bmatrix} L_{Ai} \\ M_{Ai} \\ N_{Ai} \end{Bmatrix} = \frac{1}{2}\rho \sum_{n=0}^{N+2} \left(\mathbf{T}^T{}_{nB_i} {V_n}^2 S_n c_n \begin{Bmatrix} 0 \\ C_{mn} \\ 0 \end{Bmatrix} + \begin{bmatrix} 0 & -r_{zn} & r_{yn} \\ r_{zn} & 0 & -r_{xn} \\ -r_{yn} & r_{xn} & 0 \end{bmatrix} \begin{Bmatrix} X_{An} \\ Y_{An} \\ Z_{An} \end{Bmatrix} \right) + \frac{1}{2}\rho S_i {V_i}^2 \begin{Bmatrix} b_i C_{lf} \\ c_i C_{mf} \\ b_i C_{nf} \end{Bmatrix} \tag{19}$$

where the fuselage coefficients are

$$\begin{Bmatrix} C_{lf} \\ C_{mf} \\ C_{nf} \end{Bmatrix} = \begin{Bmatrix} C_{l\beta f}\beta + \frac{b}{2V_\infty}(C_{lpf}p + C_{lrf}r) + C_{l\delta_a}\delta_a + C_{l\delta_r}\delta_r \\ C_{m0f} + C_{m\alpha f}\alpha + \frac{c}{2V_\infty}C_{mqf}q + C_{m\delta_e}\delta_e \\ \frac{b}{2V_\infty}(C_{npf}p + C_{nrf}r) + C_{n\beta f}\beta + C_{n\delta_a}\delta_a + C_{n\delta_r}\delta_r \end{Bmatrix} \tag{20}$$

The aerodynamic coefficients in equations (11), (12) and (17)-(20) are obtained from flight data, aerodynamic modeling and wind tunnel tests[81].

2.2 Nonlinear Lifting Line Wake Model

When aircraft wing tips are close, trailing vortices from different lifting surfaces interact with each other causing a change in aerodynamic loading. Figure 17 shows an example three aircraft configuration. Each dot is an aerodynamic element containing three vortices, one bound vortex and two trailing vortices. All the vortices shown in this Figure, interact with each other changing the overall lift distribution of the system. To compute this interaction, the aerodynamic model utilizes a nonlinear lifting line wake model for an incompressible and inviscid flow field about a finite wing[51,86,87]. Each lifting surface element contains one horseshoe vortex where the strength of the vortex is unknown. The method employed here is an iterative method where an initial induced velocity is assumed at each element and equation (16) is used to compute the local velocity and angle of attack at each element. Then equation (12) is used to compute the lift coefficient at each element. Using the Kutta-Joukowski theorem, the lift coefficient is written as a function

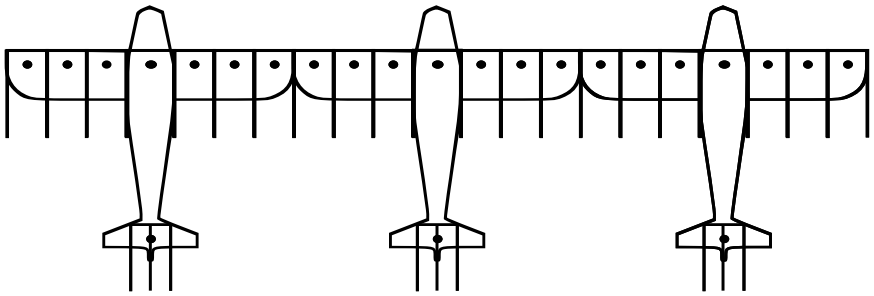

Figure 17: Aerodynamic Wake Interaction in a Three Aircraft Wing tip to Wing tip Configuration

of the strength of the horseshoe vortex at the nth element (Γ_n) as shown in equation (21)[86].

$$\Gamma_n = C_{Ln} c_n V_n / 2 \tag{21}$$

Using the equation above, the induced velocity contribution of every element can be computed. Horseshoe vortices are composed of three vortex filaments. There is a bound vortex that is parallel to the sweep angle of the wing and two trailing vortices parallel to the local velocity at that element. The total induced velocity caused by one horseshoe vortex can then be determined by computing the induced velocity associated with each filament separately and summing the three contributions together. The Biot-Savart Law is used to calculate the induced velocity of a vortex filament (Figure 18) and is used to generate equation (22)[51,86,87]

$$W_{AB,C} = \frac{\Gamma_n}{4\pi r_p}(cos(\theta_1) - cos(\theta_2)) \tag{22}$$

where $W_{AB,C}$ is the downwash velocity at point C in the local element frame caused by the vortex filament from point A to point B. The induced velocity of the nth element is equal to the sum of the induced velocities of all other horseshoe vortices in this multi-element system. Thus, the induced velocity ($\mathbf{W}_{I,i}$) of the nth

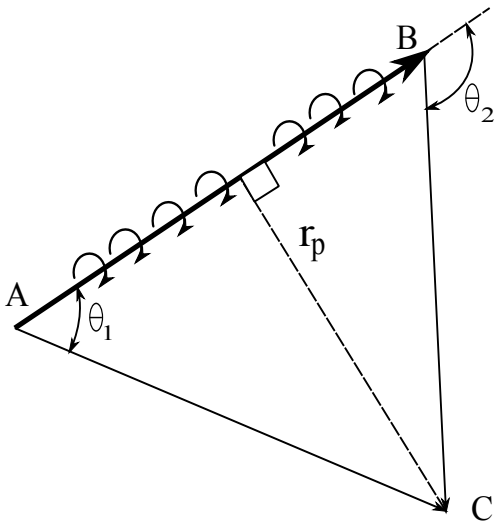

Figure 18: Diagram of Vortex Filament AB Strength as Seen by Point C

element can be given in matrix form by the equation below.

$$\begin{Bmatrix} W_{I,1} \\ W_{I,2} \\ \vdots \\ W_{I,N+2} \end{Bmatrix} = \begin{bmatrix} C_{1,1} & C_{1,2} & \dots & C_{1,N+2} \\ C_{2,1} & C_{2,2} & \dots & C_{2,N+2} \\ \dots & \dots & \ddots & \dots \\ C_{N+2,1} & C_{N+2,2} & \dots & C_{N+2,N+2} \end{bmatrix} \begin{Bmatrix} \Gamma_1 \\ \Gamma_2 \\ \vdots \\ \Gamma_{N+2} \end{Bmatrix} \tag{23}$$

In this equation, the matrix $C_{n,m}$ relates the strength of the nth horseshoe vortex on the mth element. An iterative method is used to solve for the induced velocity using equations (16), (12), (21), and (23) in that respective order. This iteration process is repeated until the entire system converges. This usually requires about 10 iterations to converge between integration time steps provided that the time step is small. This type of numerical computation is commonly referred to as fixed point iteration. Fixed point iteration commonly exhibits convergence problems and a damping parameter is often used between iterations to ensure that the system converges. This method has been validated against existing analytic solutions with good agreement[88],[89].

2.3 Magnetic Forces

The basic connection mechanism used in this simulation is passive magnets placed at the wing tips of each aircraft. When the aircraft wing tips are in close proximity, magnetic interaction forces and moments become substantial. A schematic of two magnets is shown in Figure 19. The magnet placed on the leader aircraft is shown with a non-zero rotation relative to the follower magnet. Each magnet has its own magnet-fixed reference frame located at the mass center of the magnet. The subscript for these frames are *MP* and *MC* which denotes the leader and follower magnetic reference frames respectively. Both magnets are magnetized through their $\hat{K}$ axes with a magnetic moment $\vec{M}$. To compute the magnetic forces and moments, the magnets are assumed to be cuboidal with uniform charge throughout each magnet. Analytical solutions of the forces and moments between magnets has been reported in [90] where both magnets are aligned without any relative rotation. It is possible to compute the magnetic force and moment as a function of spatial separation for cuboidal magnets as derived by Yonnet[90−92] and has been extended to non cuboidal magnets as well as single rotations between each magnet[93−94]. Due to the relative rotation along all axes that is possible for the magnets on the leader and follower aircraft a numerical approach is used here.

Magnets create forces between each other by interacting with their inherent magnetic fields. When a body comes into this magnetic field, a force is produced. The equation that relates the magnetic field of a magnet to a another magnet is given by the equation below.

$$\vec{F}_{Lijk} = \mu_0 \nabla (\vec{M}_{ML} \cdot \vec{H}_{MF}) \tag{24}$$

where $\vec{M}_{ML}$ is the magnetization vector of the magnet on the leader aircraft, $\vec{H}_{MF}$ is the magnetic field generated by the magnet on the follower aircraft and μ_0 is the permeability of free space. Kelvin's formula, as shown in equation (24), computes the force ($\vec{F}_{Lijk}$) of a cuboidal element interacting with a magnetic field produced by another magnet[92]. In order to compute the full force produced by two magnets, the leader magnet is broken into a discrete set of elements and Kelvin's formula is used to compute the force at each element q. First, the magnetic field of the follower magnet is computed analytically. The magnetic field is

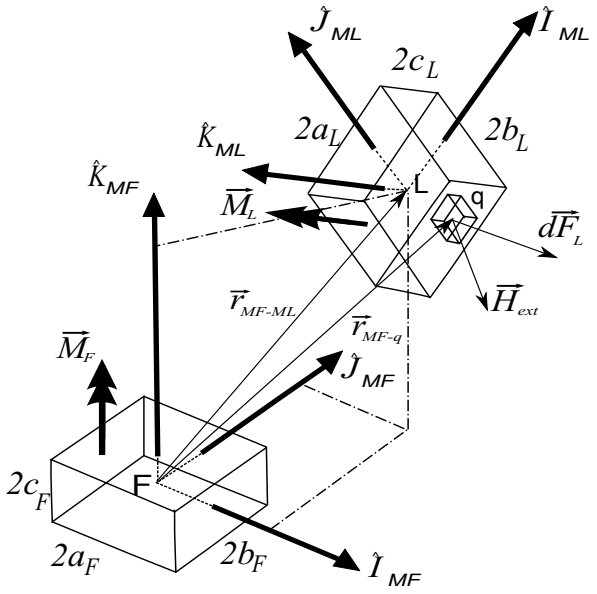

Figure 19: Magnet Configuration

computed at point q assuming the magnets are a distance (x_{fl}, y_{fl}, z_{fl}) away in the M_F reference frame as shown below.

$$\begin{aligned} \vec{r}_{MF\to ML} &= -\vec{r}_{F\to MF} - \vec{r}_{I\to F} + \vec{r}_{I\to L} + \vec{r}_{L\to ML} \\ \vec{r}_{MF\to ML} &= x_{fl}\hat{I}_{MF} + y_{fl}\hat{J}_{MF} + z_{fl}\hat{J}_{MF} \end{aligned} \tag{25}$$

For this analysis $\vec{M}_{MF} = J\hat{K}_{MF}$ and $\vec{M}_{ML} = J\hat{K}_{ML}$ for simplicity. The magnetic field of the follower magnet can be computed by first computing the magnetic field of a flat plate and summing this over the magnet along $\hat{K}_{MF}$ [90]. The magnetic field is given below in equation (26).

$$\begin{aligned} \vec{H}_{MF} &= \sum_{i=0}^{1}\sum_{j=0}^{1}\sum_{k=0}^{1} \frac{J}{4\pi\mu_0}\left[-ln(R+T)\hat{I}_{MF} - ln(R+S)\hat{J}_{MF} + tan^{-1}\left(\frac{ST}{RU}\right)\hat{K}_{MF}\right] \\ S &= x_{fq} - (-1)^i a_f \\ T &= y_{fq} - (-1)^j b_f \\ U &= z_{fq} - (-1)^k c_f \\ R &= \sqrt{S^2+T^2+U^2} \end{aligned} \tag{26}$$

where

$$\vec{r}_{MF\to q} = x_{fq}\hat{I}_{MF} + y_{fq}\hat{J}_{MF} + z_{fq}\hat{J}_{MF} \tag{27}$$

The total magnetic force can then be obtained by substituting equations (25)-(27) into (24) and summing over all the elements of the leader magnet as shown in equation (28).

$$F_{XM}\hat{I}_{MF} + F_{YM}\hat{J}_{MF} + F_{ZM}\hat{K}_{MF} = \sum_{i=0}^{NM}\sum_{j=0}^{NM}\sum_{k=0}^{NM}\vec{F}_{Lijk}\ \Delta x_{lq}\Delta y_{lq}\Delta z_{lq} \tag{28}$$

where

$$\vec{r}_{ML\to q} = x_{lq}\hat{I}_{ML} + y_{lq}\hat{J}_{ML} + z_{lq}\hat{J}_{ML}$$

$$\begin{Bmatrix} x_{fq} \\ y_{fq} \\ z_{fq} \end{Bmatrix} = \begin{Bmatrix} x_{fl} \\ y_{fl} \\ z_{fl} \end{Bmatrix} + (\mathbf{T}_{B_F M_F})^T (\mathbf{T}_{IB_F})^T \mathbf{T}_{IB_L} \mathbf{T}_{B_L M_L} \begin{Bmatrix} x_{lq} \\ y_{lq} \\ z_{lq} \end{Bmatrix} \tag{29}$$

The torque on the magnets can also be obtained in a similar fashion by simply summing the moments produced by each elemental force as shown in equation (30).

$$T_{XM}\hat{I}_{MF} + T_{YM}\hat{J}_{MF} + T_{ZM}\hat{K}_{MF} = \sum_{i=0}^{NM}\sum_{j=0}^{NM}\sum_{k=0}^{NM}(\vec{r}_{ML\to q}\times\vec{F}_{Lijk})\ \Delta x_{lq}\Delta y_{lq}\Delta z_{lq} \tag{30}$$

Equations (28) and (30) give the total magnetic force and moment between the magnets applied to magnet L in the M_F frame. Thus, the total force and moment on the follower aircraft is shown in equation (31). Note that the moment also contains contributions due to the magnetic force not being applied directly at the mass center. The $S_{B_F}()$ symbol is used to denote the skew symmetric matrix operator on a vector in the

follower body frame. Multiplying this matrix by a vector is equivalent to a cross product.

$$\begin{Bmatrix} X_{MF} \\ Y_{MF} \\ Z_{MF} \end{Bmatrix} = -\mathbf{T}_{B_F M_F} \begin{Bmatrix} F_{XM} \\ F_{YM} \\ F_{ZM} \end{Bmatrix}$$
$$\begin{Bmatrix} L_{MF} \\ M_{MF} \\ N_{MF} \end{Bmatrix} = -\mathbf{T}_{B_F M_F} \begin{Bmatrix} T_{XM} \\ T_{YM} \\ T_{ZM} \end{Bmatrix} + S_{B_F}(\vec{r}_{F \to MF}) \begin{Bmatrix} X_{MF} \\ Y_{MF} \\ Z_{MF} \end{Bmatrix} \tag{31}$$

The magnetic forces and moments applied to the leader aircraft are computed using similar rotations.

$$\begin{Bmatrix} X_{ML} \\ Y_{ML} \\ Z_{ML} \end{Bmatrix} = (\mathbf{T}_{IB_L})^T \mathbf{T}_{IB_F} \mathbf{T}_{B_F M_F} \begin{Bmatrix} F_{XM} \\ F_{YM} \\ F_{ZM} \end{Bmatrix}$$
$$\begin{Bmatrix} L_{ML} \\ M_{ML} \\ N_{ML} \end{Bmatrix} = (\mathbf{T}_{IB_L})^T \mathbf{T}_{IB_F} \mathbf{T}_{B_F M_F} \begin{Bmatrix} T_{XM} \\ T_{YM} \\ T_{ZM} \end{Bmatrix} + S_{B_L}(\vec{r}_{L \to ML}) \begin{Bmatrix} X_{ML} \\ Y_{ML} \\ Z_{ML} \end{Bmatrix} \tag{32}$$

This formulation has been validated analytically for parallel magnets thus NM must be large enough to ensure convergence between the numerical formulation and the analytical solution. Still, this numerical technique allows direct computation of the forces and moments as a function of both spatial separation and orientation. Figure 20 shows F_{ZM} as a function of separation distance for an example magnet. When the separation distance is zero the magnets are touching. It is clear from this Figure that the influence of the magnet becomes negligible very quickly. This is important when designing the control system as it must be robust enough to fall in this window of the magnet to ensure proper connection.

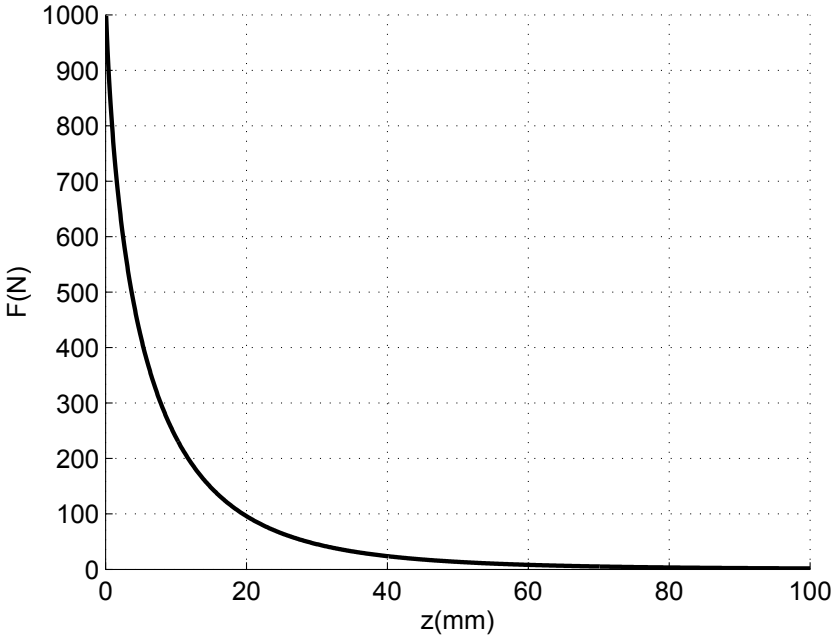

Figure 20: Magnet Strength(N) vs. Separation Distance(mm)

2.4 Soft Contact Model

During a connection event, joining aircraft can contact one another resulting in contact loads between bodies. Vertices are used to approximate the exterior shape of the follower wing and a rectangular prism is used to represent the wing on the leader aircraft. The contact forces and moments are computed when a vertex on the wing of the follower aircraft penetrates the wing on the leader aircraft. The soft contact model used was originally developed by Goyal[96] and has been used successfully in other simulations[97]. This model estimates the contact loads as well as Coulomb-like dry friction by modeling localized nonpermanent material deformation of the contacting surfaces. Contact between each vertex occurs through massless rigid planes called surface elements (SE). During contact, the SEs are constrained to remain parallel to the rectangular prism at the contact point but can slip against one another. Each body vertex is connected to a surface element through two pairs of springs and dampers (Figure 21). The normal spring and damper of the body are constrained to act along the normal vector of the contact cube and the tangential springs and dampers

act along the tangent vector. The equations used in this simulation are derived explicitly from Beyer and Costello[97]. During simulation, a contact detection method determines which body vertices have penetrated

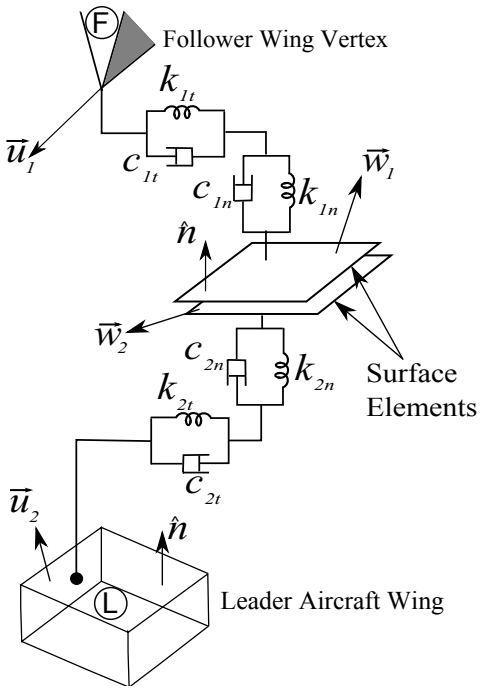

Figure 21: Spring and Damper Schematic for Soft Contact Model

the contact cube and the point of contact. The normal vector is then computed at this point of contact. Each contact point has two forces, a normal component $\vec{F}_n$ and a tangential component $\vec{F}_t$ which includes the affects of the springs and dampers as well as the friction force. These forces are applied on the follower body and expressed in the inertial frame. The normal and tangential forces are given in equations (33) and (34), where $\vec{s}_{1n}$ and $\vec{s}_{2n}$ are the distance vectors of the normal springs and $\vec{s}_{1t}$ and $\vec{s}_{2t}$ are the distance vectors of the tangential springs.

$$F_{X_n}\hat{I}_I + F_{Y_n}\hat{J}_I + F_{Z_n}\hat{K}_I = -\vec{b}_n \tag{33}$$

$$F_{X_t}\hat{I}_I + F_{Y_t}\hat{J}_I + F_{Z_t}\hat{K}_I = -\vec{b}_t + c^*\Delta\vec{w}_t \tag{34}$$

where

$$c^* = \frac{c_{1t}c_{2t}}{c_{1t} + c_{2t}} \tag{35}$$

$$\vec{b}_n = \frac{1}{c_{1n} + c_{2n}}(c_{2n}k_{1n}\vec{s}_{1n} - c_{1n}k_{2n}\vec{s}_{2n} + c_{1n}c_{2n}\Delta\vec{u}_n) \tag{36}$$

$$\vec{b}_t = \frac{1}{c_{1t} + c_{2t}}(c_{2t}k_{1t}\vec{s}_{1t} - c_{1t}k_{2t}\vec{s}_{2t} + c_{1t}c_{2t}\Delta\vec{u}_t) \tag{37}$$

In the above equations $\Delta\vec{u} = \vec{u}_1 - \vec{u}_2$ and $\Delta\vec{w} = \vec{w}_1 - \vec{w}_2$ where $\vec{u}_1$ and $\vec{u}_2$ are the absolute velocities of the contact point on the follower and leader aircraft and $\vec{w}_1$ and $\vec{w}_2$ are the absolute velocities of the two SEs. $\Delta\vec{u}_t$ and $\Delta\vec{u}_n$ are the tangential and normal components of $\Delta\vec{u}$. Similarly $\Delta\vec{w}_t$ and $\Delta\vec{w}_n$ are the tangential and normal components of $\Delta\vec{w}$. In this formulation $\Delta\vec{w}_n = 0$, since relative motion between the SEs along $\hat{n}$ is not allowed. The tangential force also includes the affect of friction. The two SEs can either be slipping or not. A state of stick exists when $|\vec{b}_t| \leq \mu|\vec{b}_n|$. Where μ is the coefficient of friction between the two SEs. While in a state of stick, $\Delta\vec{w}_t = 0$, which implies that $\vec{F}_t = -\vec{b}_t$. If the inequality is not true $\vec{w}_t$ is then set to the following:

$$\Delta\vec{w}_t = \frac{\lambda\vec{b}_t}{1 + \lambda c^*} \tag{38}$$

where

$$\lambda = \frac{|\vec{b}_t| - \mu|\vec{b}_n|}{c^*\mu|\vec{b}_n|} \tag{39}$$

The contact forces and moments in this formulation are applied on the follower aircraft and expressed in the inertial frame. Since the force is expressed in the inertial frame, the total force is identical for both follower and leader aircraft only the leader aircraft has a minus sign.

$$\begin{Bmatrix} X_{Ci} \\ Y_{Ci} \\ Z_{Ci} \end{Bmatrix} = (\mathbf{T}_{IB_i})^T \sum_{m=1}^{NC} \left(\begin{Bmatrix} F_{m,X_n} \\ F_{m,Y_n} \\ F_{m,Z_n} \end{Bmatrix} + \begin{Bmatrix} F_{m,X_t} \\ F_{m,Y_t} \\ F_{m,Z_t} \end{Bmatrix} \right) \tag{40}$$

$$\begin{Bmatrix} L_{Ci} \\ M_{Ci} \\ N_{Ci} \end{Bmatrix} = \sum_{m=1}^{NC} S_{B_i}(\vec{r}_{i\to Cm}) \begin{Bmatrix} X_{Cm} \\ Y_{Cm} \\ Z_{Cm} \end{Bmatrix} \tag{41}$$

The parameter NC is the number of contact points which must be large enough to approximate the wing. In addition to computing the forces and moments at the contact points, the state of the springs are tracked using the following differential equations:

$$\dot{\vec{s}}_{1n} = \frac{c_{2n}}{c_{1n}+c_{2n}}\Delta\vec{u}_n - \frac{1}{c_{1n}+c_{2n}}(k_{1n}\vec{s}_{1n} + k_{2n}\vec{s}_{2n}) \tag{42}$$

$$\dot{\vec{s}}_{2n} = \frac{-c_{1n}}{c_{1n}+c_{2n}}\Delta\vec{u}_n - \frac{1}{c_{1n}+c_{2n}}(k_{1n}\vec{s}_{1n} + k_{2n}\vec{s}_{2n}) \tag{43}$$

$$\dot{\vec{s}}_{1t} = \frac{c_{2t}}{c_{1t}+c_{2t}}(\Delta\vec{u}_t - \Delta\vec{w}_t) - \frac{1}{c_{1t}+c_{2t}}(k_{1t}\vec{s}_{1t} + k_{2t}\vec{s}_{2t}) \tag{44}$$

$$\dot{\vec{s}}_{2t} = \frac{-c_{1t}}{c_{1t}+c_{2t}}(\Delta\vec{u}_t - \Delta\vec{w}_t) - \frac{1}{c_{1t}+c_{2t}}(k_{1t}\vec{s}_{1t} + k_{2t}\vec{s}_{2t}) \tag{45}$$

2.5 Connection Interface Simplification

When simulating aircraft that are connected before the simulation starts, simplifications can be made to connection model. First the magnet model is removed entirely and replaced with a more intuitive spring mass damper system consisting of linear and rotational springs and dampers.

$$\begin{Bmatrix} X_{Ci} \\ Y_{Ci} \\ Z_{Ci} \end{Bmatrix} = \begin{Bmatrix} K_x\Delta x_{Wij} + C_x\Delta\dot{x}_{Wij} \\ K_y\Delta y_{Wij} + C_y\Delta\dot{y}_{Wij} \\ K_z\Delta z_{Wij} + C_z\Delta\dot{z}_{Wij} \end{Bmatrix}$$

$$\begin{Bmatrix} L_{Ci} \\ M_{Ci} \\ N_{Ci} \end{Bmatrix} = \begin{Bmatrix} K_\phi\Delta\phi_{ij} + C_\phi\Delta\dot{\phi}_{ij} \\ K_\theta\Delta\theta_{ij} + C_\theta\Delta\dot{\theta}_{ij} \\ K_\psi\Delta\psi_{ij} + C_\psi\Delta\dot{\psi}_{ij} \end{Bmatrix} \tag{46}$$

where $\Delta x_{Wij}, \Delta y_{Wij}, \Delta z_{Wij}$ are the inertial distances between the wing tip of the ith and jth aircraft. The values $\Delta\phi_{ij}$, $\Delta\theta_{ij}$, and $\Delta\psi_{ij}$ are the Euler angle differences between the ith and jth aircraft.

2.6 Wind Model

For small air vehicles, atmospheric winds are known to represent a large disturbance to the vehicle and can substantially affect aircraft motion. The atmospheric model in this simulation has two components, a spatial varying low frequency component from the Weather Research and Forecasting (WRF) model[99], as well as a full field Dryden turbulence model. The WRF model provides three dimensional, time varying atmospheric wind velocity information. This software is capable of generating realistic wind fields incorporating effects such as gravity waves, thermals and wind shear. The WRF simulation uses fully compressible non-hydrostatic equations to propagate the wind field forward in time. The WRF model is capable of exporting data at a user defined grid size at sampling intervals as low as 1 second. The WRF model only generates large scale, slowly varying atmospheric features. Turbulence is added according to the Dryden turbulence spectrum to complete the wind model. Due to the the complexity of the lifting line model, a 3D full field turbulence model is employed such that turbulence is correlated across the entire aircraft[84][100−105]. To do this, a 3-dimensional map is created by digitally simulating this random process using the Dryden turbulence spectrum. The full field Dryden turbulence spectrum is a 3x3 matrix that is a function of three spatial waves along each inertial axis such that $\vec{\Omega} = \Omega_x \hat{I}_I + \Omega_y \hat{J}_I + \Omega_z \hat{K}_I$. The Dryden turbulence spectrum is shown in equation (47).

$$\mathbf{\Theta}(\vec{\Omega}) = \frac{E(\vec{\Omega})}{4\pi\Omega^4} \begin{bmatrix} \Omega^2 - {\Omega_x}^2 & -\Omega_x\Omega_y & -\Omega_x\Omega_z \\ -\Omega_x\Omega_y & \Omega^2 - {\Omega_y}^2 & -\Omega_y\Omega_z \\ -\Omega_x\Omega_z & -\Omega_y\Omega_z & \Omega^2 - {\Omega_z}^2 \end{bmatrix} \tag{47}$$

In the above equation, Ω is the magnitude of the wave vector and $E(\vec{\Omega})$ is the energy density function which is defined in the equation below[101].

$$E(\vec{\Omega}) = \frac{8\sigma^2 L}{\pi} \frac{(L\Omega)^4}{(1 + (L\Omega)^2)^3} \tag{48}$$

The energy density function takes L as the length scale of the turbulence and σ is the variance which are both user defined parameters. To create an example realization of this spectrum, the formulation developed by Shinozuka is used for a multivariate stochastic process[106]. In this process, the spectrum function is sampled at a number of discrete waves and summed over the entire 3D space. The spatial realization is shown in equation (49)

$$V_m(\vec{r}) = \sum_{n=1}^{m} \sum_{k_1=1}^{NW} \sum_{k_2=1}^{NW} \sum_{k_3=1}^{NW} |P_{mn}(\vec{\Omega}_k)| \sqrt{2\Delta\Omega}\ cos(\vec{\omega}_k^T \vec{r} + \Phi_{nk}) \tag{49}$$

where $\vec{r}$ is the position vector in inertial space, NW is the number of waves sampled, and $\mathbf{P}$ is the spectral factorization of the spectrum function such that $\mathbf{\Theta} = \mathbf{P}\mathbf{P}^*$. P_{mn} is then the mth row and nth column of this matrix. The spectral factorization is completed using the Cholesky decomposition[107]. The parameter Φ_{nk} is a uniform random number from 0 to 2π. Note that $m = 1$ gives $V_x(\vec{r})$,$m = 2$ gives $V_y(\vec{r})$ and $m = 3$ gives $V_z(\vec{r})$. Finally, the following supplemental equations are used

$$\begin{aligned}
\vec{\Omega}_k &= \Omega_{1k_1}\hat{I}_I + \Omega_{2k_2}\hat{J}_I + \Omega_{3k_3}\hat{K}_I \\
\Omega_{mk_m} &= \Omega_{mL} + (k_m - 0.5)\Delta\Omega_m \\
\Delta\Omega_m &= (\Omega_{mU} - \Omega_{mL})/N \\
\vec{\omega}_k &= \omega_{1k_1}\hat{I}_I + \omega_{2k_2}\hat{J}_I + \omega_{3k_3}\hat{K}_I \\
\omega_{mk_m} &= \Omega_{mk_m} + \delta\Omega_m
\end{aligned} \tag{50}$$

where Ω_{mU} and Ω_{mL} are upper and lower bounds of the wave computed and $\delta\Omega_m$ is a random number that is smaller than the distance between discrete waves. This is a user parameter that randomizes the wave frequency in the summation. Rather than using equation (49) during the simulation to compute the turbulence, the turbulence field is realized ahead of time and is interpolated at each timestep using a 3D table lookup. Figure 22 shows an example wind profile for 3 different scenarios. The plot on the left only contains the WRF model at an intensity of 1.0 with a length scale of $1530m$. The plot in the middle only contains the Dryden turbulence model at an intensity of 1.0. The plot on the right is simply the sum of the

two plots on the left. The wind components plotted are taken at the center of gravity of an aircraft flying at a nominal $20m/s$. The components U, V, W are the inertial components of the atmospheric wind velocity. This Figure shows that the wind model used in this simulation contains low frequency spatial gusts as well as turbulence to represent a realistic wind environment.

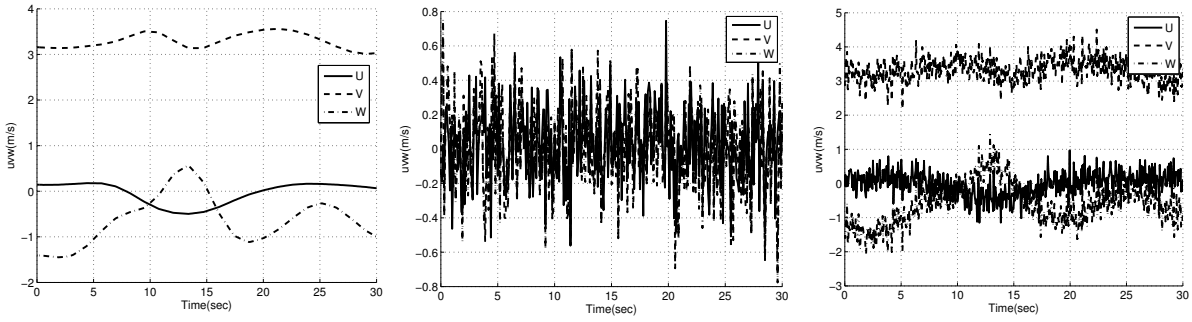

Figure 22: Wind Speed Components for Different Wind Models(m/s) vs. Time(sec)

2.7 Simulation Setup

To explore the flight dynamics of meta aircraft, an example small aircraft is used for all simulation results. The example aircraft utilizes the aerodynamics and mass properties of a single propeller, high wing conventional aircraft as reported by [81]. The mass of each aircraft is 5.6 kg. The mass moments of inertia are $Ixx = 0.4923\ kg\ m^2$, $Iyy = 0.5111\ kg\ m^2$, and $Izz = 0.8470\ kg\ m^2$. The main wing has a 2.04 m span and a 0.3215 m chord with a cambered airfoil (NACA 1412) with a maximum thickness of $t = 0.0386\ m$. The lift coefficient at zero angle of attack is 0.062 and the lift slope is 5.195/rad. The horizontal tail is 0.72 m in span with a 0.295 m chord. The vertical tail has a half span of 0.305 m and a chord of 0.25 m. Both horizontal and vertical tails use symmetric airfoils and are positioned 1.4 m from the center of mass of the aircraft. The aircraft uses a conventional control layout with an elevator to control pitch, ailerons to control roll angle, rudder to control sideslip and a propeller for thrust. This aircraft has a nominal flight speed of $20m/s$. A single magnet is placed at the connection joint of each aircraft. This magnet has a maximum force of $1000N$ with dimensions $101.6 \times 25.0 \times 20.2\ mm$ and weighs approximately $380g$.

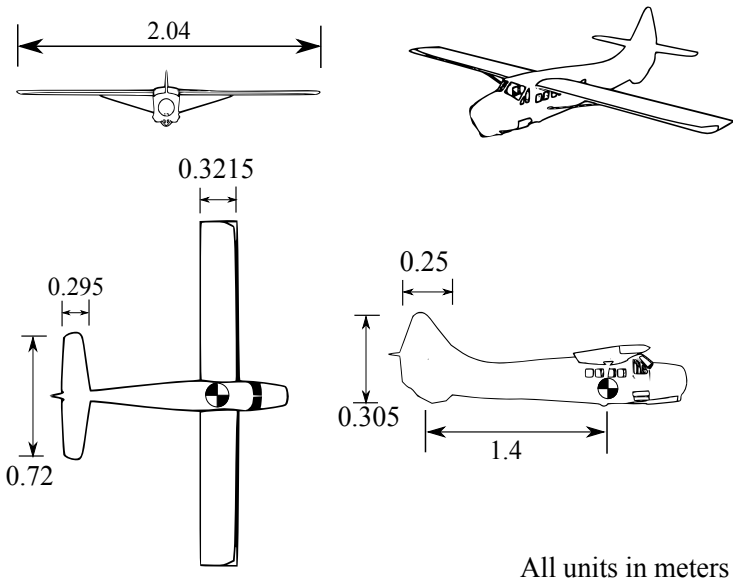

Figure 23: Aircraft Three-View

In order to approximate joint characteristics of connected aircraft, the linear springs and dampers have been set to be relatively stiff. Thus, the linear spring and damper constants have been set to $10,000 N/m$ and $40 N-s/m$ respectively. The rotational springs and dampers have been set to be relatively soft to allow relative rotation between each aircraft. The values of the roll, pitch and yaw stiffness are 370 $N-m/rad$,2580 $N-m/rad$, and 2580 $N-m/rad$ respectively. The roll, pitch and yaw damping are 1.5 $N-m-s/rad$,10 $N-m-s/rad$, and 10 $N-m-s/rad$ respectively.

The fuselage aerodynamic coefficients are obtained using a numerical fitting procedure so that the forces and moments due to all lifting surfaces and the fuselage are equal to the forces and moments produced by the full aerodynamic expansion given by [81]. This ensures that the single aircraft has the same dynamics regardless of the number of lifting elements used. For example, if the number of lifting elements is set to zero, the fuselage coefficients converge to the full aerodynamic expansion given by [81]. All of the results presented in this dissertation were computed for 3, 5 and 7 elements on the main wing and no significant difference was found.

Note that no propeller aerodynamic wash is modeled in the simulation. Thus, the results simply hold in

the confines of this dynamic model. It may be that the dynamics may alter slightly for tip to tail aircraft if propeller wash is included in the analysis. It is hypothesized that no significant change would occur for wing tip to wing tip connected flight.

The WRF model was compiled to create a 3-D large eddy simulation (LES) with a convective boundary layer (CBL) over a flat terrain with the full suite of physics options enabled. The initial temperature is defined as 300 K with a surface heat flux of 0.3 $Watts/m^2$. The surface heat flux is used to maintain the CBL over time. The LES simulation has zero initial gusts, therefore, the simulation computes 30 minutes of simulated data to allow large scale atmospheric features to develop. After this initialization period a snapshot of data is taken for use in the aircraft simulation. This snapshot assumes that the speed of the aircraft is faster than the time-varying component of the WRF model so that a frozen field model can be used to reduce computation time. The simulation grid spans a 1 km cube with 25 meter resolution. An initial wind profile is required to start the simulation using data taken during airdrop tests to initialize the horizontal wind components over the entire simulation grid[36]. The mean wind speed is about 4m/s and varies with altitude.

In this model formulation, the assumption of high altitude turbulence is made thus $L = 1530m$ and $\sigma = 1$. The turbulence model is outputted at a grid size of $1m$. The upper and lower spatial frequency bounds of the wind field turbulence spectrum are set to $20rad/m$ and $-20rad/m$ respectively with $NW = 70$. Note that the Dryden turbulence model and the WRF model can be scaled independently to achieve different atmospheric wind fields. When the WRF scale is equal to 1 the mean wind is about $4m/s$ with a standard deviation of $0.2m/s, 0.2m/s$ and $0.5m/s$ along V_x, V_y and V_z respectively. When the turbulence intensity is equal to 1 the mean wind is $0m/s$ with a standard deviation of $0.25m/s$. For most cases, the turbulence intensity and WRF scale are set to the same value so that the maximum value of turbulence is 10% of the mean wind as customary for atmospheric turbulence.

3 Meta Aircraft Flight Dynamics

The following section explores the flight dynamics of meta aircraft configurations with a focus on the flight dynamic modes and mode shapes. This chapter begins with the flight dynamic modes of motion for meta aircraft and then moves on to the flexible modes of motion for meta aircraft. The example aircraft used in the following simulations is detailed in Section 2.7. Note, that the simplified contact model defined in Section 2.5 is used in this chapter.

3.1 Flight Dynamic Modes of Motion for Meta Aircraft

To obtain the flight dynamic modes of motion of the meta aircraft system, the trim state of a connected meta aircraft configuration is obtained through a controller that uses elevator inputs to track a prescribed altitude, thrust inputs to track a desired flight speed, aileron inputs to balance roll moments, and rudder commands to balance yaw moments. Using this control law, the equations of motion are simulated until all state derivatives (except $\dot{x}_i$) are less than 1e-8. This trimming procedure was found to work robustly for all configurations examined.

Once the trim state of each configuration is found, a linear time invariant model is obtained numerically using forward finite differencing to compute the Jacobian of the nonlinear model[85]. Each state is perturbed from trim by 1e-6 to compute numerical derivatives. A $12N_{AC}$ state linear time invariant dynamic model results with $12N_{AC}$ associated eigenvalues (modes) and eigenvectors (modeshapes). For 4 aircraft composing the meta aircraft configuration the linear model has 48 states. For a body in free flight, 12 of these modes and modes shapes are associated with standard rigid aircraft flight dynamic motion of the entire meta aircraft configuration. These are relatively low frequency and are associated with the global flight dynamic behavior of the aircraft. They involve the classical phugoid, short period, dutch roll, spiral, and roll modes[85,84]. The remaining modes in the linear time invariant model are associated with the flexible modes of motion. The flight dynamic modes of a single aircraft are shown in Figure 24. Specifically, the short period mode is $(-5.92 \pm 9.22i)$, the phugoid mode is $(-0.032 \pm 0.61i)$, the roll mode is (-16.93), the dutch roll mode is

$(-0.42 \pm 2.31i)$ and the spiral mode is (-0.029).

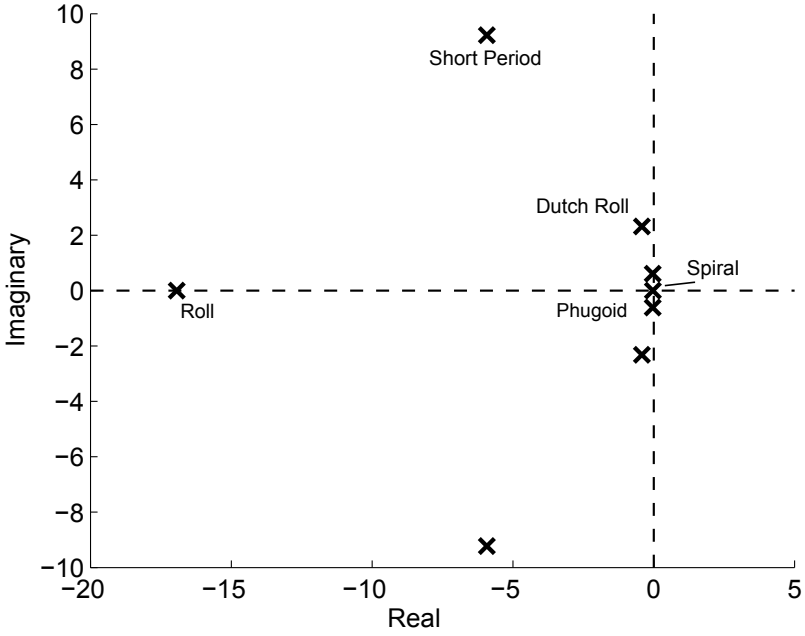

Figure 24: Single Aircraft Flight Dynamic Modes

The same analysis above is conducted for aircraft connected tip to tail and wing tip to wing tip. In order to establish a pattern, 5 aircraft are examined for both wing tip to wing tip and tip to tail connected flight. To understand the physical and aerodynamic changes when aircraft are connected together, the results from the nonlinear model are compared to analytical expressions by Phillips[85]. It is possible to obtain analytic expressions for each flight dynamic mode; however, these analytic expressions require the full aerodynamic expansion of an aircraft rather than the split aerodynamic model used in this formulation. In order to use these expressions the meta aircraft is assumed to act as a rigid body and equivalent aerodynamic coefficients are obtained. Equations can be created for all longitudinal and lateral coefficients and used in approximate flight dynamic expressions[85]. It is assumed that the geometry of the meta aircraft can be scaled, such that the planform area of the entire system $S_T = N_{AC}S$. Similarly, for wing tip to wing tip connected flight, the wing span is $b_T = N_{AC}b$ however the chord is kept constant. In tip to tail connected flight $c_T = N_{AC}c$ and the span is kept constant.

Finally, the pitch, roll and yaw inertias are computed using the parallel axis theorem. It is easy to see that in wing tip to wing tip connected flight the pitch inertia increases linearly while the roll and yaw inertias increase quadratically. Conversely, in tip to tail connected flight the roll inertia increases linearly with number of connected aircraft and the yaw and pitch inertias increase quadratically. Using the equations for geometry, mass, inertia and equivalencing the overall aerodynamic coefficients, analytical expressions in [85] can be used to compute the flight dynamic modes. The results of these equations are plotted alongside the numerical results for wing tip to wing tip connected flight and tip to tail connected flight. This analysis is thus capable of analyzing fractionated aircraft and a smooth root locus can be generated and plot and plotted alongside the discrete numerical modes. Note that there will be slight differences between the numerical model and the approximate solution. This is due to the assumptions made to arrive at these analytical expressions.

Figure 25 shows the change in the short period mode. Each discrete point is the addition of an extra aircraft as shown by the number above each pole. The short period mode is a relatively fast mode that can be excited by a step change in the elevator. The aircraft exhibits a quick oscillation about the pitch axis which quickly damps out. The short period mode is largely unchanged for wing tip to wing tip connected flight which is expected as this is a pure longitudinal mode. However, the short period mode changes drastically for tip to tail connected flight and even causes the mode to become critically damped once there are 3 or more aircraft connected together. Figure 90 indicates a similar change in the phugoid mode. Just as in the short period mode a negligible change is seen for wing tip to wing tip flight versus a drastic change in tip to tail flight. The underlying physical phenomenon can be explained by examining the change in geometry and aerodynamics. In wing tip to wing tip connected flight, the pitch inertia of the aircraft increase linearly as well as the overall planform area. In addition, when the aircraft pitches about the y-axis it is a symmetric pitch. That is, the overall pitch rate of the entire meta aircraft is equal to the pitch rate of each individual aircraft. In addition, the angle of attack of each aircraft is identical. These effects cause all meta aircraft longitudinal coefficients to be constant with respect to the number of connected aircraft resulting in nearly identical short period and phugoid modes.

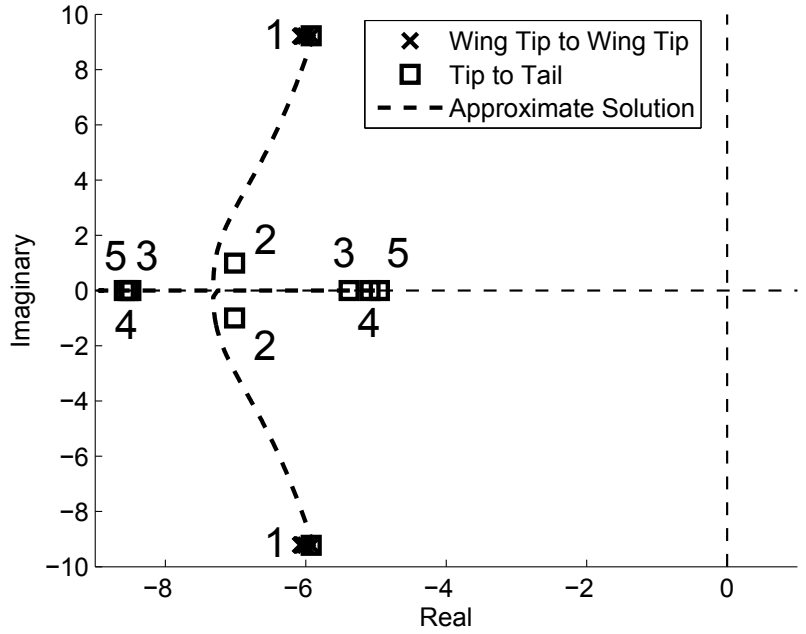

Figure 25: Short Period Mode as a Function of Number of Connected Aircraft

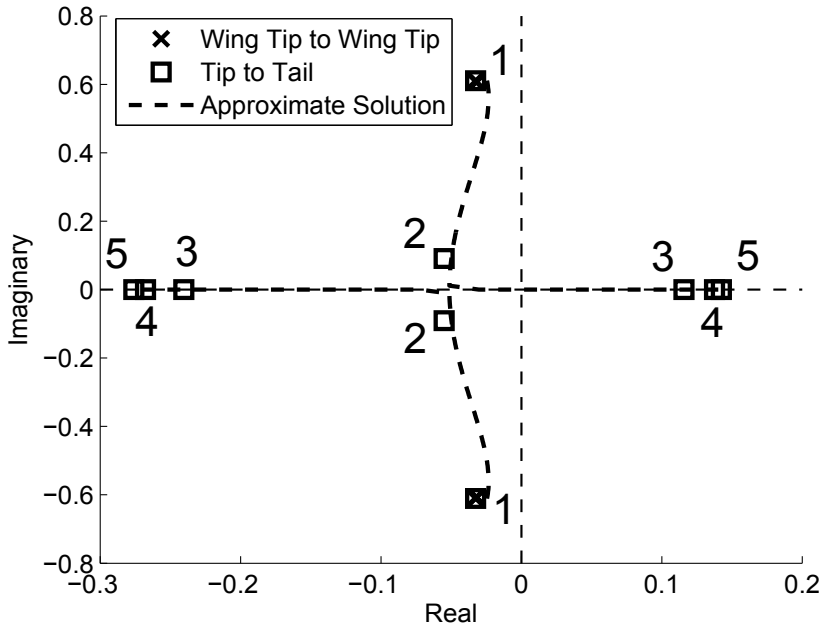

Figure 26: Phugoid Mode as a Function of Number of Connected Aircraft

The tip to tail configuration, has a different aerodynamic and geometric change. First, the pitch inertia increases quadratically rather than increasing linearly. Aerodynamically, an overall pitch rate on the meta aircraft results in a non uniform angle of attack on all aircraft. That is, a positive pitch rate leads to an increase in angle of attack on trailing aircraft and a decrease in angle of attack on leading aircraft. This effect causes the pitch damping coefficient to change. This change in pitch damping, coupled with the increase in pitch inertia causes the longitudinal modes to become critically damped after 2 aircraft. In addition to becoming critically damped, the phugoid mode becomes unstable. Since this is a mode along the pitch axis, this mode can be seen as a slow and unstable increase in pitch. The changes in longitudinal modes also show a key result and that is the pitch symmetry of wing tip to wing tip connected flight. Tip to tail connected flight has a similar axis of symmetry along the roll axis resulting in a nearly constant roll mode. However, because the trailing aircraft are flying in the wake of the leading aircraft, the roll damping coefficient actually drops slightly resulting in a drop in the roll mode for tip to tail flight as depicted in Figure 27.

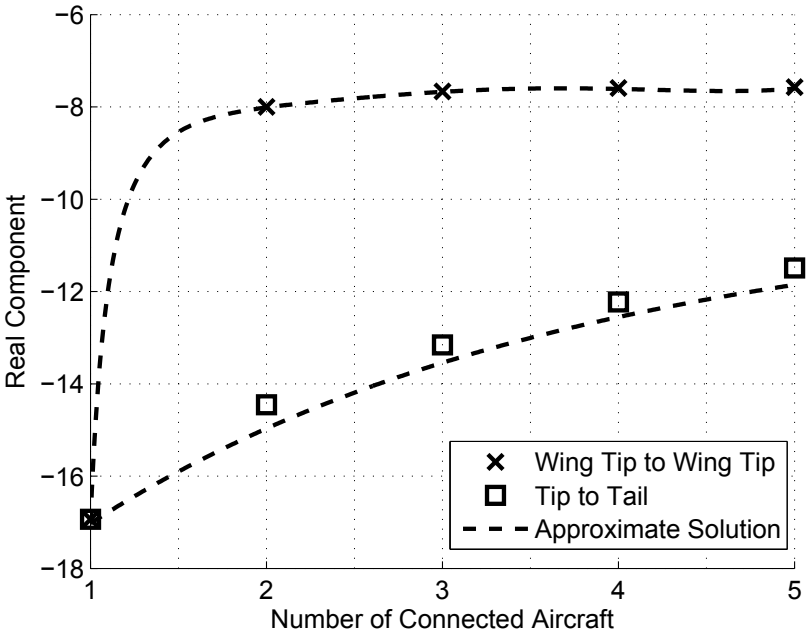

Figure 27: Roll Mode as a Function of Number of Connected Aircraft

Wing tip to wing tip connected flight actually creates an increase in roll damping due to the aerodynamic

center offset of each aircraft from the center of mass. However, since the roll inertia of the wing tip to wing tip meta aircraft increases quadratically, the roll mode eigenvalue actually decreases. After about 2 to 3 connected aircraft, these two effects cancel each other out and the roll mode stays constant. The remaining 2 modes involve sideslipping, rolling and yawing motion. As such, these modes exhibit some longitudinal and lateral dynamic coupling which causes these modes to change for both wing tip to wing tip and tip to tail connected flight. Figure 28 depicts the change in the dutch roll mode.

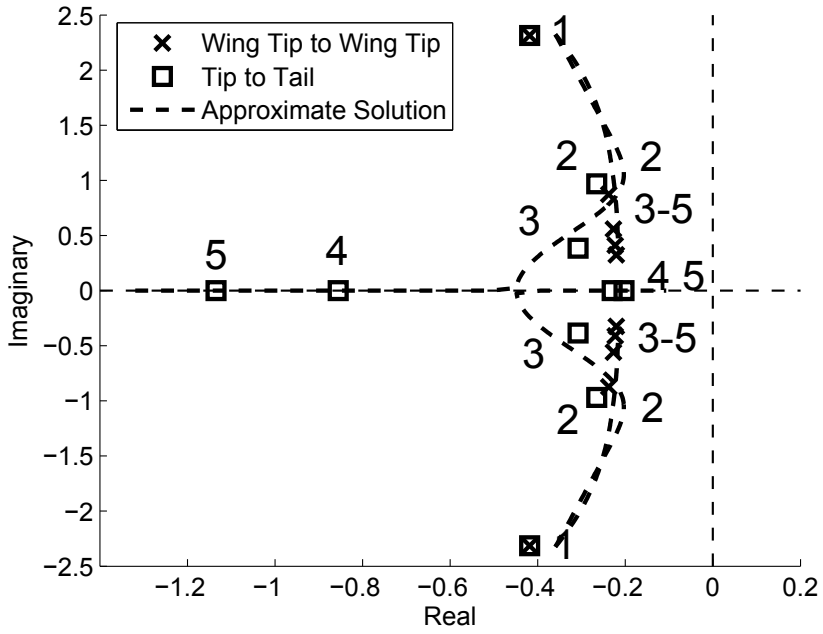

Figure 28: Dutch Roll Mode as a Function of Number of Connected Aircraft

The tip to tail configuration causes this mode to become critically damped similar to the phugoid mode. The underlying physical phenomena is mainly caused by the increase in the magnitude of the yaw damping coefficient. Notice, that the phugoid mode becomes critically damped for tip to tail connected flight due to a similar increase in the pitch damping coefficient. Similarly, the yaw damping coefficient increases causing the dutch roll mode to become critically damped. In addition, the yaw and pitch moments of inertia increase quadratically with the number of connected aircraft. These two effects lead to critically damped dutch roll and longitudinal modes. Wing tip to wing tip connected flight does not exhibit a large increase in yaw

damping but rather an increase in roll damping. This increase in roll damping coupled with an increase in the roll and yaw moments of inertia lead to increased damping in the dutch roll mode.

The final lateral mode, the spiral mode, changes most significantly for tip to tail connected flight as shown in Figure 29. The mode becomes more convergent for 2 aircraft and then becomes more unstable with each added aircraft. Wing tip to wing tip connected flight however, has a smooth increase in the mode moving from -0.0288 for the single aircraft and 0.0282 for 5 connected aircraft.

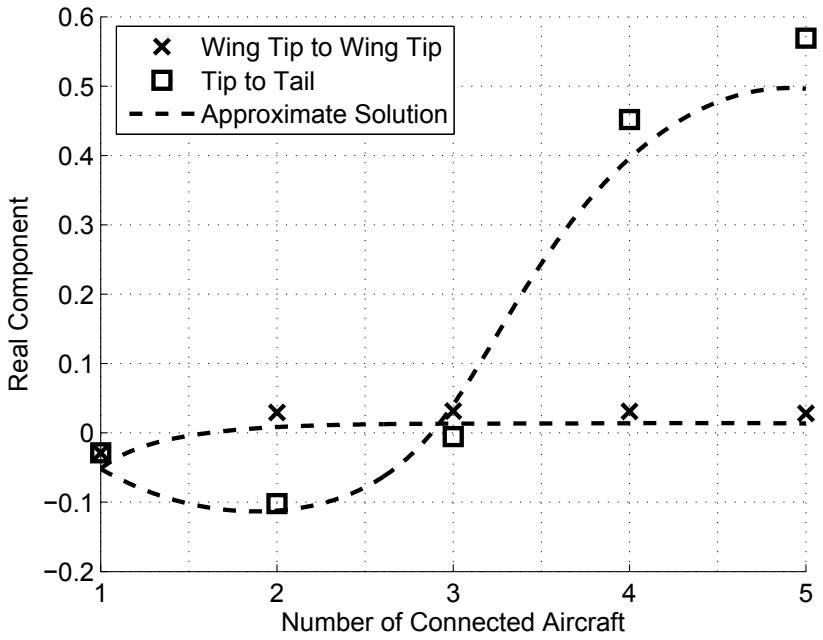

Figure 29: Spiral Mode as a Function of Number of Connected Aircraft

The change in this mode can be explained by examining the approximate solution for the spiral mode given by equation (51)[85].

$$\lambda = -\frac{g}{V_T}\frac{C_{L\beta_T}C_{NR_T} - C_{LR_T}C_{N\beta_T}}{C_{L\beta_T}C_{NP_T} - C_{LP_T}C_{N\beta_T}} \tag{51}$$

In this equation, the total meta aircraft velocity (V_T) is very insensitive to the number of connected aircraft. This mode is thus effected by the roll and yaw coefficients due to sideslipping, rolling and yawing. It has already been discussed that the roll damping coefficient increases significantly for wing tip to wing

Table 1: Flight Dynamic Modes for Meta Aircraft

			WingTip to Wing Tip					Tip to Tail				
		Number of Aircraft	1	2	3	4	5	1	2	3	4	5
MODES	Short Period	Root (Approximate)	-5.88+9.283i	-5.968+9.268i	-6.005+9.262i	-6.026+9.258i	-6.039+9.255i	-5.88+9.283i	-7.299+0.926i	-8.896 -5.496	-8.921 -5.171	-8.759 -5.016
		Root (Numerical)	-5.922+9.224i	-6.007+9.216i	-6.045+9.214i	-6.062+9.209i	-6.075+9.208i	-5.922+9.224i	-7.014+0.996i	-8.491 -5.383	-8.584 -5.086	-8.522 -4.954
		Natural Frequency	10.961	11.001	11.02	11.025	11.031	10.961	7.084	6.761	6.607	6.498
		Damping	0.54	0.546	0.549	0.55	0.551	0.54	0.99	1.026	1.034	1.037
	Phugoid	Root (Approximate)	-0.024+0.611i	-0.024+0.609i	-0.024+0.608i	-0.024+0.608i	-0.024+0.607i	-0.024+0.611i	-0.05+0.077i	-0.239 0.123	-0.266 0.145	-0.273 0.149
		Root (Numerical)	-0.033+0.611i	-0.032+0.608i	-0.032+0.608i	-0.032+0.607i	-0.032+0.607i	-0.033+0.611i	-0.055+0.091i	-0.24 0.116	-0.268 0.138	-0.276 0.142
		Natural Frequency	0.612	0.609	0.609	0.608	0.608	0.612	0.106	0.167	0.192	0.198
		Damping	0.054	0.053	0.053	0.053	0.053	0.054	0.517	1.067	1.056	1.056
	Dutch Roll	Root (Approximate)	-0.36+2.324i	-0.223+0.874i	-0.218+0.558i	-0.216+0.411i	-0.214+0.325i	-0.36+2.324i	-0.204+1.034i	-0.324+0.527i	-1.024 -0.129	-1.335 -0.112
		Root (Numerical)	-0.418+2.315i	-0.238+0.874i	-0.227+0.558i	-0.223+0.411i	-0.221+0.324i	-0.418+2.315i	-0.265+0.968i	-0.308+0.385i	-0.856 -0.23	-1.135 -0.203
		Natural Frequency	2.352	0.906	0.602	0.468	0.392	2.352	1.004	0.493	0.444	0.48
		Damping	0.178	0.263	0.377	0.477	0.563	0.178	0.264	0.625	1.224	1.394
	Roll	Root (Approximate)	-17.023	-8.012	-7.674	-7.611	-7.604	-17.023	-14.968	-13.544	-12.553	-11.854
		Root (Numerical)	-16.934	-8.001	-7.664	-7.593	-7.572	-16.934	-14.454	-13.157	-12.225	-11.489
	Spiral	Root (Approximate)	-0.052	0.008	0.013	0.014	0.013	-0.052	-0.112	0.041	0.396	0.496
		Root (Numerical)	-0.029	0.029	0.032	0.031	0.028	-0.029	-0.102	-0.005	0.452	0.569

tip connected flight and decreases slightly for tip to tail connected flight. In addition, the yaw damping coefficient increases in magnitude for tip to tail connected flight while remaining largely constant for wing tip to wing tip connected flight. The roll moment due to sideslip decreases slightly for wing tip to wing tip connected flight but remains negative. This coefficient however changes sign for tip to tail connected flight again due to the trailing aircraft flying in the wake of the leading aircraft. All of these effects coupled with similar changes in other lateral coefficients leads to this change in the spiral mode. Table 1 contains a comprehensive list of all flight dynamic modes as a function of connected aircraft along with the approximate solution from Phillips[85].

Another interesting result is to examine the static stability of wing tip to wing tip connected flight and tip to tail connected flight. It was shown previously that the phugoid mode for tip to tail connected flight becomes unstable but this is a dynamic instability. Figure 30 shows the change in $C_{m\alpha}$ for wing tip to wing tip connected flight and tip to tail connected flight. This Figure shows that when connecting aircraft wing tip to wing tip the pitch moment slope stays constant as expected. However, when connected tip to tail the pitch moment slope become positive. This indicates a static instability for tip to tail connected flight.

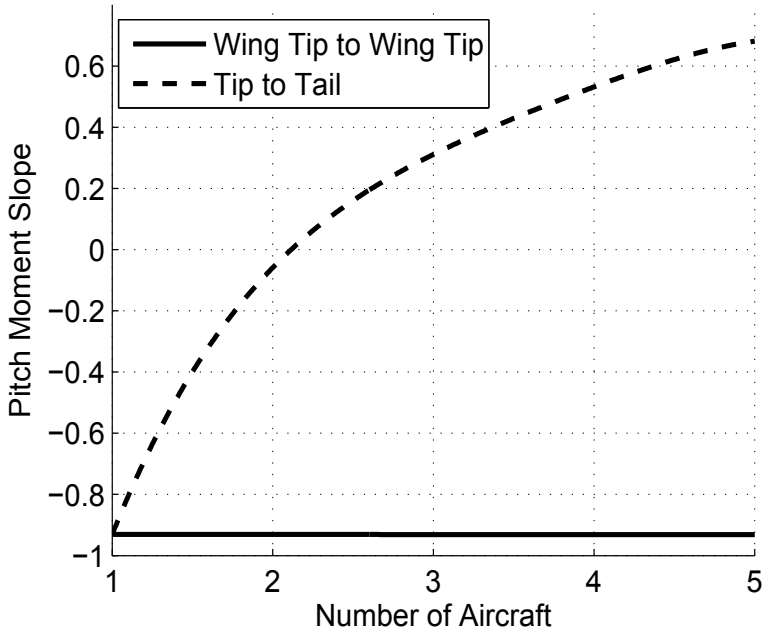

Figure 30: Pitch Moment Slope vs. Number of Connected Aircraft

3.2 Flexible Modes of Motion for Meta Aircraft

In addition to changing the flight dynamic modes of motion, meta aircraft systems also contain flexible modes. These flexible modes are a direct result of relative motion at the joints that connect aircraft. For the 4 aircraft system, the linear time invariant model contains 48 states. Section 4.2 described the 12 flight dynamic modes of motion. The remaining 36 modes are associated with translational flexible modes (18 eigenvalues) and rotational flexible modes (18 eigenvalues). This section deals with the modes associated with relative rolling, pitching and yawing between each connected aircraft resulting in $3(N_{AC}-1)$ modes with $6(N_{AC}-1)$ eigenvalues. The joint characteristics are set such that the translational spring and damper constants are relatively stiff such that the translational flexible modes are high in frequency. Due to this high frequency and minimal translation along the x,y and z axes the translational flexible modes are not discussed in detail. Motion along each axis is given a name based on the axis of rotation. For wing tip to wing tip connected flight, roll motion is called flapping, pitch motion is called the twisting (pitch) mode

and yaw motion is called the lead lag mode, which are names taken from the rotorcraft sector. For tip to tail connected flight, roll motion is called the twisting (roll) mode whereas pitch and yaw motion are called porpoising and snaking modes named after their animal like motions. Figures 31 and 32 show the flexible modes of wing tip to wing tip flight and tip to tail flight separated by motion along the yaw plane, pitch plane and roll plane for 4 aircraft.

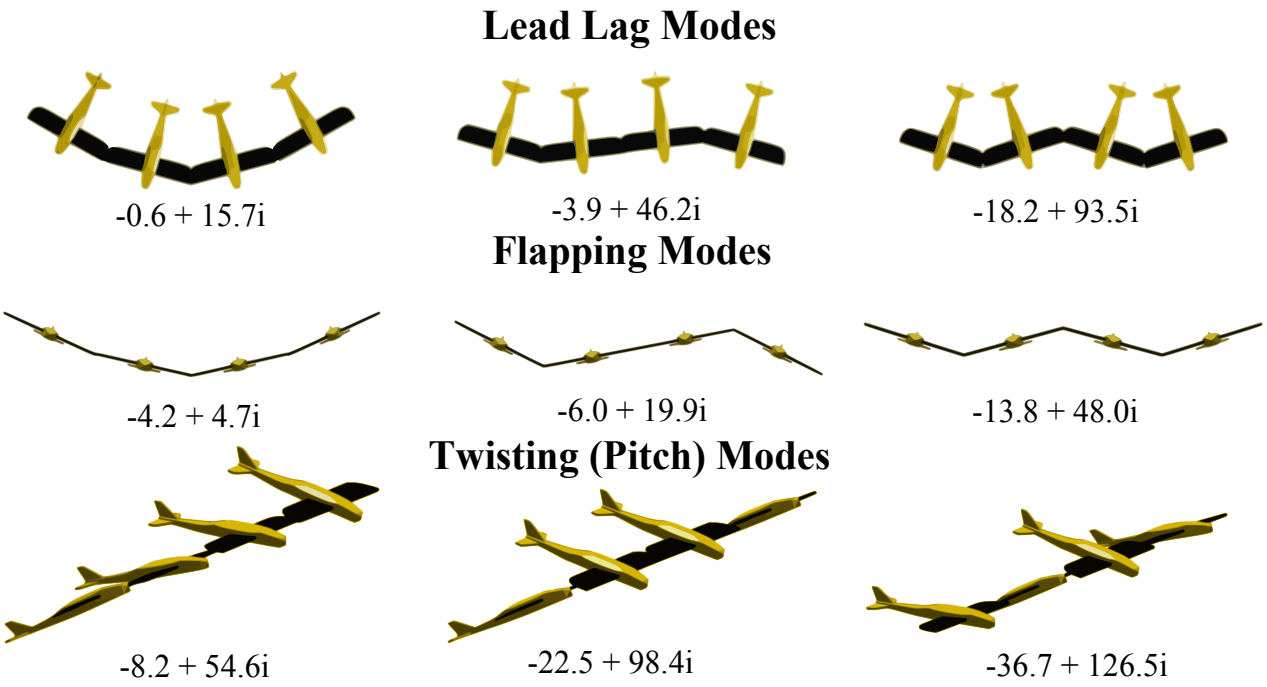

Figure 31: Flexible Wing Tip to Wing Tip Modes

The numbers below each graphic show the eigenvalue of each mode. As mentioned previously, the number of flexible rotational modes is equal to $3(N_{AC} - 1)$. For 4 connected aircraft, there are a total of 9 flexible modes with 3 modes along each rotational axis. For each configuration, the rows represent each axis of relative motion and the columns are split into the lowest and highest natural frequencies. The highest frequency mode is characterized by alternating angles between each aircraft. For example, in Figure 31 the fastest lead lag mode is characterized by the first aircraft having a positive yaw angle and the second having a negative yaw angle. This pattern is repeated for the next two aircraft. Each aircraft is 180 degrees out of phase with the aircraft to its left and to its right. Similarly, the flapping modes alternate their roll angles

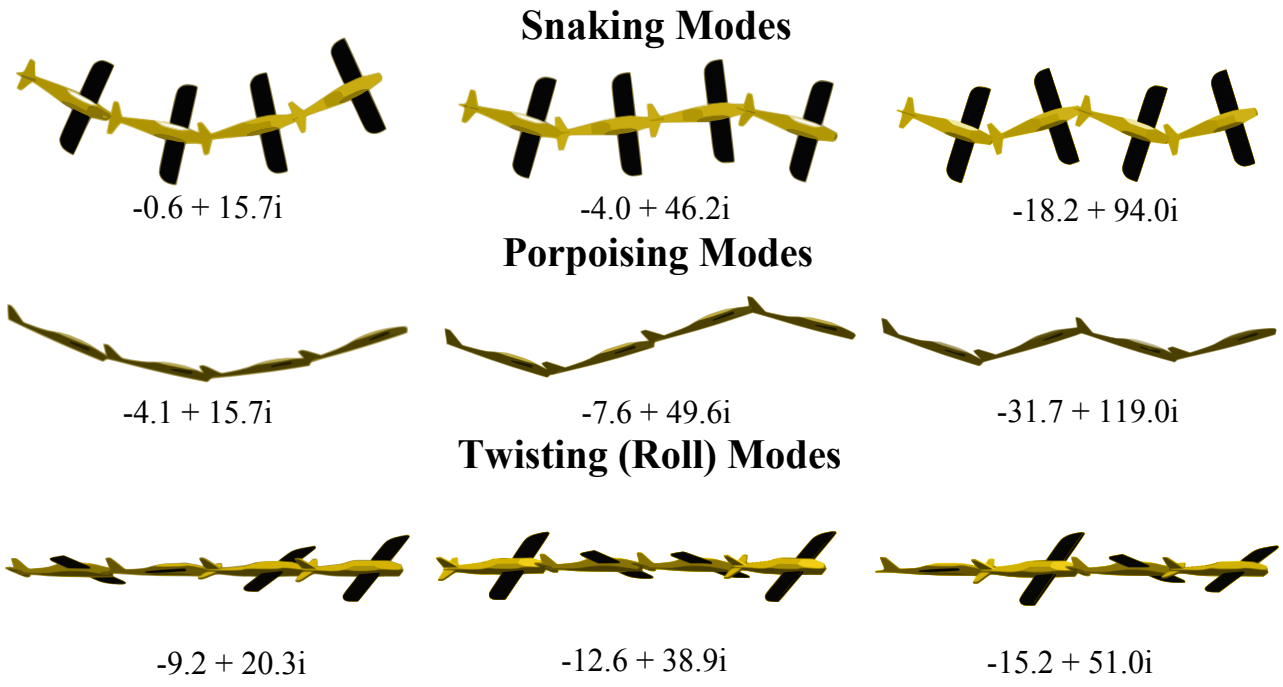

Figure 32: Flexible Tip to Tail Modes

and the twisting (pitch) modes alternate their pitch angles. The middle column is characterized by the two outside aircraft oscillating in phase whereas the other two middle aircraft oscillate 180 degrees out of phase. The low frequency flexible mode places an axis of symmetry between the second and third aircraft. Aircraft one and two oscillate in phase with varying magnitudes while aircraft three and four oscillate out of phase with aircraft one and two.

3.3 Effect of Meta Aircraft Connection Characteristics

Notice that the flexible modes of motion contain all complex modes. The frequency and damping of these modes can be altered by changing the joint characteristics. For example, if stiffness is added to the roll axis of the joint for the wingtip to wingtip configuration, the flapping modes will have higher frequencies. In order to highlight the changes to the flexible modes, the rotational springs and dampers are varied for 2 aircraft connected wing tip to wing tip and root locus plots are created to show the change in lead lag, twist (pitch), and flapping modes. Since there are only 2 aircraft connected, the number of flexible

modes is 3, which makes the analysis much simpler. Tip to tail aircraft exhibit similar changes in the flexible modes but is not analyzed in this dissertation. The nominal value of the rotational springs are 370 $N-m/rad$, 2580 $N-m/rad$, and 2580 $N-m/rad$ along the roll, pitch and yaw axes respectively. The rotational dampers are 1.5 $N-m-s/rad$, 10 $N-m-s/rad$, and $10N-m-s/rad$ along the roll, pitch and yaw axes respectively. The linear springs and dampers are held constant throughout this section at $10000N/m$ and $40N-s/m$ respectively. Using these nominal values of springs and dampers, the nominal values of the three flexible modes are shown in Figure 33.

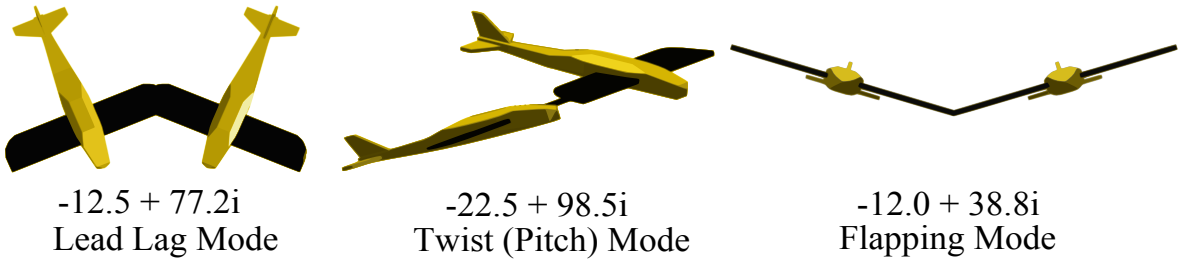

Figure 33: Flexible Modes for Two Aircraft Connected Wing Tip to Wing Tip

Figure 34 shows a root locus of all three flexible modes where K_ϕ is varied from 1 to 1000 $N-m/rad$. Increasing K_ϕ is analogous to adding stiffness to the aircraft joint along the roll axis such that the aircraft resists rolling and acts to keep the roll angles of each aircraft the same. As such, the flapping mode moves from critically damped to an oscillatory mode with two complex conjugate pairs. In addition, adding stiffness to the roll axis has no significant effect on the twist (pitch) and lead lag modes highlighting the decoupled nature of these three flexible modes. In addition, this study shows that if a different flapping frequency is desired the designer merely must change the roll stiffness of the connection joint.

A similar result can be seen when varying the rotational stiffness about the pitch and yaw axes (K_θ, K_ψ). Figures 35 and 36 show the effect of varying these two spring constants. When varying K_θ, the flapping and lead lag modes remain at their nominal values while the twist (pitch) mode changes significantly. When varying K_ψ, the twist (pitch) and flapping modes remain at their nominal values while the lead lag mode changes significantly. Notice that when varying the rotational stiffness the primary effect is for the imaginary component to change. At a certain point the mode switches from being critically damped mode to oscillatory.

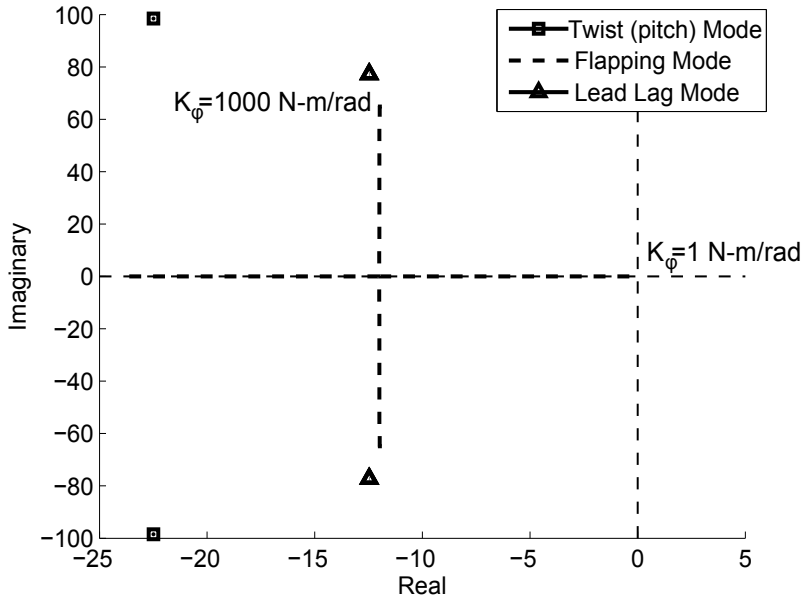

Figure 34: Change in Flexible Modes as a Function of Roll Stiffness(K_ϕ)

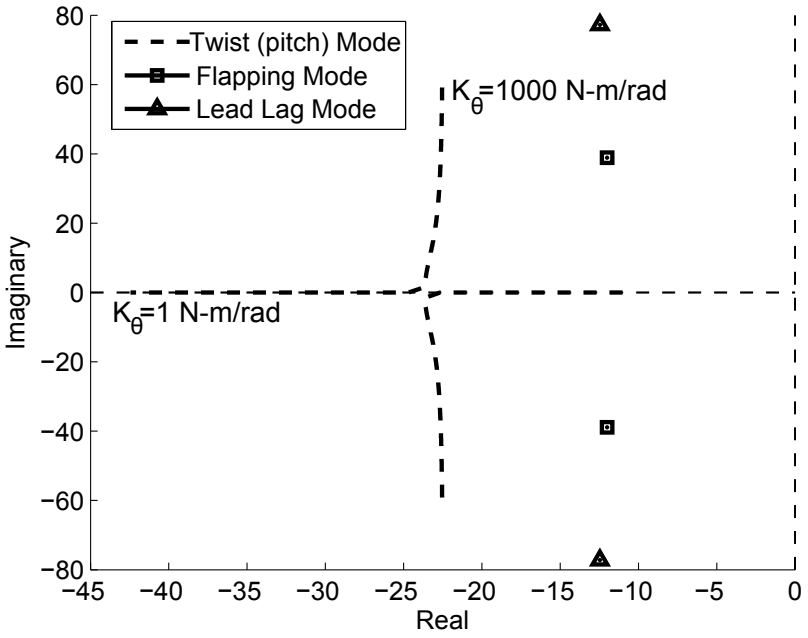

Figure 35: Change in Flexible Modes as a Function of Pitch Stiffness(K_θ)

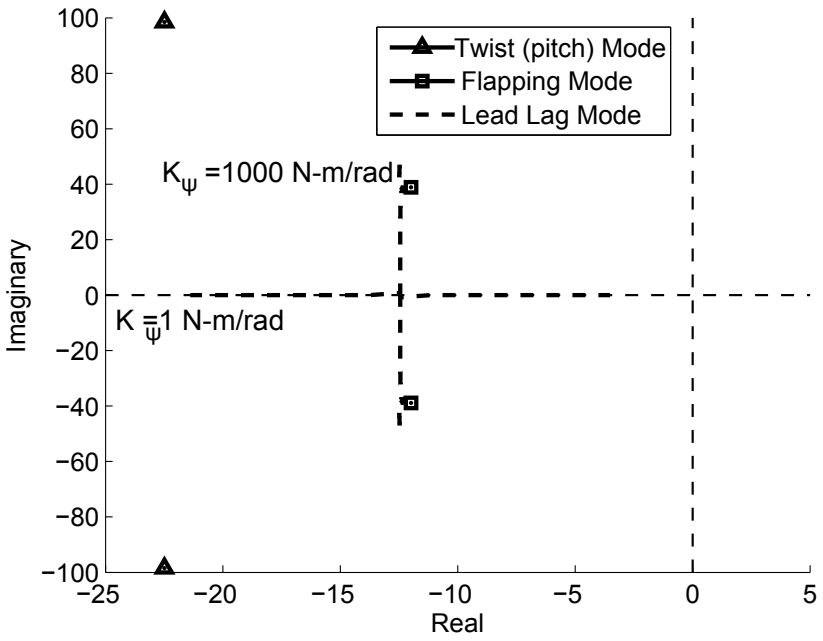

Figure 36: Change in Flexible Modes as a Function of Yaw Stiffness(K_ψ)

Similar effects can been seen when varying the damping coefficients along all three axes. Figures 37-39 show the root locus plots when varying the rotational damping coefficients C_ϕ, C_θ and C_ψ. Notice that all flexible modes can be switched from critically damped modes to oscillatory modes by changing the damping coefficients at the joint.

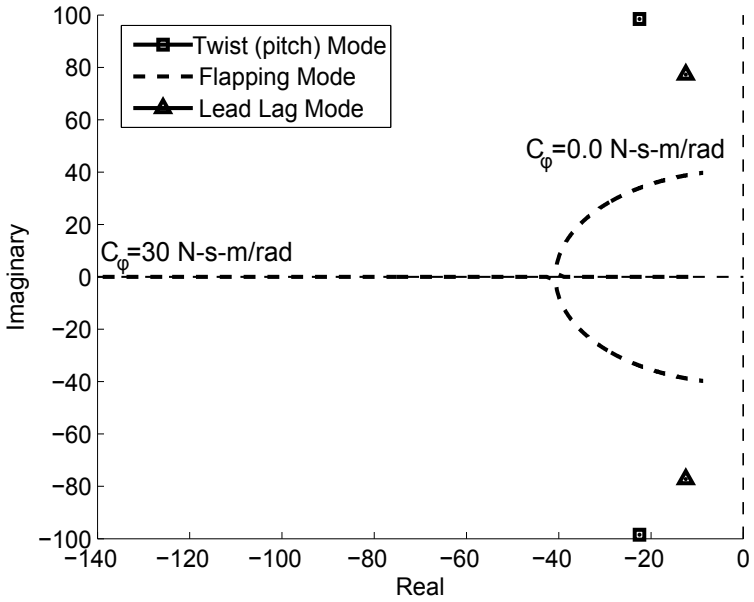

Figure 37: Change in Flexible Modes as a Function of Roll Damping(C_ϕ)

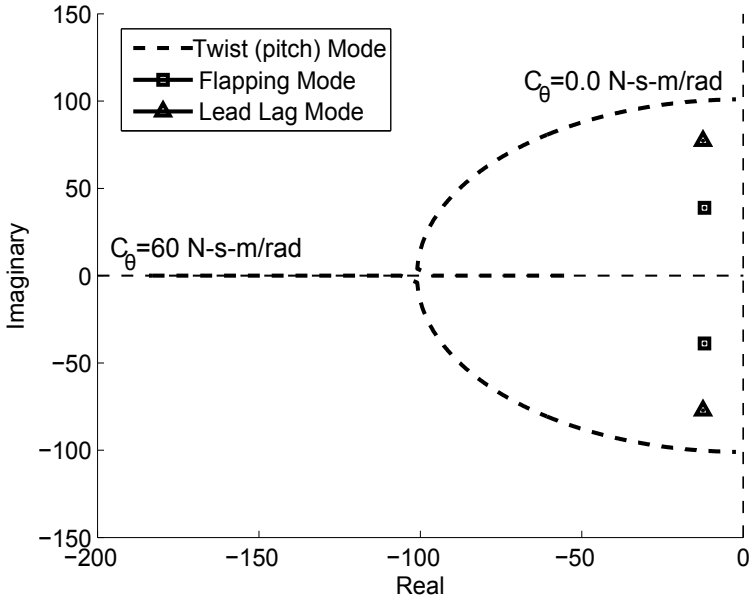

Figure 38: Change in Flexible Modes as a Function of Pitch Damping(C_θ)

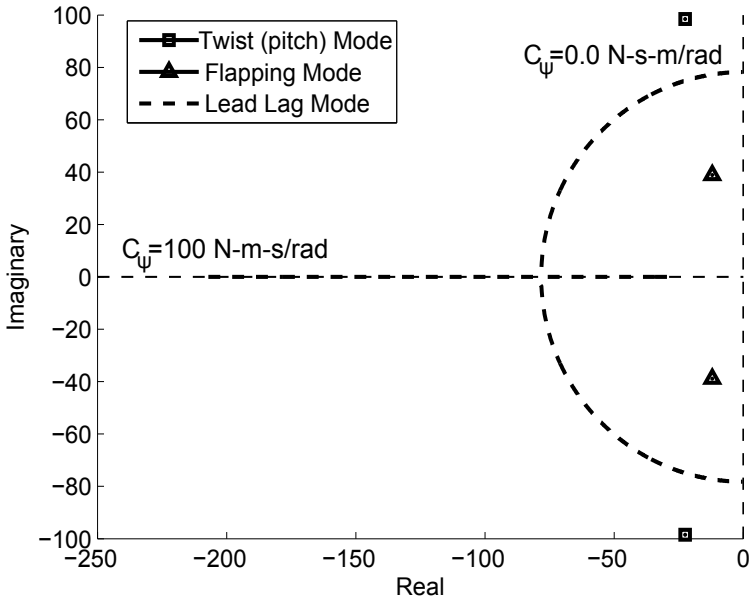

Figure 39: Change in Flexible Modes as a Function of Yaw Damping(C_ψ)

Each of these flexible modes can be modeled assuming a single degree of freedom excited by an external torque function, aerodynamic damping, and rotational springs and dampers. The single degree of freedom equations are shown below for the twisting (pitch) mode.

$$J_\theta \ddot{\theta} = -K_\theta \theta - (C_\theta + C_A)\dot{\theta} + T_\theta(t) \tag{52}$$

where J_θ is the equivalent rotational inertia along the pitch axis, K_θ and C_θ are the joint rotational springs and dampers, C_A is an equivalent aerodynamic damping term and $T_\theta(t)$ is a torque function. Using this equation of motion a transfer function can be created.

$$\Theta(s) = \frac{T_\theta(s)}{J_\theta s^2 + (C_\theta + C_A)s + K_\theta} \tag{53}$$

Using a numerical solver it is possible to compute the equivalent aerodynamic damping (C_A) and rotational inertia (J_θ). The transfer functions for all three axes are given in the equations below where $\Phi(s)$,$\Theta(s)$,

and $\Psi(s)$ are all transfer functions describing the flapping, twist (pitch) and lead lag modes. Using these equations the controls designer can choose any stiffness and damping values to achieve the desired flexible natural frequency and damping.

$$\begin{aligned}\Phi(s) &= \frac{T_\phi(s)}{0.2249s^2+(C_\phi+3.909)s+K_\phi} \\ \Theta(s) &= \frac{T_\theta(s)}{0.257s^2+(C_\theta+0.544)s+K_\theta} \\ \Psi(s) &= \frac{T_\psi(s)}{0.4228s^2+(C_\psi+0.121)s+K_\psi}\end{aligned} \tag{54}$$

4 Meta Aircraft Wing Tip Connection Dynamics

The following section explores the connection flight dynamics for meta aircraft where the vehicles are connected wing tip to wing tip using passive magnets with a particular focus on modeling the connection event between aircraft in a practical environment. This section presents a two stage air vehicle connection control law driven by conventional 6 degree of freedom aircraft feedback plus relative position feedback of the lead aircraft.

4.1 Connection Control Law

The overall connection control scheme uses the leader-follower approach. The leader aircraft is instructed to fly a straight and level path ignoring the state of the follower aircraft completely. The control scheme described below details the follower aircraft control architecture to achieve proper connection. The connection control law is split into two stages. Stage 1 is a global mass center to mass center controller that brings the follower aircraft close to the leader aircraft using GPS sensor data. This aspect of the control law fits a 3-degree polynomial between the two aircraft to generate a command trajectory for the follower aircraft. The follower aircraft then follows this trajectory to the leader aircraft[36]. Stage 2 is a wing tip to wing tip controller where the follower aircraft wing tip seeks to track the wing tip of the leader aircraft using a vision based navigation sensor[18]. To blend the two stages together, sigmoidal functions are used to weight the two different control stages so that control laws are blended seamlessly and the transition between both stages is smooth. Figure 40 shows a detailed schematic of the control architecture. It was noticed in initial testing that in the presence of winds repeated contact can occur that may result in a connection failure. To protect the vehicles from repeated contact an imaginary boundary is placed around the leader aircraft wing. If the wing tip of the follower aircraft penetrates this imaginary boundary the follower aircraft is commanded to track a waypoint offset from the leader aircraft wing tip. Once this point is tracked, the follower aircraft then tries to dock once again. This extra logic has been added to increase the robustness of connection.

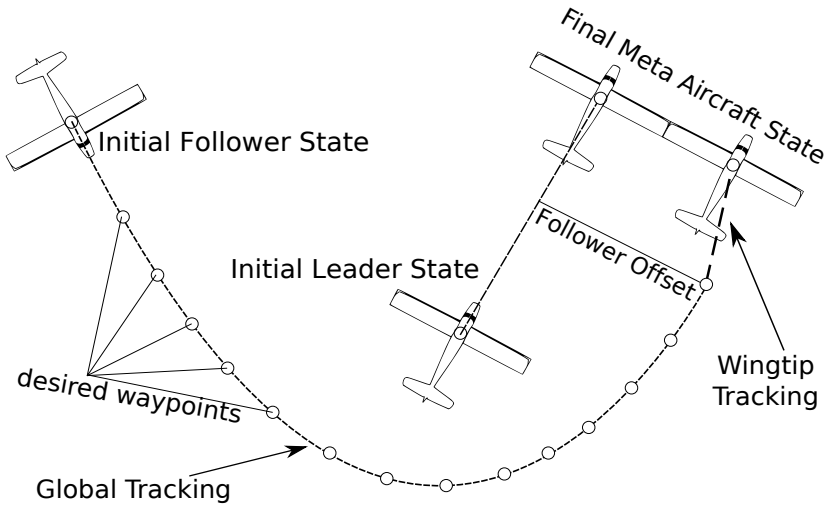

Figure 40: Control Law Stages

4.1.1 Global Tracking Controller

Waypoints are computed using a 3-degree polynomial from the follower aircraft to the leader aircraft. This function is simply parameterized using the parameter s:

$$\begin{aligned} x_w(s) &= c_0 + c_1 s + c_2 s^2 + c_3 s^3 \\ y_w(s) &= d_0 + d_1 s + d_2 s^2 + d_3 s^3 \\ z_w(s) &= e_0 + e_1 s + e_2 s^2 + e_3 s^3 \\ \vec{W}(s) &= x_w(s)\hat{I}_I + y_w(s)\hat{J}_I + z_w(s)\hat{K}_I \end{aligned} \tag{55}$$

The parameter s is allowed to vary from 0 to 1. These equations above have 12 unknowns, thus 12 constraint equations are needed. The first constraint requires $\vec{W}$ to be equal to the follower aircraft state when $s = 0$. Furthermore, when $s = 1$ the waypoint is equal to the current leader aircraft state plus an offset along the $\hat{J}_P$ axis. This offset if used to add a buffer between the follower and leader aircraft and can be seen in Figure 40. Similar constraints are imposed on velocity yielding the following 12 constraint equations which can be

solved for explicitly.

$$\begin{aligned} \vec{W}(0) &= \vec{r}_{I\to F} \quad \vec{W}(1) = \vec{r}_{I\to L} \\ \frac{dW}{ds}(0) &= \vec{V}_{F/I} \quad \frac{dW}{ds}(1) = \vec{V}_{L/I} \end{aligned} \tag{56}$$

Once the polynomial is computed, the follower aircraft tracks a point along the line that is an arclength η along the polynomial. The control surfaces are defined such that δ_{t_i} tracks range, ϕ_c tracks heading, and θ_c tracks altitude using a simple inner loop-outer loop PID controller. The desired heading is computed using the following relationship:

$$\psi_w(s) = tan^{-1}\left(\frac{dy_w/ds}{dx_w/ds}\right) \tag{57}$$

The rudder, elevator and aileron commands are set to $\delta_{r_i} = -K_v v_i$, $\delta_{e_i} = K_p(\theta_i - \theta_c) + K_d\dot{\theta}_i$ and $\delta_a = K_p(\phi - \phi_c) + K_d\dot{\phi}$. A saturation block is added to ensure that a command outside the limits of the control surfaces is not sent to the servos. The Euler angle commands ϕ_c and θ_c are set using the following relationships:

$$\begin{aligned} \phi_c &= K_p(\psi_i - \psi_w(\eta)) + K_d\dot{\psi}_i \\ \theta_c &= K_p(z_i - z_w(\eta)) + K_d\dot{z}_i + K_I\int z_i - z_w(\eta)dt \end{aligned} \tag{58}$$

The control scheme defined above is a conventional inner loop-outer loop control of a fixed wing aircraft using a PID tracking controller. Note that by construction this formulation is only collision free if the initial conditions of the system are set such that the follower aircraft is behind the leader aircraft. No simulations were performed where the follower aircraft initializes ahead of the leader. In this situation a collision could arise however this idea of collision is not investigated in detail.

4.1.2 Wing Tip Error Controller

The wing tip error controller is responsible for driving the distance between the two wing tips to zero. In the global tracking controller, a PID controller is sufficient to move the aircraft close enough for the visual based sensor to take over. A trade study was run using PID, sliding mode, feedback linearization and Model Predictive Control (MPC). It was found that MPC has better connection performance than PID for wing tip error tracking. The Model Predictive Control law assumes that the system is a linear discrete time-invariant

system as shown below.

$$\begin{aligned} \vec{x}(k+1) &= A\vec{x}(k) + B\vec{u}(k) \\ \vec{y}(k) &= C\vec{x}(k) \end{aligned} \tag{59}$$

The nonlinear model depicted in equations (1)-(6) is linearized and then discretized to be put in the above form. The A,B, and C matrices in equation (59) describe the state space system that are used to generate control given a vector of commands $\vec{Y}_C$. The basic formulation starts with propagating the system forward H_p discrete steps. Writing each step in matrix form yields a system of the form

$$\vec{Y} = K_{CA}\vec{x}(0) + K_{CAB}\vec{U} \tag{60}$$

where

$$K_{CA} = \begin{bmatrix} CA \\ CA^2 \\ \vdots \\ CA^{H_p-1} \end{bmatrix}$$

$$K_{CAB} = \begin{bmatrix} CB & 0 & 0 & \dots & 0 \\ CAB & CB & 0 & \dots & 0 \\ CA^2 & CAB & CB & \dots & 0 \\ \vdots & \vdots & \vdots & \ddots & \vdots \\ CA^{H_p-1}B & \dots & CA^2B & CAB & CB \end{bmatrix} \tag{61}$$

and

$$\vec{Y} = \begin{bmatrix} \vec{y}(k) \\ \vec{y}(k+1) \\ \vdots \\ \vec{y}(k+H_p) \end{bmatrix} \quad \vec{U} = \begin{bmatrix} \vec{u}(k) \\ \vec{u}(k+1) \\ \vdots \\ \vec{u}(k+H_p) \end{bmatrix} \tag{62}$$

At this point a cost function can be defined using the equation below

$$J = \frac{1}{2}(\vec{Y} - \vec{Y}_C)^T Q(\vec{Y} - \vec{Y}_C) + \frac{1}{2}\vec{U}^T R\vec{U} \tag{63}$$

where Q and R are weighting matrices. To obtain the optimal control, the cost function is differentiated with respect to $\vec{U}$, set to zero and solved for $\vec{U}$.

$$\vec{U} = K(\vec{Y}_C - K_{CA}\vec{x}(0)) \tag{64}$$

where

$$K = (K_{CAB}^T Q K_{CAB} + R)^{-1} K_{CAB}^T Q \tag{65}$$

In this formulation, $\vec{Y}_c$ is a vector of future commands. To generate future commands, a set of waypoints are defined along the trajectory using the same arclength η from the global tracking controller.

$$\begin{gathered} x_s = x + \eta cos(\Delta\psi) \qquad y_s = y + \eta sin(\Delta\psi) \qquad z_s = z_{WP} - z_{WC} \\ x_c(k+1) = x + \sigma(x_s - x) \quad y_c(k+1) = y + \sigma(y_s - y) \quad z_c(k+1) = z_s \end{gathered} \tag{66}$$

where $\sigma = k/H_p$. k is an integer from 0 to H_p where H_p is the number of discrete steps in MPC. The computation of $\Delta\psi$ involves mapping the offset in crossrange to the yaw angle.

$$\Delta\psi = \psi_F - (K_p\Delta y + K_d\Delta\dot{y} + K_I \int \Delta y \; dt) \tag{67}$$

The values K_P, K_D and K_I are PID gains mapping crossrange to the yaw angle. These values are obtained experimentally. The value of Δy and $\Delta\dot{y}$ switches between two different values as given by the equation below.

$$\begin{aligned} \Delta y &= W_{offset}\Delta y_{offset} + W_{connect}\Delta y_{connect} \\ \Delta\dot{y} &= W_{offset}\Delta\dot{y}_{offset} + W_{connect}\Delta\dot{y}_{connect} \end{aligned} \tag{68}$$

As the subscript implies, the values Δy_{offset} and $\Delta y_{connect}$ are scalar distances between a connection signal and a signal that will move the follower aircraft to an offset value as given by the equation below.

$$\begin{aligned} \Delta y_{connect} &= y_{L,wingtip} - y_{F,wingtip} \\ \Delta \dot{y}_{connect} &= v_L - v_F \\ \Delta y_{offset} &= y_{path} - y_{F,wingtip} \\ \Delta \dot{y}_{offset} &= v_{path} - v_F \end{aligned} \tag{69}$$

The value y_{path} is the y coordinate of a path offset from the leader aircraft where Δw is a constant value set by the control designer. The value v_{path} is the difference between the y-velocity of the follower aircraft and the offset point.

$$y_{path} = y_L - y_F + \Delta w \tag{70}$$

Note these equations assume that the leader is flying straight and level with a heading angle of zero. These equations can be rotated to any heading angle assuming a standard rotation about ψ_L. The values W_{offset} and $W_{connect}$ are sigmoidal functions that can take a value between 0 and 1.

$$W_{offset} = 1 - W_{connect} \tag{71}$$

Clearly when $W_{connect}$ equals 1, the follower aircraft will begin its connection maneuver. If W_{offset} is 1, the follower aircraft will halt its connection maneuver and begin to track the offset point from the leader aircraft. This smooth switching was added into the controller to reduce the number of crashes and failed connection attempts. The argument for the sigmoidal functions is the orthogonal distance along the x and z axes such that $\Delta d = \sqrt{(z_{L,wingtip} - z_{F,wingtip})^2 + (x_{L,wingtip} - x_{F,wingtip})^2}$. Figure 41 shows the value of $W_{connect}$ as a function of Δd. Note that by construction, Δd is always positive.

The effect of this blending creates a schedule for the follower aircraft. The follower aircraft will track the offset point until $W_{connect}$ reaches a value of 1. Once $W_{connect}$ reaches 1 the follower aircraft will begin its

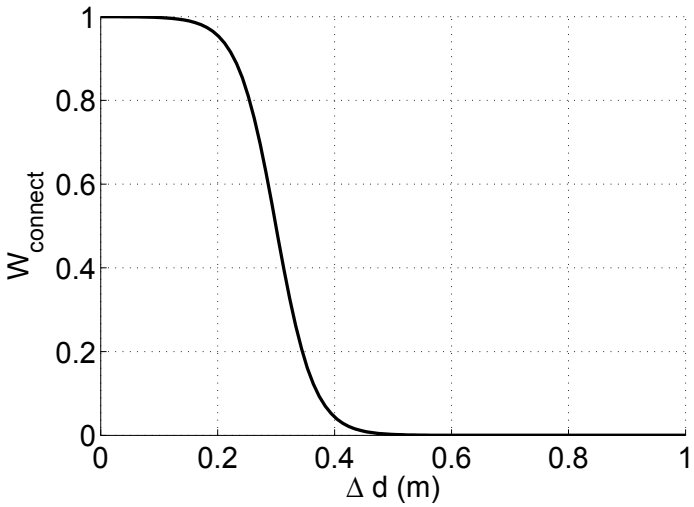

Figure 41: $W_{connect}$ **vs.** Δd **(m)**

connection maneuver. If however, $W_{connect}$ drops below 1, $W_{connect}$ is set to zero, W_{offset} is set to 1 and the follower aircraft will break away from its connection maneuver and begin to track the offset point to avoid the potential for a crash. This can be visualized in the Figure 42.

Here, an imaginary boundary is plotted around the leader aircraft. If the follower aircraft wingtip is inside this boundary, the value of $W_{connect}$ will be 1 and the follower aircraft will attempt to connect. At any point in the connection event if the follower aircraft wing tip falls outside of this boundary the follower aircraft will halt its connection maneuver and track the offset waypoint. Finally, the values of x_c, y_c, z_c are mapped to Euler angle commands.

$$\begin{aligned} \theta_c(k+1) &= tan^{-1}(\tfrac{z_c(k+1)-z_c(k)}{d(k+1)-d(k)}) \\ \psi_c(k+1) &= tan^{-1}(\tfrac{y_c(k+1)-y_c(k)}{x_c(k+1)-x_c(k)}) \\ \phi_c(k+1) &= K_p(\psi - \psi_c(k+1)) \end{aligned} \tag{72}$$

where

$$d(k+1) = \sqrt{(x_c(k+1)-x)^2 + (y_c(k+1)-y)^2 + (z_c(k+1))^2} \tag{73}$$

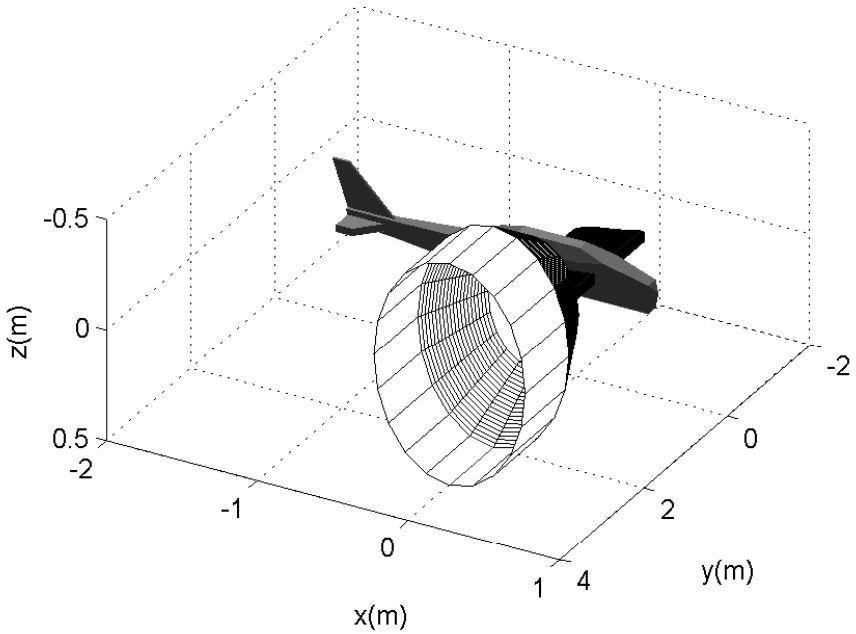

Figure 42: Safety Boundary Placed Around Leader Aircraft Wing tip

Then the Euler angle commands are mapped into roll and pitch rate commands

$$\begin{aligned} p_c(k+1) &= (\phi_c(k+1) - \phi_c(k))/\Delta t_d \\ q_c(k+1) &= (\theta_c(k+1) - \theta_c(k))/\Delta t_d \\ u_c(k+1) &= K_p(u_c - u) \end{aligned} \tag{74}$$

where Δt_d is the timestep used to discretize the linear model. Note that the velocity command is simply a function of the velocity command from the outer loop PID controller. Finally, the three commands can be placed into $\vec{y}_c(k)$ to solve for $\vec{u}(k)$ where $\vec{y}_c(k) = [u_c(k), p_c(k), q_c(k)]^T$ and $\vec{u}(k) = [\delta_e(k), \delta_a(k), \delta_t(k)]^T$.

4.2 Simulation Results

The aircraft used in the following simulations is detailed in Section 2.7. To connect aircraft together, a single magnet is placed at the wing tip of each aircraft with the magnetization direction pointing along the $\hat{J}_B$ axis. The magnet with the highest connection performance is found to be a rectangular magnet with

a maximum force of $1000N$. This magnet is $101.6 \times 25.0 \times 20.2$ mm and weighs approximately $300g$. To accurately represent the aircraft connection surface to model contact between aircraft, the connection surface contains 34 vertices. The contact properties have been set to provide realistic contact response; therefore, every spring constant has been set to 10000 N/m and each damping constant has been set to 40 Ns/m. For the non-linear magnetic discretization, each magnet is split into 27 small elements to compute the magnetic forces and moments.

The aircraft in these simulations are fit with a GPS sensor to obtain x, y, z position data. An accelerometer and rate gyro are used to obtain accelerations and angular velocities. The accelerometer data is integrated to obtain both velocity and position and is blended with GPS data to obtain nearly continuous data. The wing tip controller uses the position information of the leader aircraft using a vision based navigation sensor. This sensor uses 4 or more LEDs to track the relative position and attitude between the two aircraft and has mainly been used for autonomous aerial refueling missions[18]. In this setup, 4 LEDs are mounted on the wing tip which fire at set rates. The follower aircraft contains the sensor to obtain position and orientation information. A schematic of the leader aircraft wing tip complete with the magnet and LEDs is shown in Figure 43.

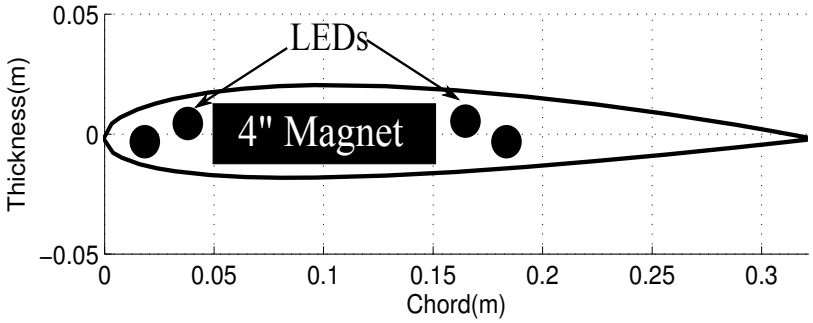

Figure 43: Leader Airfoil Cross Section Detailing Magnet and LED Location

When the follower aircraft uses the wing tip controller, it solely uses the information from the vision sensor and ignores the GPS/IMU data. Sensor noise is modeled to represent feedback from a GPS based system with a position bias of $2.4m$ and a standard deviation of $1.5m$. The accuracy of the vision sensor is a

function of the distance between the image point and the sensor. When the sensor is $10m$ away the position information has a standard deviation of $1cm$. When the sensor is $1m$ away the position information has a standard deviation of $1mm$[18].

An example connection simulation is shown below with perfect sensor measurements and no atmospheric winds. The leader aircraft is initially located at $(0, 0, -200)m$ while the follower aircraft is positioned 50 meters directly behind the leader aircraft. Both aircraft have a forward velocity of 20 m/s. Figure 44 shows a top view of the entire trajectory. Figures 45 - 49 show the position and attitude of each aircraft during this example scenario. The shift from the global tracking controller to the wing tip controller occurs around 40 seconds and connection occurs around 50 seconds. Figures 50 and 51 show wing tip error vs time. During the first 35 seconds the follower aircraft is moving along the global trajectory to the offset waypoint and also moves inline with the leader aircraft. At 40 seconds the x wing tip error is roughly zero and the y wing tip error is roughly 2 times the wingspan of the leader aircraft. At this point the follower aircraft switches to the wing tip controller and the Y wing tip error begins to drop until they finally connect. Once the aircraft connect the control system is turned off entirely. Thus, transient from the connection maneuver causes the aircraft to move laterally after connection. Chapter 5 details a potential controller than can be used once aircraft are connected.

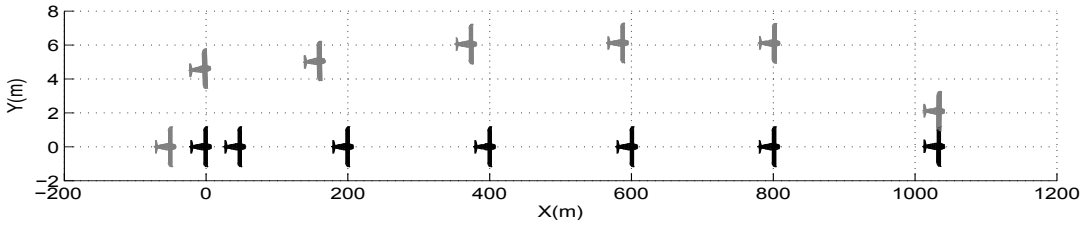

Figure 44: Top down view of Simple Connection Event-Black(leader),Grey(follower)

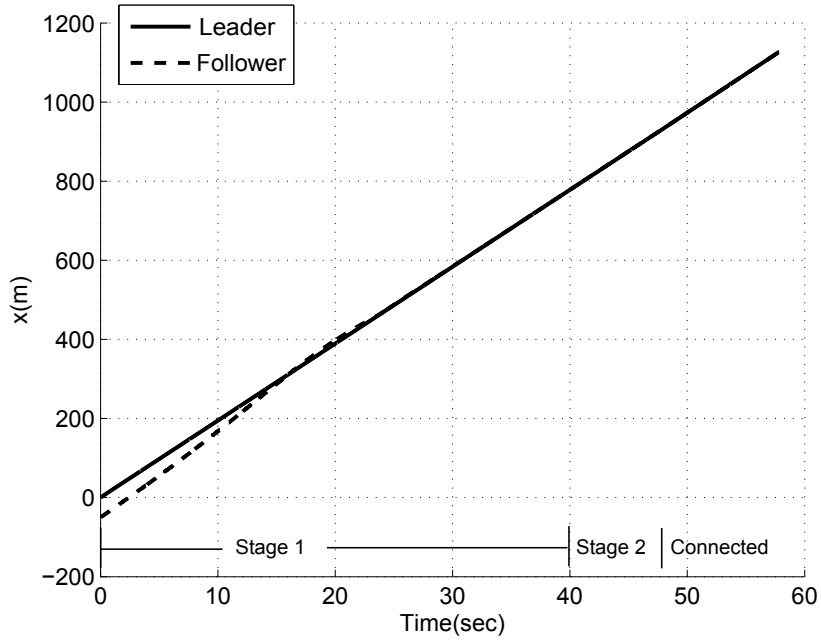

Figure 45: X(m) vs Time(sec)-Solid(leader),Dashed(follower)

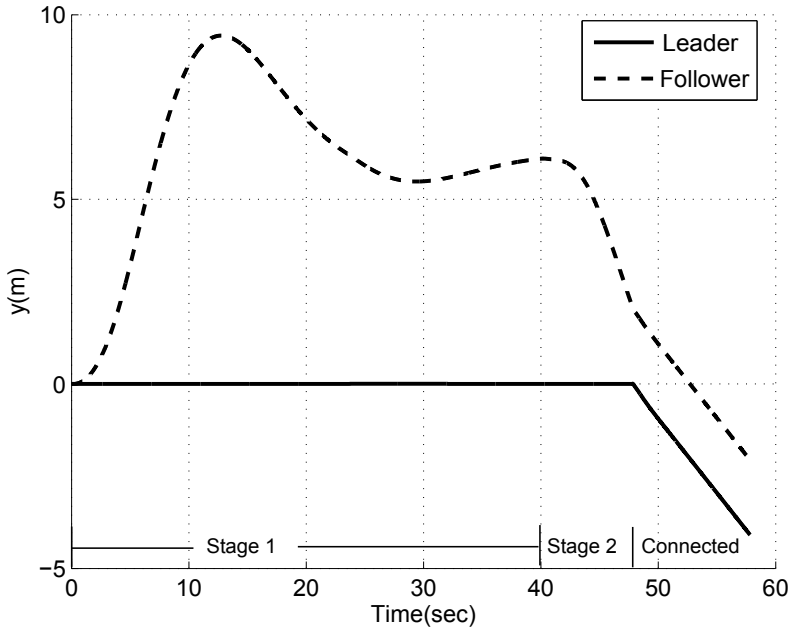

Figure 46: Y(m) vs Time(sec)-Solid(leader),Dashed(follower)

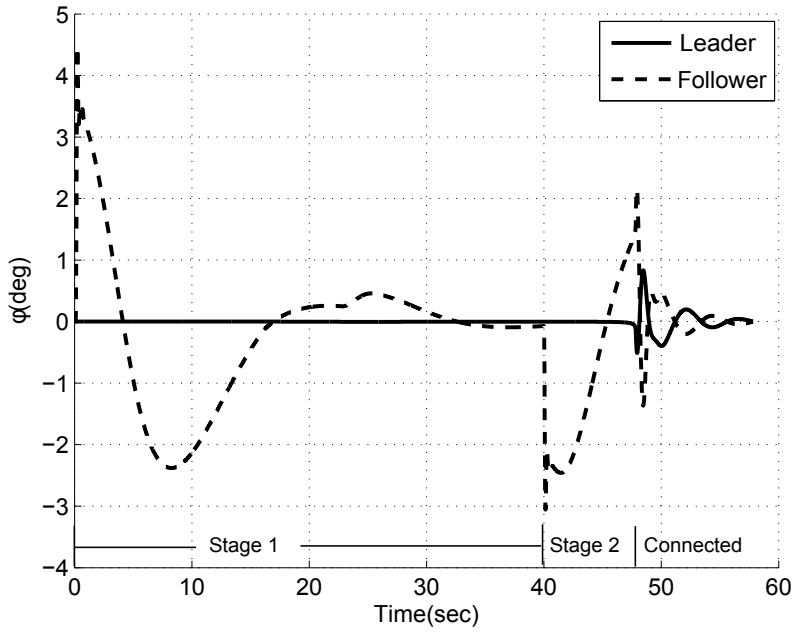

Figure 47: ϕ**(deg) vs Time(sec)-Solid(leader),Dashed(follower)**

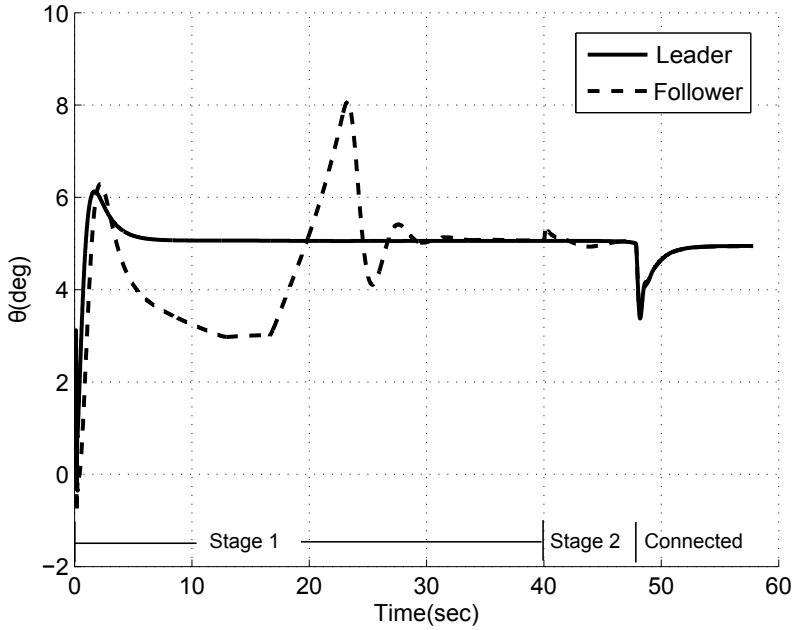

Figure 48: θ**(deg) vs Time(sec)-Solid(leader),Dashed(follower)**

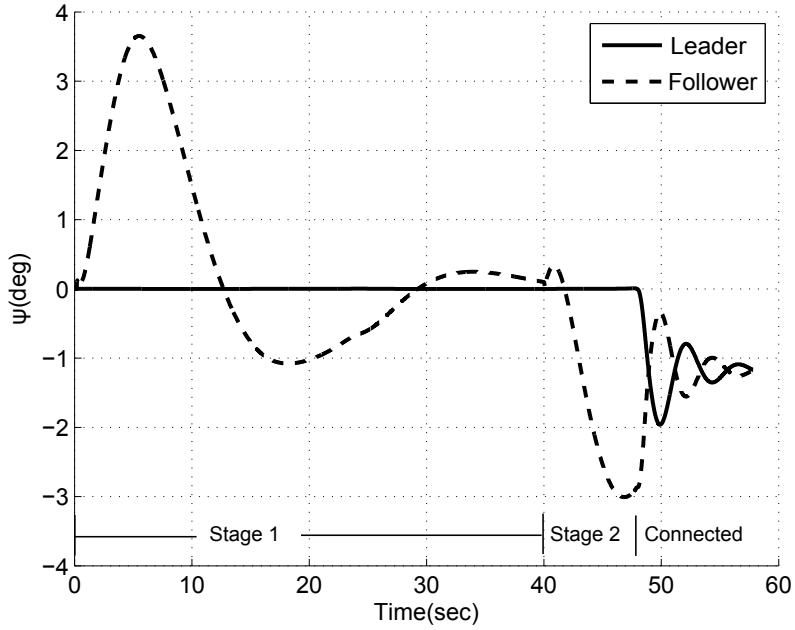

Figure 49: ψ**(deg) vs Time(sec)-Solid(leader),Dashed(follower)**

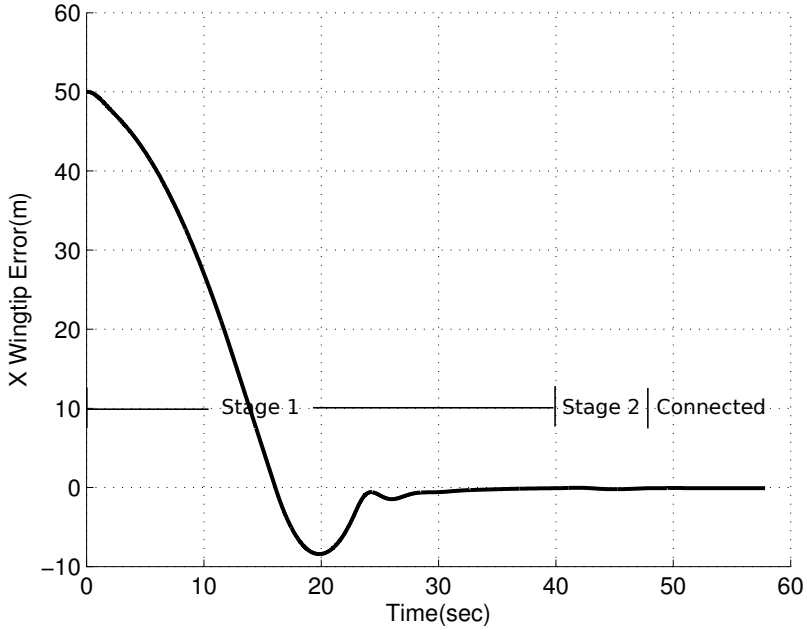

Figure 50: X Wing Tip Error(m) vs Time(sec)

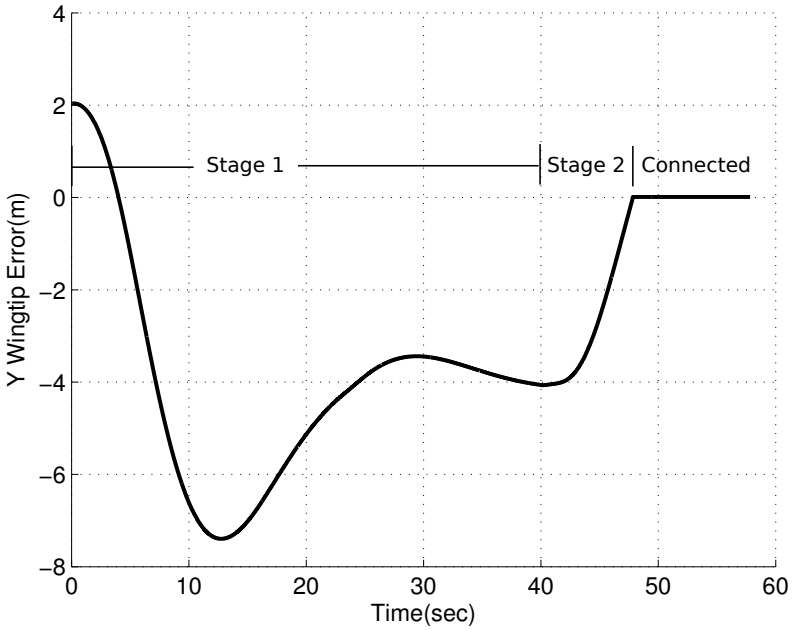

Figure 51: Y Wing Tip Error(m) vs Time(sec)

When atmospheric wind disturbances excite both aircraft, a simple connection like the example above is not achieved. The following example has the exact same initial conditions only 1.5 m/s winds are present using the WRF+Dryden wind model as explained in Section 2.6. The WRF scale and turbulence intensity are set to 0.3. Figure 52 shows the top view of the trajectory of the leader and follower aircraft in these atmospheric winds. At a range of about 1000 m the aircraft contact each other but do not connect. In this example, the follower aircraft is commanded to an offset waypoint and then commanded to try again. This is an example of the extra logic added to inhibit repeated contact. Figure 53 shows a multiple axis plot showing the Y wing tip error in centimeters using the axis on the left and side contact force in Newtons using the axis on the right. A collision occurs around 50 seconds and another around 55 seconds. These collisions give rise to a small contact force as indicated by the spikes of about 100 N. Finally, at about 80 seconds the follower aircraft returns and achieves a successful connection. At this time there is a spike in the contact force that jumps to about 1300 N and then settles around 1000 N to counteract the large magnetic force. Figure 54 shows the magnetic force as a function of time. At 50 seconds there is a very small magnetic force

being generated on the order of $1N$ which cannot be seen. This is due to the non-linearity of the magnets. The magnets do not produce a large force until the magnets are very close to one another on the order of $10cm$. At 50 seconds although the Y wing tip error is zero, the X wing tip error is about $0.1m$ thus contact forces arise but only small magnetic forces are generated. Finally, at 80 seconds the plot indicates a large magnetic force indicating a connection between the two aircraft.

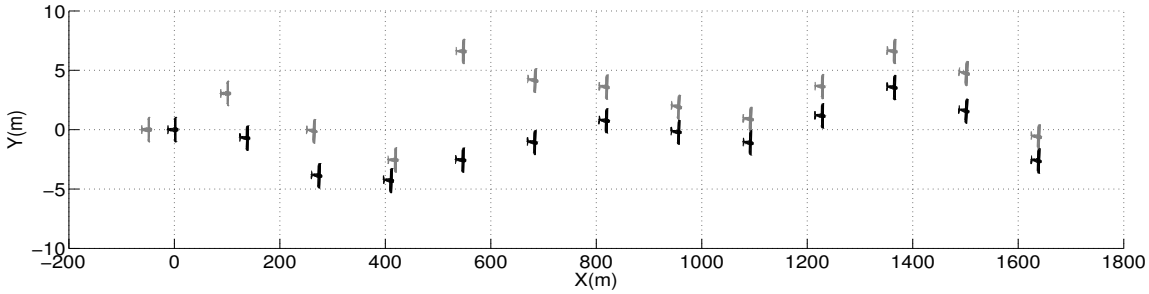

Figure 52: Top down View of Connection Event in 1.5 m/s Winds(WRF=0.3,TURB=0.3)

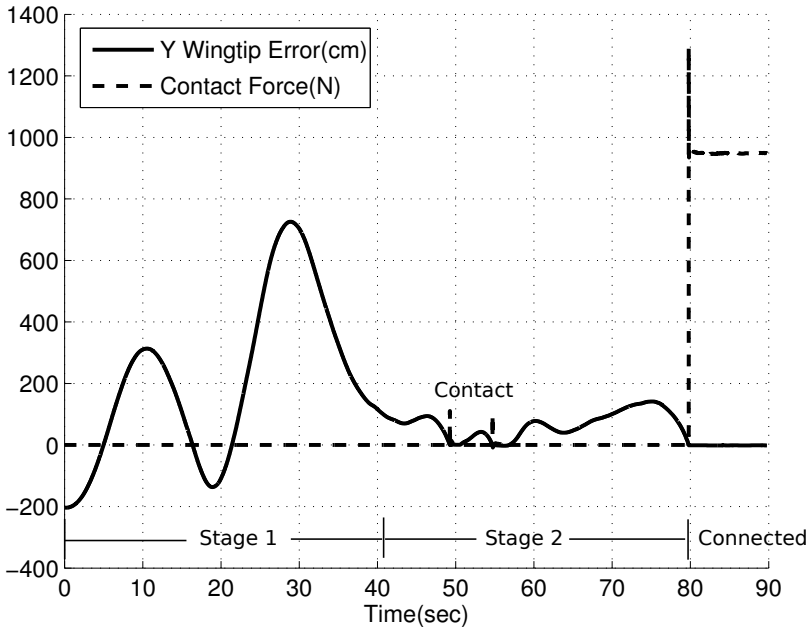

Figure 53: Y Wing Tip Error (cm),(solid) ; Side Contact Force (N),(dashed) vs Time(sec)

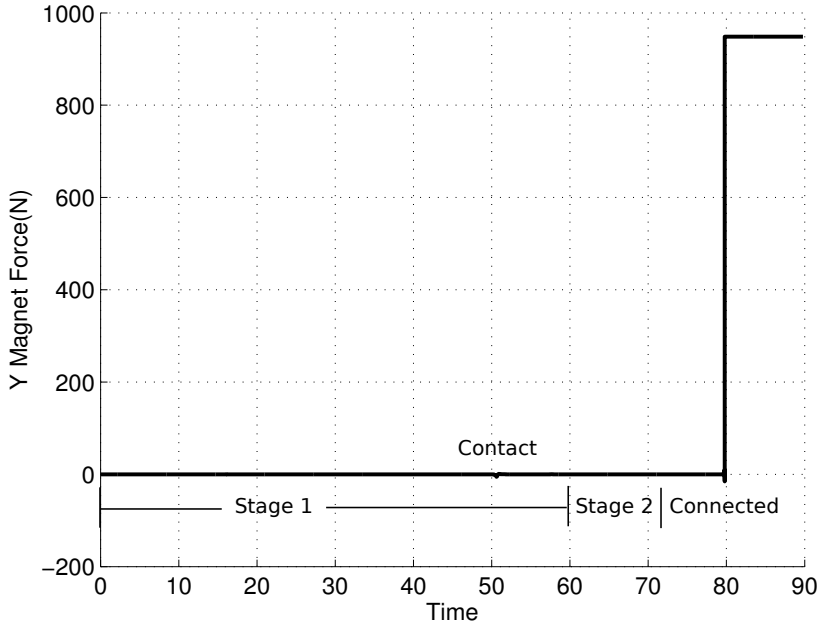

Figure 54: Magnetic Force(N) vs Time(sec) - Forces Expressed in Follower Body Frame

4.3 Parametric Trade Studies

To enable reliable vehicle connection in a practical environment, a variety of parametric trade studies are performed. The metric used to analyze performance is percent connection rate. Monte Carlo runs are performed at a given wind speed and the percentage of runs with a successful connection is reported. A run is deemed successful if the aircraft achieves a successful connection in 10 minutes or less. Unless stated specifically, the wind environment used is imported into the simulation such that when the mean wind of the WRF model is $4m/s$, the Dryden turbulence has a standard deviation of $0.25m/s$. Thus when the WRF mean wind is increased to $8m/s$ the Dryden turbulence will have a standard deviation of $0.5m/s$. The WRF wind is increased until percent connection rate drops to zero percent and is plotted with maximum wind disturbance on the x-axis. To ensure that the parameters chosen for the aerodynamic and magnetic models are sufficiently detailed to accurately capture percent connection rates, the modeling parameters were varied. The magnet elements were varied from 27 to 343 elements and the number of main wing elements were varied

from 3 to 7. Figure 55 shows the result of increasing the number of elements on the main wing from 3 to 7. Figure 56 shows the result of increasing the number of elements on the magnet model from 27 to 343 for a square magnet. The number of elements on the main wing and magnet has little effect on percent connection rates. Thus, for the rest of the Monte Carlo runs the number of elements on the main wing is set to 3 and the number of elements on the magnet is set to 27.

Note that these figures are generated using discrete Monte Carlo runs for windspeeds where the scale factor on the WRF and turbulence models is increased by 0.25. All lines collapse to zero percent when the scale factor is 2.25 corresponding to a mean windspeed of about 10.9 m/s. Although, when the scale factor is 2.0, the percent connection rates are non-zero. If the resolution was finer, say increments of 0.1 or 0.05 the data would show the percent connection rates falling at different windspeeds. Thus, the lines are slightly different throughout the trade study but collapse to zero at the same windspeed.

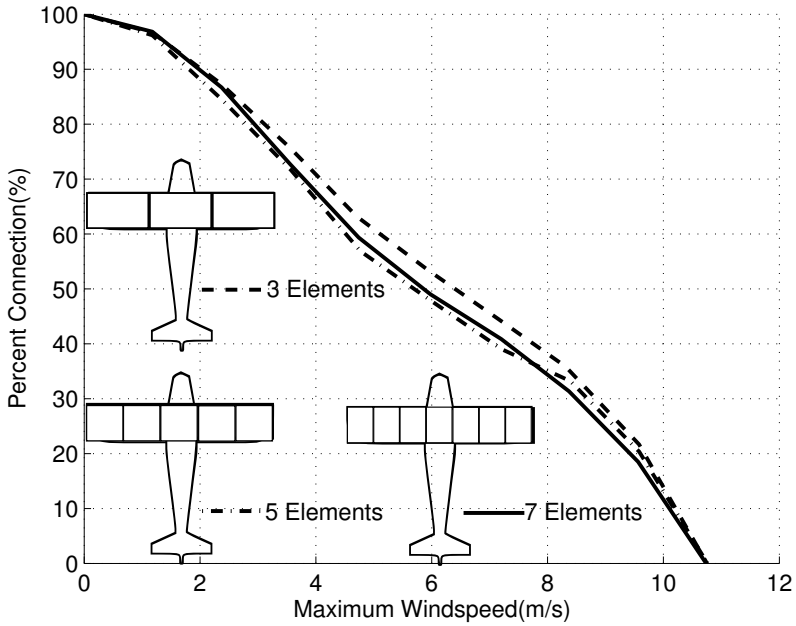

Figure 55: Percent Connection(%) vs. Maximum Wind Speed(m/s) - Main Wing Elements

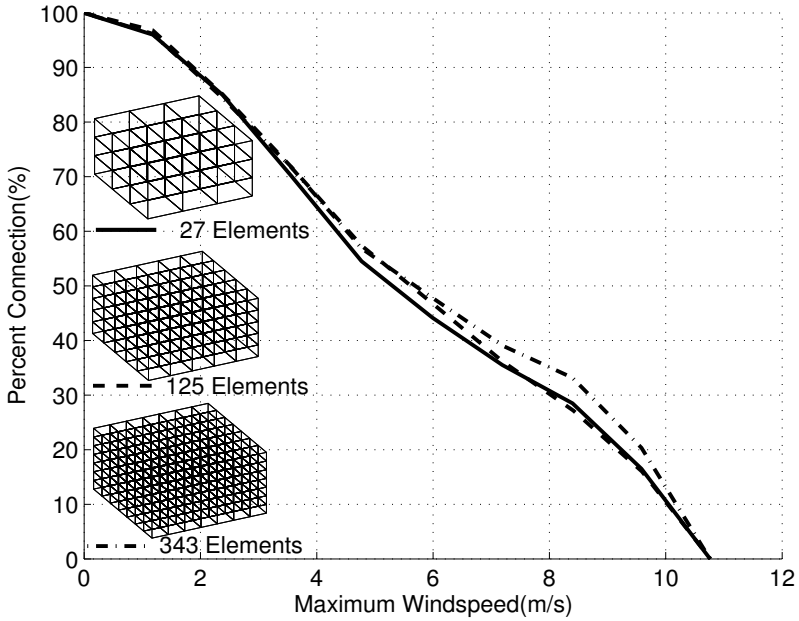

Figure 56: Percent Connection(%) vs. Maximum Wind Speed(m/s) - Magnet Elements

Atmospheric winds play an important role in connection performance. With no winds the connection performance is 100% even with realistic sensor noise which shows that the controller is robust to sensor errors. Unfortunately, as winds are increased the percent connection rate begins to drop until it drops to zero. This is a consequence of the decline in controller performance where tracking performance between the leader and follower aircraft is the main driver. The leader aircraft in these connection simulations is instructed to fly steady and level throughout the flight and it is not important how much the leader aircraft is disturbed. The main parameter that must be minimized is the tracking error between the leader and follower aircraft. Connection is achieved when the tracking error is less than the window the connection mechanism allows. There are two main components to increase percent connection rates of this system. One way is to increase the robustness of the controller by decreasing tracking error but another is to alter the connection mechanism, allowing the controller to be more lax. There is a boundary between how well the follower can track the leader aircraft and how close the two aircraft need to be before a connection occurs.

Note that the aircraft are given 10 minutes to connect. In this time, the aircraft can either crash, connect

or simply not connect in the allotted time due to large atmospheric winds. However, detail has only been given to the connection event and a crash is realized when the center of mass of each aircraft is less than half the wingspan of the aircraft. Since the contact points are only placed around the wing, the simulation is not sophisticated enough to capture a crash event. Therefore, the simulation can only predict two outcomes: connection or not. For example, Figure 57 shows the percent connection rates of the nominal configuration plotted alongside the percentages of crashes and percentages of no connections. It is important for the reader to realize that the percent connection rate is merely the percentage of simulations that attained a good connection in 10 minutes. In these 10 minutes, if the center of mass of the two aircraft becomes smaller half the wingspan the simulation is deemed a crash. If in these 10 minutes, the aircraft do not crash and do not connect the simulation is deemed a failure. Notice that the percent failures is non-zero. This means that although the percent connection rate falls to zero it does not imply that the percent crash rate rises to 100%. Furthermore, because the simulation is not sophisticated enough to model a crash, the percent of crashes is an overestimate. It may be in a real flight test that the aircraft could actually recover from a trajectory where the distances between their center of masses is less than half the wingspan.

4.4 Controller Performance in Winds

In order to directly compare the controller performance to tracking error, the aircraft are instructed to fly in formation but not connect with the same atmospheric disturbances as the Monte Carlo runs. At each wind level the heading angle is randomized for 200 headings and the average error in x,y,z is reported for all headings. This is to average out any bias toward wind direction. Figure 58 shows that as the atmospheric wind intensity is increased the tracking error in position increases considerably. The tracking error is computed as $e = \sqrt{(x - x_c)^2 + (y - y_c)^2 + (z - z_c)^2}$.

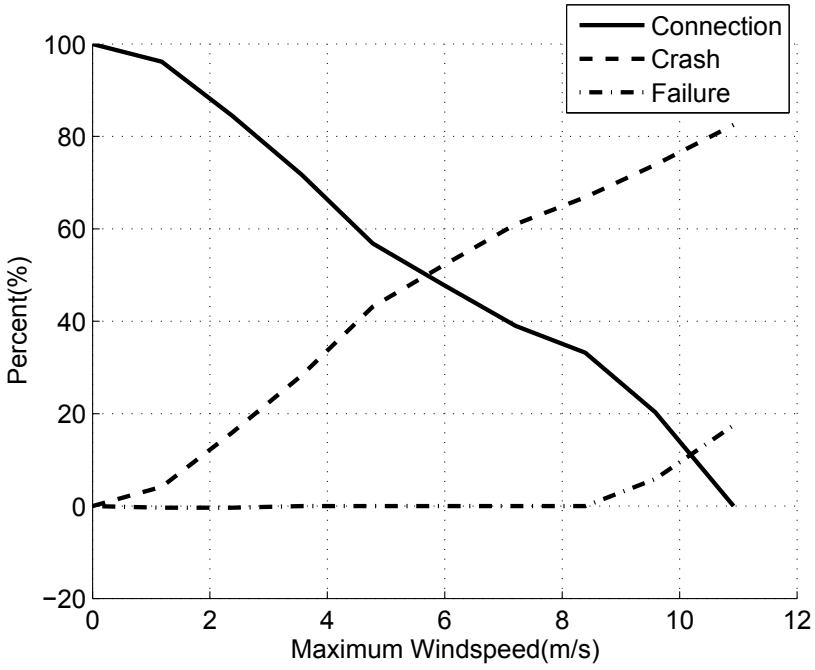

Figure 57: Percent Connection(%) vs. Maximum Wind Speed(m/s) - Explanation of Percent Connection

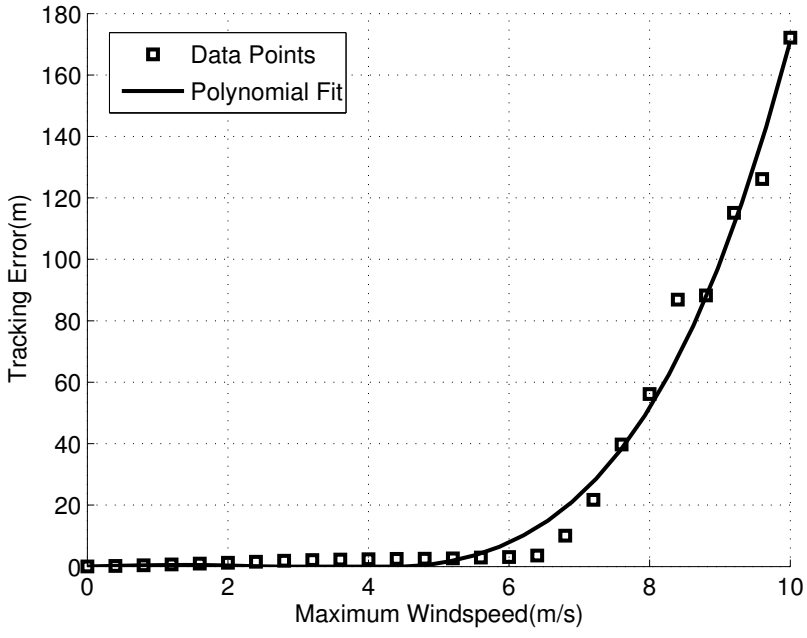

Figure 58: Tracking Error(m) vs. Maximum Wind Speed(m/s)

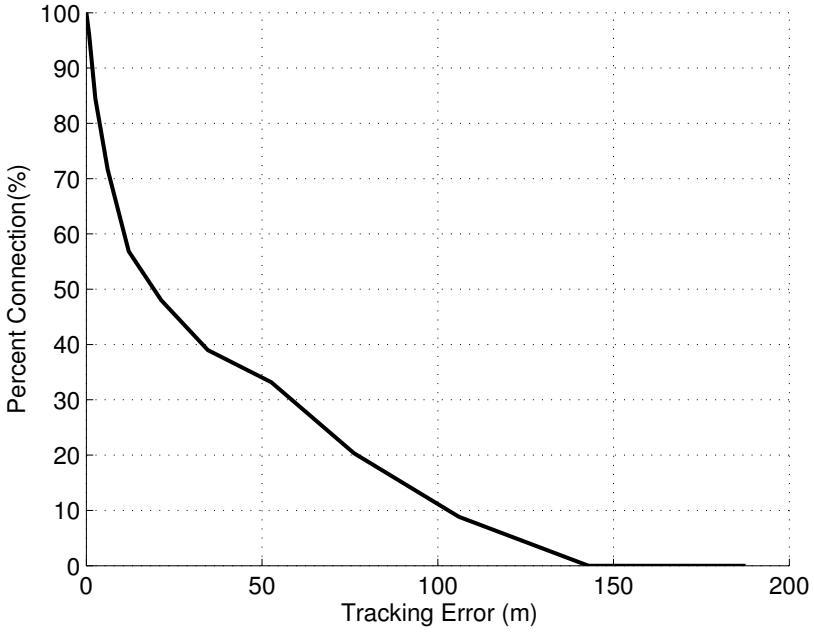

Figure 59: Percent Connection(%) vs. Tracking Error(m)

This drop in tracking performance can be directly related to the drop in connection performance as shown in Figure 59. In order to maintain percent connection rates above 80% the tracking error of the controller must be below about 2.5 m. In order to understand the characteristics of the atmospheric wind field, in particular examining its effect on connection performance, a simple wind model is tested. A simple wind field is a static sinusoidal wave with a spatial frequency. To create a sinusoidal wave, equation (75) is used to relate the x position of each element on each aircraft to the current disturbance with an intensity K_i and frequency f_x. In this study, only 1 spatial frequency is used along the x direction and the aircraft fly with a nominal heading of $\psi = 0$.

$$\begin{Bmatrix} u_d \\ v_d \\ w_d \end{Bmatrix} = \begin{Bmatrix} K_u \\ K_v \\ K_w \end{Bmatrix} cos(f_x x) \tag{75}$$

The frequency is then varied from 0 to 0.1 rad/m and the wind intensity is set at 2 m/s which corresponds to 10% the nominal flight speed. The spatial frequency is in units of rad/m which translates to $20 f_x rad/s$

assuming that the aircraft fly at a nominal speed of 20 m/s. Setting $K_v = K_w = 0, K_u = 2$ creates a change in the axial velocity. The aircraft experiences a headwind followed by a tailwind. In this case, little change is noticed in percent connection rates. Rather, the percent connection rates remain at 100% except for frequencies around 0.075 rad/m where the percent connection rate drops to 92% as shown in Figure 60. Docking is thus robust to disturbances at frequencies between 0 and 0.1 rad/m and a wind intensity of up to 2 m/s along the I_B axis.

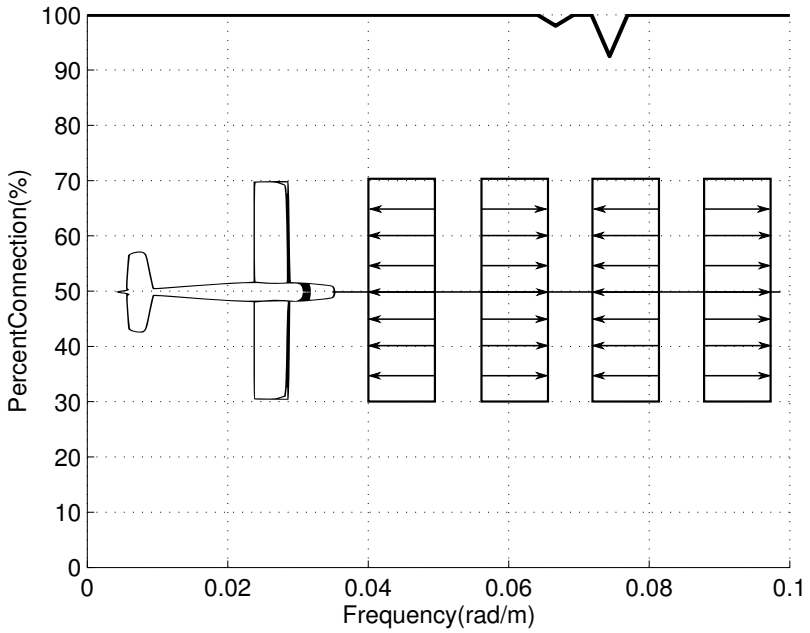

Figure 60: Percent Connection(%) vs. Frequency(rad/m) - Axial Disturbance(K_u = 2m/s)

With $K_u = K_w = 0, K_v = 2$, an increase and decrease in the side velocity of the aircraft is generated. In this case, a drop in percent connection rates at two specific spatial frequencies of 0.02 rad/m and 0.08 rad/m is noted (Figure 61). At frequencies of 0.02 rad/m and 0.08 rad/m or about 0.4 rad/s and 1.6 rad/s, the percent connection rate drops considerably to about 10%. These frequencies corresponds to wavelengths of 50 m and 12.5 m.

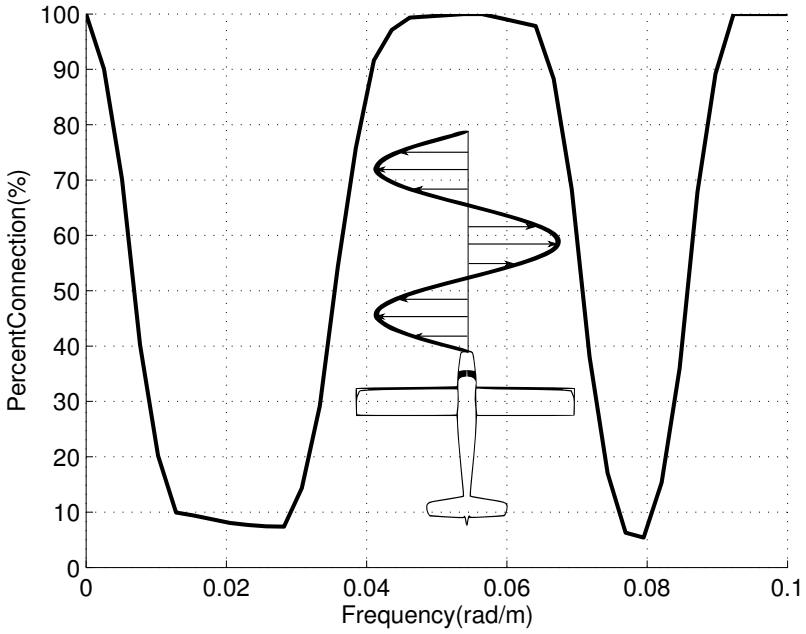

Figure 61: Percent Connection(%) vs. Frequency(rad/m) - Lateral Disturbance(K_v = 2m/s)

The explanation of these buckets relates to the tracking controller defined in Section 4.1.2. Without any sensor errors a nominal simulation would look like Figure 62, provided that $W_{connect}$ was set to zero 0 indefinitely. The leader aircraft would track a crossrange value of zero perfectly and the follower aircraft would track the offset path perfectly.

If however, sensor errors are present, both aircraft would experience some deviations from their path. Figure 63 shows an example simulation where the leader and follower aircraft have sensor errors in their feedback signals. However, the follower aircraft receives feedback from the leader aircraft assuming that it is flying perfectly at a crossrange of zero. That is, the leader aircraft trajectory has no effect on the follower aircraft in this scenario.

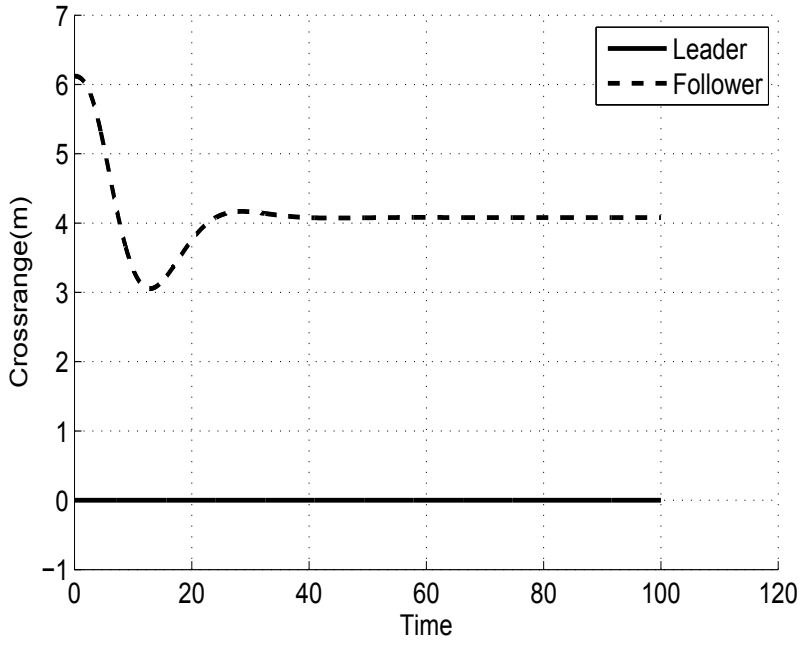

Figure 62: Crossrange(m) vs. Time(sec) for Leader and Follower Aircraft with No Sensor Errors

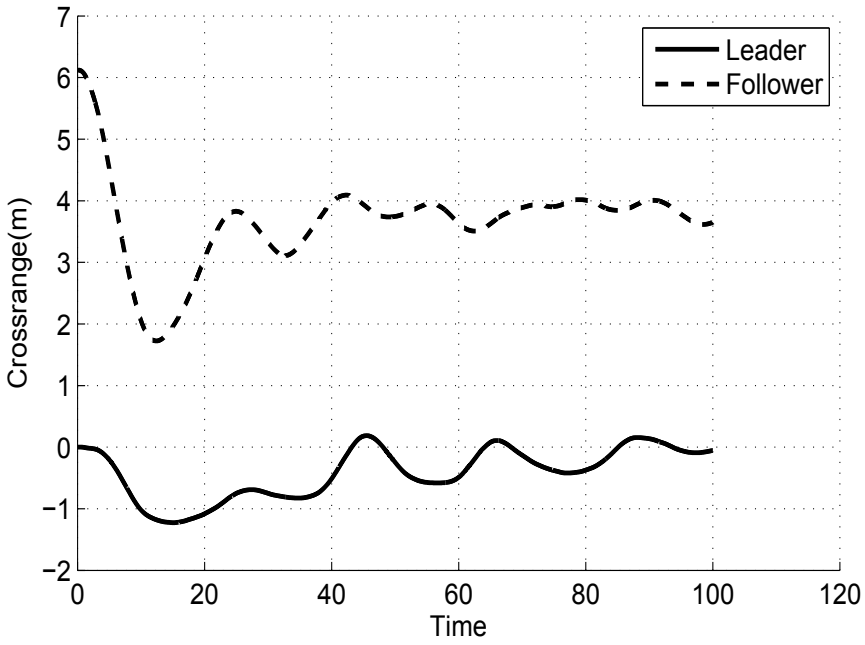

Figure 63: Crossrange(m) vs. Time(sec) for Leader and Follower Aircraft without Tracking Leader Aircraft

The issue arises when the follower aircraft attempts to track the leader aircraft. In this case, the error in the trajectory of the follower aircraft is worsened by the error in the trajectory of the leader aircraft. This is because the follower aircraft uses image point feedback from the leader aircraft. Figure 64 shows how the tracking performance in the follower aircraft is now worse than it was in Figure 63.

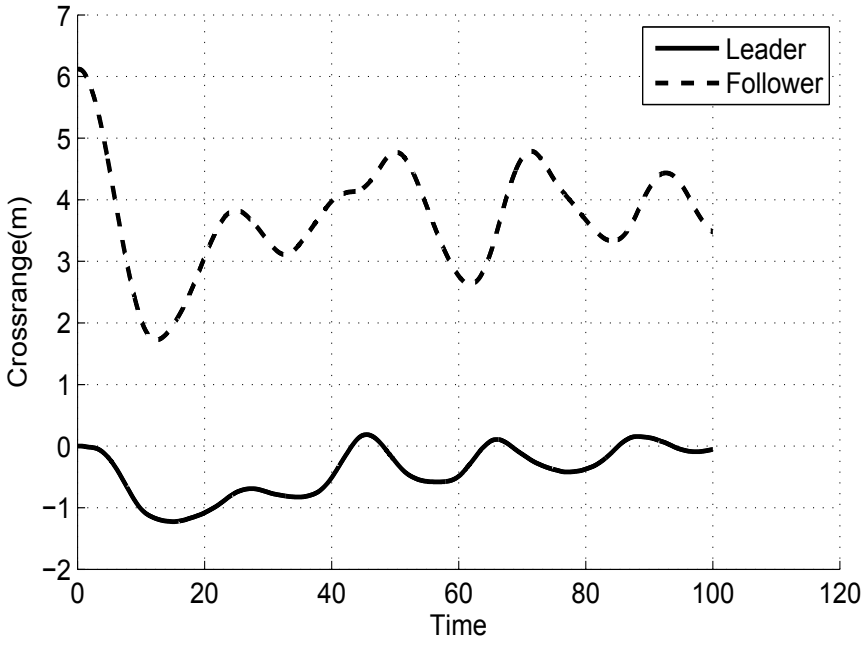

Figure 64: Crossrange(m) vs. Time(sec) for Leader and Follower Aircraft

This drop in tracking performance is what causes the drop in percent connection rates at 0.02 rad/m. In order to highlight this effect, the the aircraft are flown steady and level in the same wind field depicted but do not attempt to connect. The result is a sinusoidal state history in crossrange. The amplitude of the crossrange can be reported for multiple frequencies. The result of this analysis is shown in Figure 65.

This plot indicates that a spatial wind frequency of 0.005 to 0.025 rad/m excites the aircraft in such a way that the tracking performance is reduced and the crossrange response is greater than 20 m. The follower aircraft has a slightly different magnitude response than the leader aircraft when it is not tracking the leader because the follower aircraft is using MPC for control and the leader aircraft is using PID. The biggest issue is when the follower aircraft tries to track the leader aircraft at this frequency. Two effects are happening

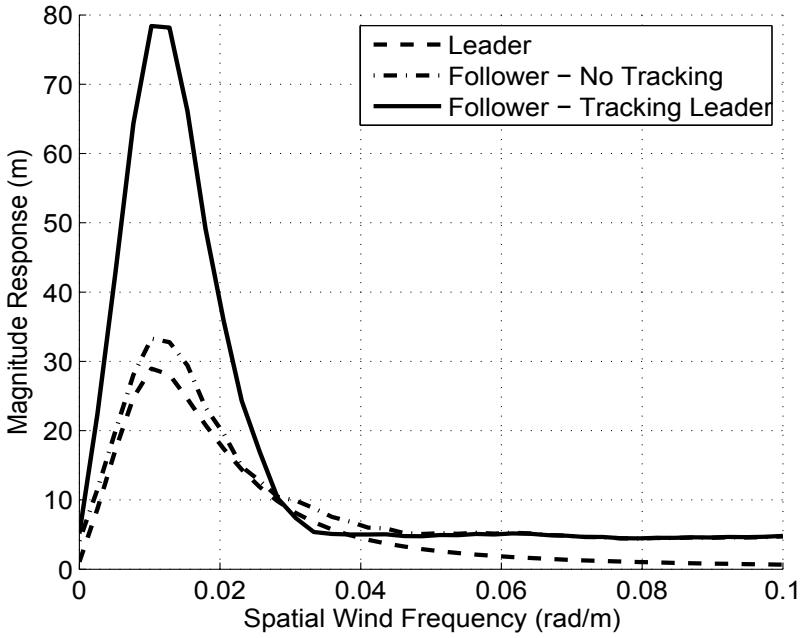

Figure 65: Spatial Wind Frequency (rad/m) vs. Crossrange Response (m)

here. First, the leader and the follower aircraft lose tracking performance at this specific frequency. The follower aircraft then tries to track this sinusoidal trajectory which further worsens the tracking performance. What results, is a specific spatial frequency that the aircraft should not fly in. The second bucket at 0.08 rad/m is purely a consequence of the sigmoidal functions described in Section 4.1.2. A frequency of 0.08 rad/m causes the response in the aircraft to resonate with the logic in moving from tracking the wing tip to tracking the path offset from the leader. Right when the follower aircraft begins its connection maneuver the wing tip moves outside of boundary and it halts its connection maneuver. This limit cycle is repeated for the entire 10 minute simulation and thus the aircraft never connect.

With $K_u = K_v = 0, K_w = 2$, an upwash and then a downwash is experienced by the aircraft. In this case, percent connection rates drop to zero once frequencies above 0.01 rad/m are encountered (Figure 66). The reason for the drop in frequencies above 0.01 rad/m is again due to the safety boundary built around the wing tip. Note, that although percent connection rates drop, the safety boundary reduces the number of crashes.

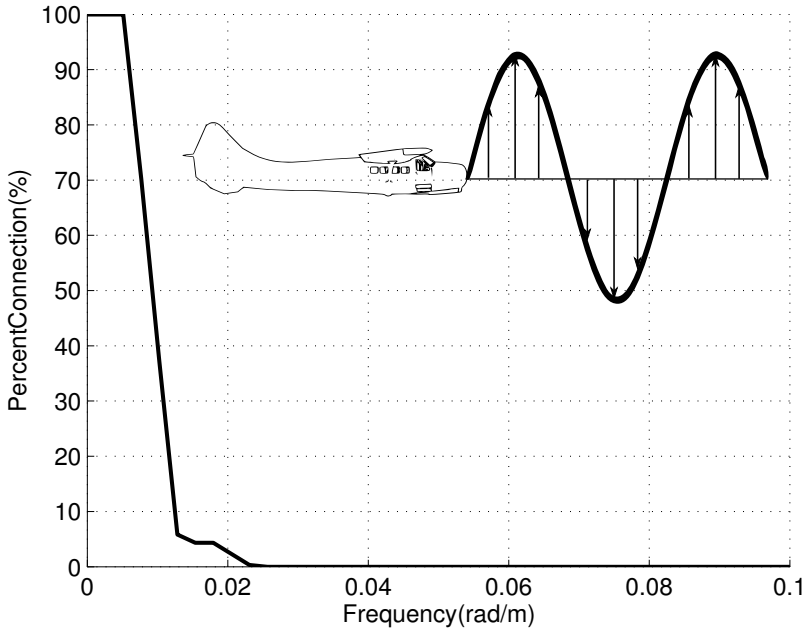

Figure 66: Percent Connection(%) vs. Frequency(rad/m) - Vertical Disturbance(K_w = 2m/s)

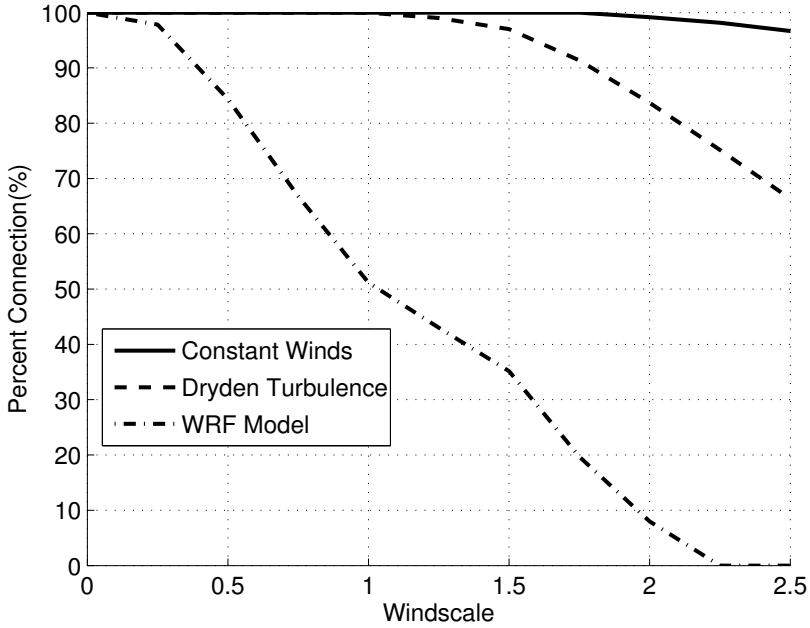

Figure 67: Percent Connection(%) vs. Wind Scale - Wind Model

To understand the effect of different wind types on connection performance, constant winds, pure turbulence (Dryden turbulence), and pure low frequency winds (WRF) are compared (Figure 67). At a wind scale of 1, the constant wind model and WRF model have a mean wind value of 4 m/s whereas the Dryden turbulence model has a mean wind of zero and a standard deviation of 0.25 m/s. High frequency turbulence, at the intensity normally found in the atmosphere, and constant wind gusts are not a significant driver of connection rate performance. Low frequency spatial gusts, particularly in the vertical direction hamper connection rates the most.

Given the results, increasing percent connection rates can be achieved by flying faster. To investigate the effect of speed on percent connection rates a Monte Carlo simulation was run with the Dryden and WRF models set to a scale of 0.8 while varying the nominal speed of the aircraft from 15 to 30 m/s (Figure 68). Flying faster increases connection performance while slower worsens percent connection rates all the way down to about 50%.

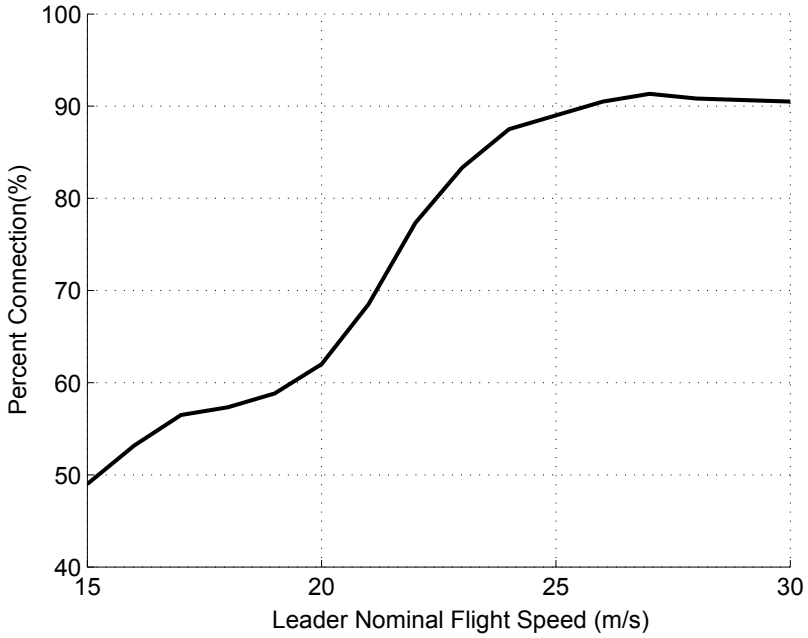

Figure 68: Percent Connection(%) vs. Leader Nominal Flight Speed(m/s)

Note, that the controller designed here has been tuned with good disturbance rejection. It is worth noting

that no work has been done to minimize saturation. That is, if the winds are high enough and the error big enough the controls can saturate. A good figure of merit is the amount of time the controls are saturated during a connection event and averaging this over all windspeeds. A percentage of 100% means the controls are saturated for the entire duration of the flight and 0% implies no saturation during the flight at all. Note however that the saturation limits of the elevator and aileron which directly control the crossrange and altitude have saturation limits of $\pm\ 30^o$. If the saturation percentage is zero the absolute values of the control deflections might still be high but just not saturated. Figure 69 shows the average saturation percentage of the aileron and elevator. The thrust and rudder channels are left out for brevity. This Figure shows that the aileron and elevators saturate more as the windspeed increases as expected however the maximum saturation percentage is only 18% for the elevator and about 2% for the aileron. This indicates that the gains in the controller could easily be increased significantly to increase tracking performance. It is worth noting that a fully actuated aileron or elevator is not problematic at all. The issue with control saturation has to do with the decline in tracking performance due to the limit in controls. Thus, it is clear that tracking performance would decline as windspeed increases since the amount of control saturation increases leading to smaller percent connection rates. Future work may include designing an aircraft that has more control authority to fight winds or at least intelligently fight atmospheric winds.

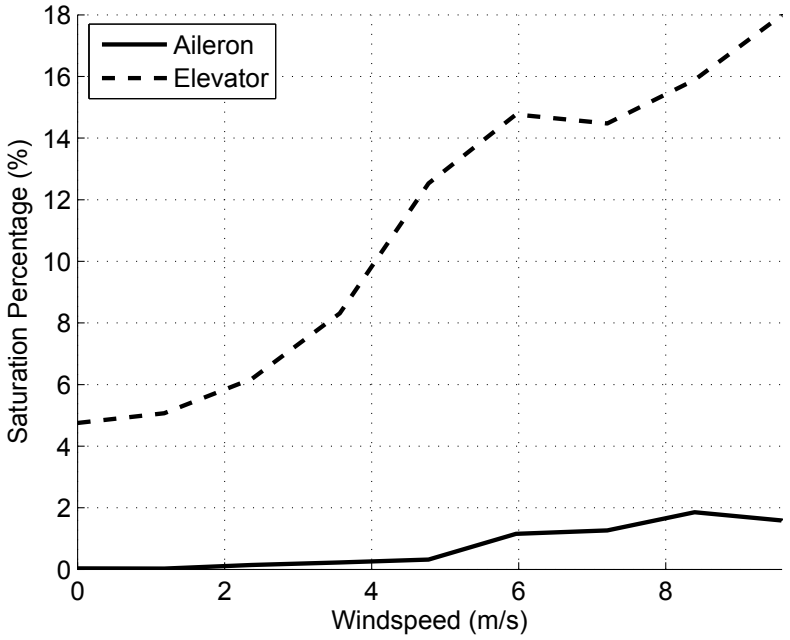

Figure 69: Percent Control Saturation (%) vs. Maximum Wind Speed(m/s)

4.5 Connection Mechanism Design

A complement to the rational of increasing controller performance is to engineer the connection mechanism to be more robust which creates a bigger window for a connection to occur. The magnets placed on the wing tips of the aircraft are the driving force behind a successful connection. The bigger and stronger the magnet, the larger the pull or force field there is that can bring the aircraft together. The boundary between non-negligible and negligible magnetic forces and moments is coined the sphere of influence (SOI). If the control system can successfully guide the wing tip of the follower aircraft to fall within the magnets SOI, the aircraft will connect if there are no atmospheric disturbances. Naturally, the bigger the SOI, the better connection performance. Unfortunately, due to size and weight constraints on the aircraft the choice of a magnet is not simply the biggest or strongest magnet. That is, the magnet must fit inside the aircraft, it must not weight too much and it must maintain a strong connection such that the aircraft do not break apart in winds. The magnets themselves only have a few parameters that can be changed. These include

the charge density (J), the number of magnets, the overall shape, and the overall size. The geometry of the magnet has the biggest effect on connection performance. Figure 70 shows a 4 view of an SOI for a magnet size of $50.8 \times 50.8 \times 21.3mm$ and a charge density of $J = 1.29\ kGauss$. Notice that the SOI is an ellipsoid rather than a cone. If the aircraft are close but slightly offset in either x or z, the aircraft do not connect. This is due to the nature of the magnetic fields produced by cuboidal magnets.

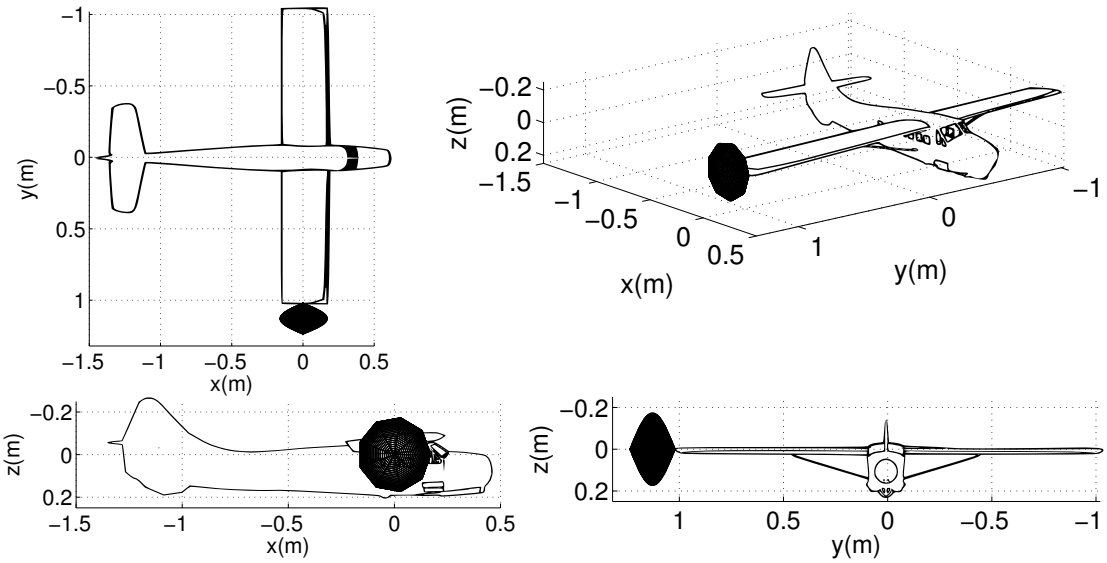

Figure 70: Magnetic Force Field(SOI) 4-View for 2" Square Magnet J=1.29

When magnets are directly aligned, a strong magnetic force is produced bringing them together, but when the magnets are offset there is a repulsive force that pushes the magnets away (Figure 71). Magnets naturally will reorient themselves to align and connect but unfortunately these magnetic moments are not sufficiently strong to rotate the entire aircraft to connect. Another interesting results is that placing two magnets side by side has the exact same force and moment characteristics as a larger magnet with the same size due to the repulsive force exhibited by slightly offset magnets. Increasing the number of magnets or placing magnets side by side creates destructive interference and has the same effect as increasing the size of the magnets.

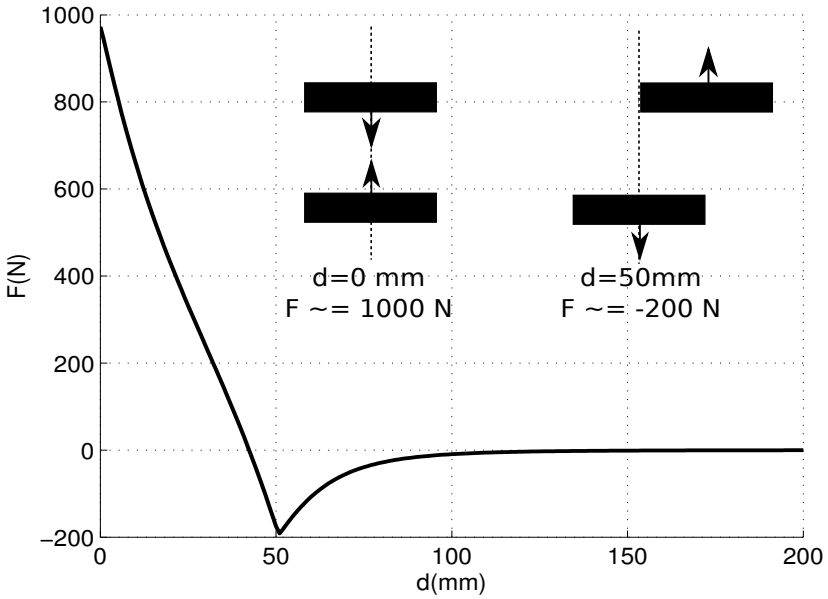

Figure 71: Magnetic Attraction and Repulsion

Increasing the charge density of the magnet has a small effect on connection performance. To show this effect, the charge density of a $50.8 \times 25.4 \times 9.5mm$ magnet is altered from $J = 0.75$ to $J = 2.25$ $kGauss$ while the size of the magnet is held constant. Note, that the force of the magnet is proportional to J^2, thus a charge density of 1.82 is the equivalent to multiplying the force of the magnet with charge density of 1.29 by a factor of 2. A charge density of 0.75 is then a factor of 1/3 and 2.25 is a factor of 3. Figure 72 shows the 3-view of each SOI in the same format as Figure 70 except the aircraft has been removed for easier viewing and Figure 73 shows how each SOI affects connection performance. The larger the charge density the better the connection performance.

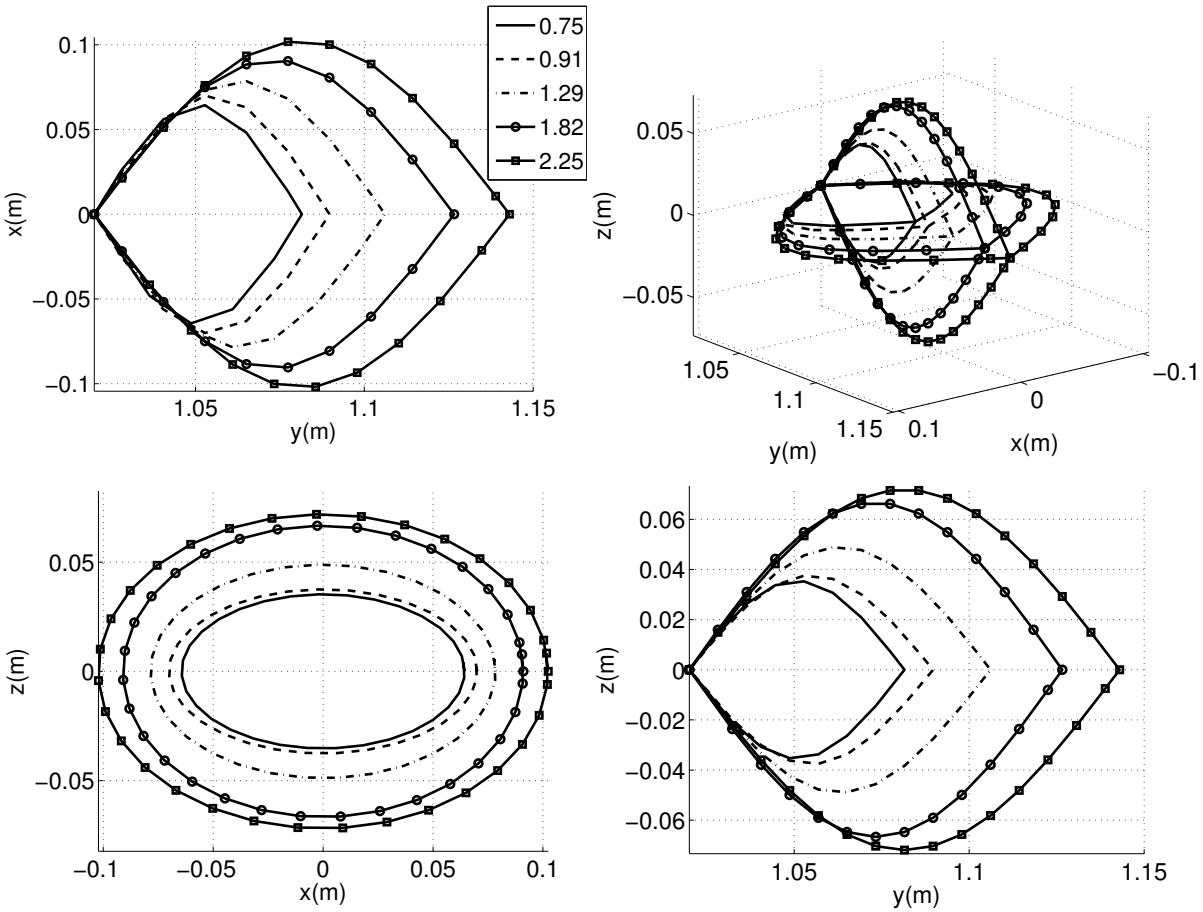

Figure 72: SOI 3-View for Increasing Charge Density

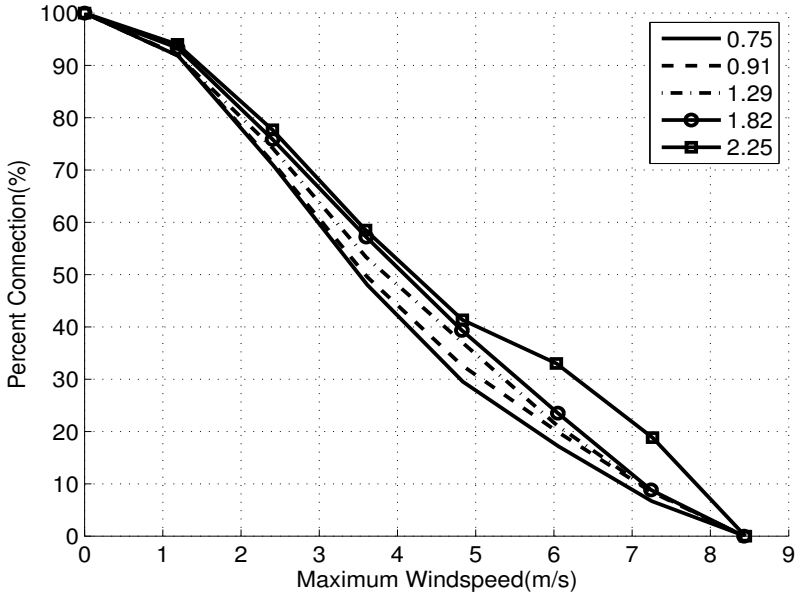

Figure 73: Percent Connection(%) vs. Maximum Wind Speed(m/s) - Charge Density Varied

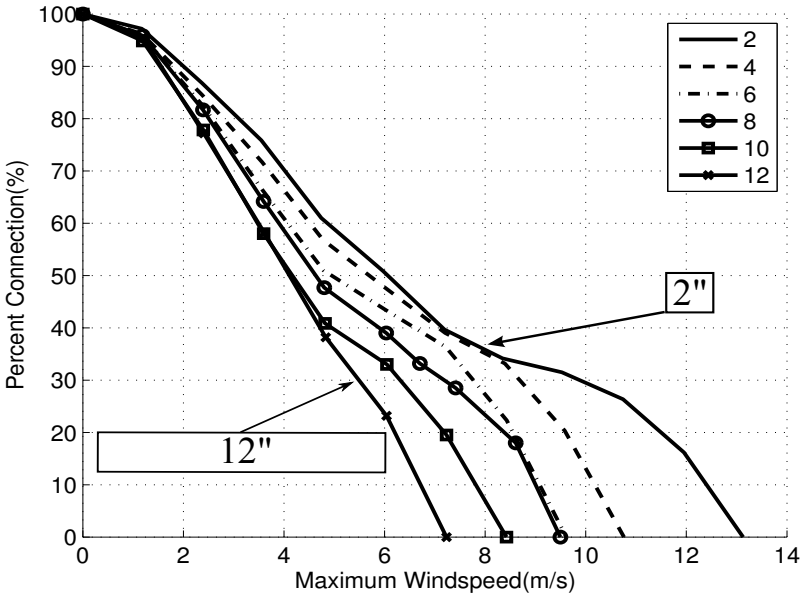

Figure 74: Percent Connection(%) vs. Maximum Wind Speed(m/s) - Magnet Length Varied

The overall shape of a magnet, has a significant effect on connection rate. Since increasing the number of magnets is identical to increasing the size of the magnet, the length of the magnet is varied. Long skinny magnets exhibit an undesirable force distribution; thus, connection performance declines considerably (Figures 74 and 75).

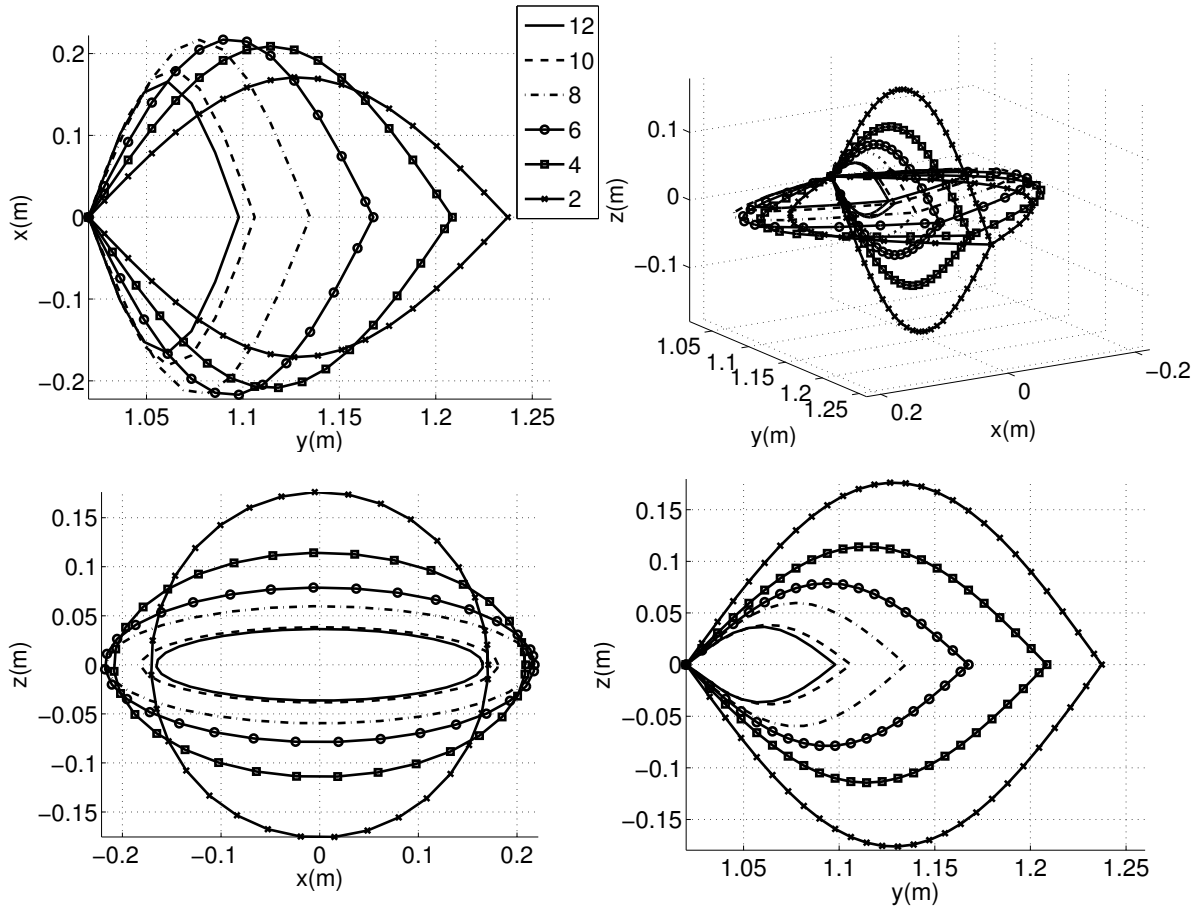

Figure 75: SOI 3-View for Varying Magnet Length from 12" to 2"

The decline in performance can be understood by examining the force distribution of the magnets. Figures 76 and 77 show the F_{XM} and F_{ZM} magnetic forces respectively for a long 12" magnet next to a square 2" magnet both with a maximum force of $1000N$. Although the 12" magnet exhibits a large F_{ZM} force, there is a very small F_{XM} force as opposed to the 2" magnet which has symmetric forces that are large along both axes.

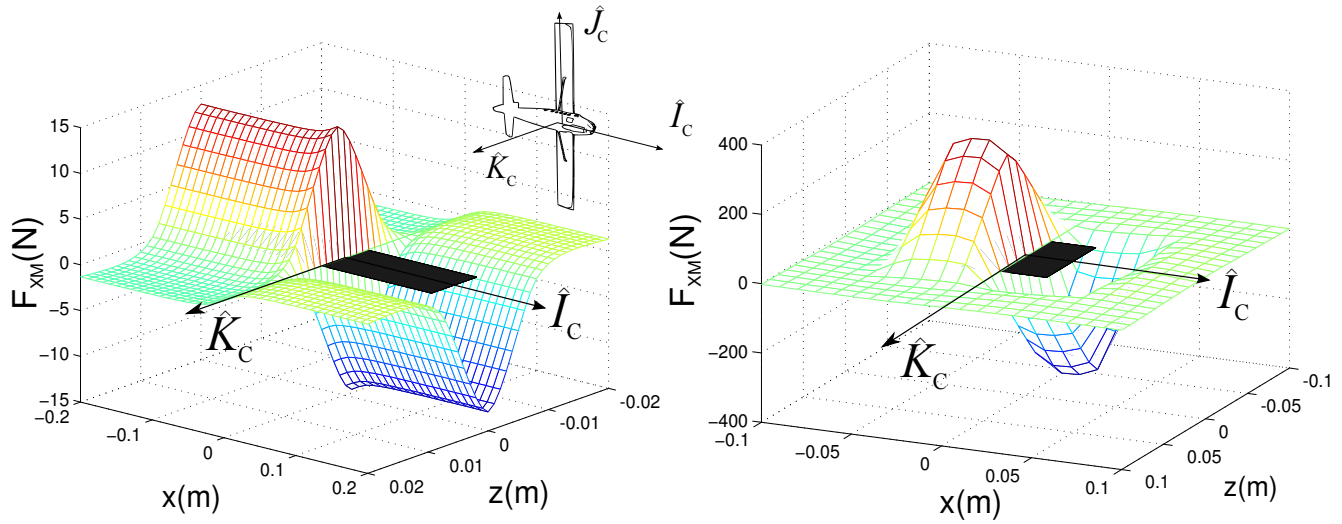

Figure 76: F_{XM} **Force(N) vs. Position of Leader Magnet(m) for a 12" Rectangular Magnet(Left) and 2" Square Magnet(Right)**

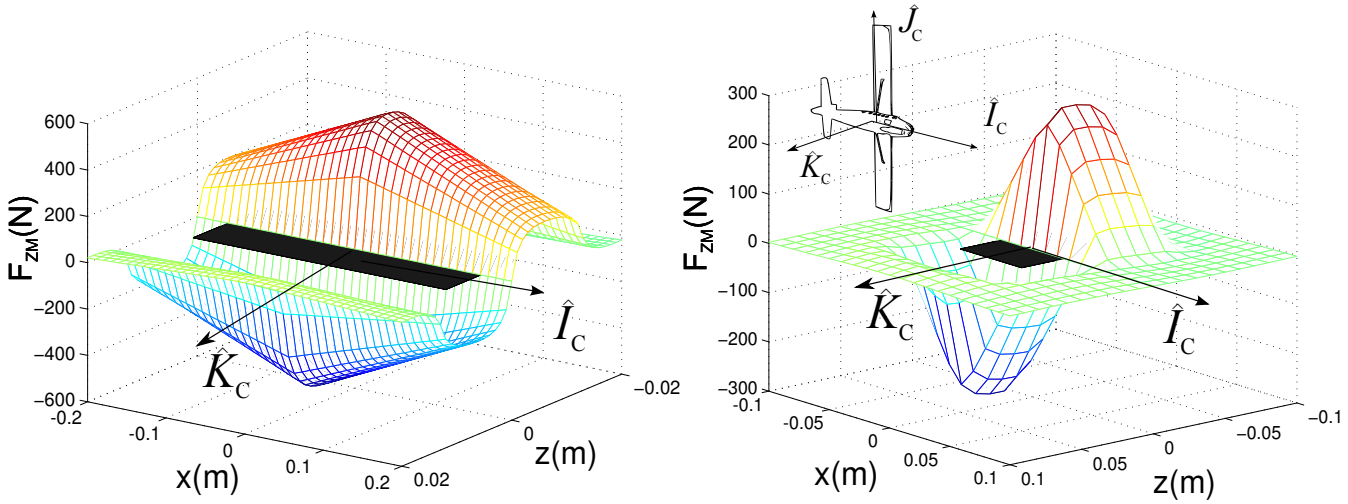

Figure 77: F_{ZM} **Force(N) vs. Position of Leader Magnet(m) for a 12" Rectangular Magnet(Left) and 2" Square Magnet(Right)**

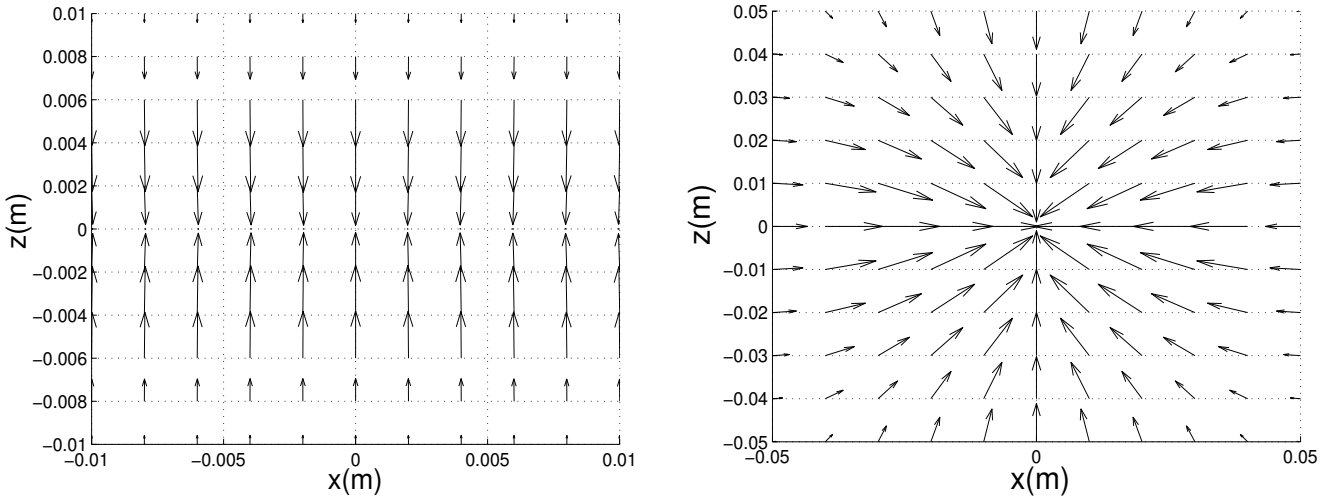

Figure 78: Quiver Plot showing F_{XM} and F_{ZM} Force for a 12" Rectangular Magnet(Left) and 2" Square Magnet(Right)

Figure 78 shows a quiver plot of a 2D cross section detailing the F_{XM} and F_{ZM} force. This Figure further details the difference between the 12" and 2" magnets. Investigation of the connection dynamics indicates that if the error in the wing tips along the x-axis is substantial the rectangular shaped magnets will provide little correction to this error and it will most likely result in a failure. Therefore, although maximum force during connection is important, the force distribution is even more important. Using all of this information it is possible to choose a magnet that exhibits a desirable force distribution while meeting size and weight constraints. The magnet chosen has a maximum force of $1000N$, a size of $101.6 \times 25.0 \times 20.2\ mm$ and weighs approximately $300g$.

Another idea to increase the connection rates and the magnets sphere of influence is to have a spring loaded actuator attached at the wing tip that would fire the magnet towards the other wing when the aircraft were in a desirable window. Increasing the reach of the magnet increases the sphere of influence to a much larger radius and increases connection performance (Figure 79). If the wing tips of the aircraft are aligned ($x_f - x_l << 1\ and\ z_f - z_l << 1$) and less than 1 m away, the actuator fires. In the simulation, the magnet is allowed 3DOFs. The speed of the actuator plays an important part in the system. If the magnet is fired too slowly the magnet will not connect as the aircraft are being perturbed by atmospheric winds. Still, an

actuator capable of firing a $300g$ magnet at $10m/s$ results in roughly a 15% increase in percent connection rates.

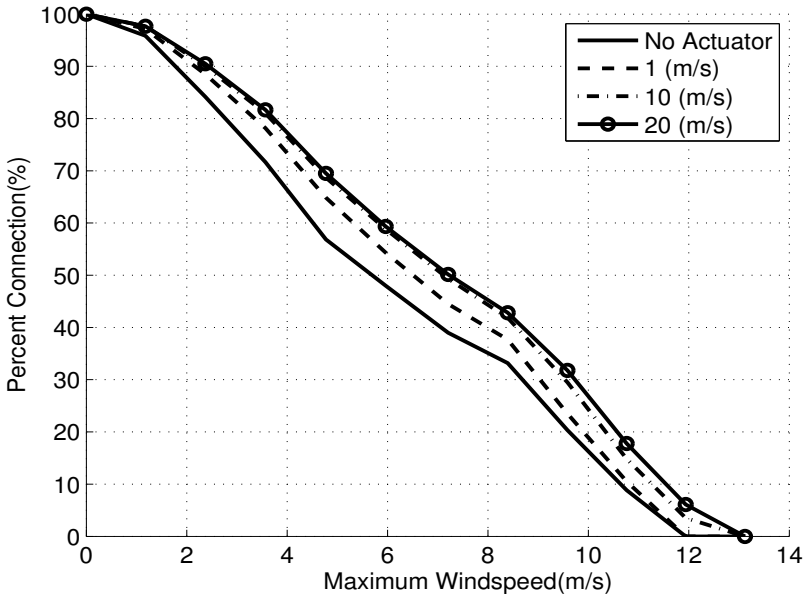

Figure 79: Percent Connection(%) vs. Maximum Wind Speed(m/s) - Magnet Actuator

5 Meta Aircraft Flight Performance

This chapter explores the control of meta aircraft in numerous configurations with a focus on the performance of different types of configurations in a realistic wind environment. A control law is formed that adequately controls meta aircraft in a variety of different configurations by using a simplified rigid body dynamics model that alters inner and outer loop gains that are dependent on the meta aircraft configuration. This control law is capable of adequately controlling meta aircraft and is sufficiently flexible to accommodate different configurations. Using this control architecture the benefits of a meta aircraft from a stability and lift to drag performance perspective are examined.

5.1 Meta Aircraft Control System

To control the meta aircraft in different conditions a simplified rigid body model is used to alter inner and outer loop gains that are dependent on the meta aircraft configuration. A feedback linearization scheme is used in the inner loop and PID is used for the outer loop. Finally, a minimization routine is run to allocate control to individual lifting surfaces on each aircraft. Figure 80 shows the overall flow of the meta aircraft controller. Here outer loop heading and altitude commands are sent to an outer loop PID controller to create inner loop pitch and roll commands. These commands are then translated into pseudo controls using conventional feedback linearization. The pseudo controls are then sent to a rigid body model to cancel out the rigid body dynamics. Finally, a minimization routine is used to allocate controls of all individual control surfaces. All controls are then sent to the plant and the output of each aircraft is measured. The state of each aircraft is sent to the inner loop feedback linearization block while the meta aircraft state, or the average of all aircraft, is sent to the outer loop PID controller. The rigid body model is also used to update inner and outer loop gains depending on the meta aircraft configuration which is sent from the plant.

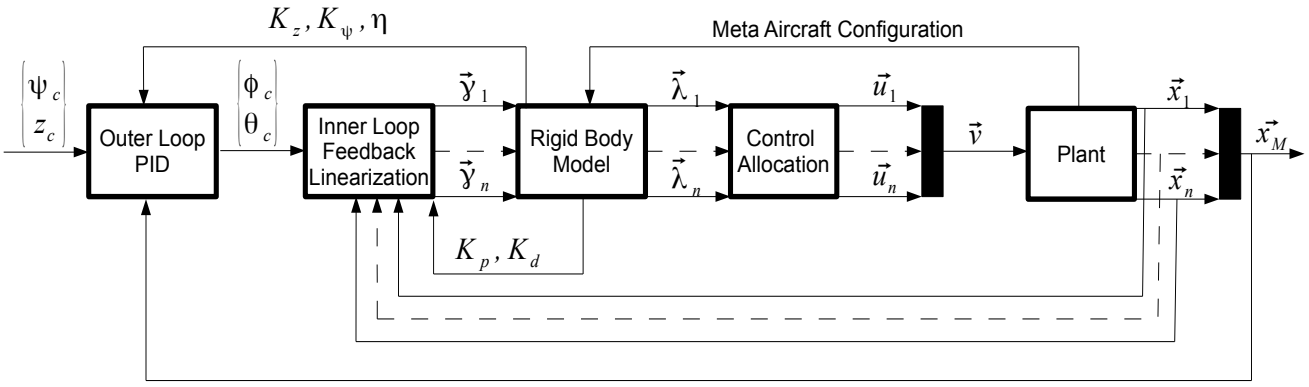

Figure 80: Meta Aircraft Control System

5.1.1 Rigid Body Model

When multiple aircraft are connected, the rigid body modes of the aircraft change. In order to capture these changes, a rigid body model is created. The formulation presented here reduces the $6NDOF$ model to just $6DOF$ by assuming the connection joints are rigid. Thus, the system reduces to a system with 3 translational coordinates (x_M, y_M, z_M) and 3 rotational components $(\phi_M, \theta_M, \psi_M)$. This model can be created on the fly assuming that the configuration of the meta aircraft is known. Figure 81 shows a schematic of an example meta aircraft system.

In this schematic, each aircraft is used to compute a composite center of mass denoted B_M. Forces and moments are then computed at each aerodynamic center to compute the total force and moment about the composite center of mass. In order to simplify the controller derivation, the forces and moments of every aircraft is split into forces and moments that are not a function of control $(\vec{F}_{A0i}, \vec{M}_{AOi})$ and forces and moments that solely include control $(\vec{F}_{A1i}, \vec{M}_{A1i})$. The total mass of the system is simply the sum of all aircraft mass in the system.

$$m_M = \sum_{i=1}^{N} m_i \tag{76}$$

Using the total mass, the center of mass with respect to the inertial frame can be written using the

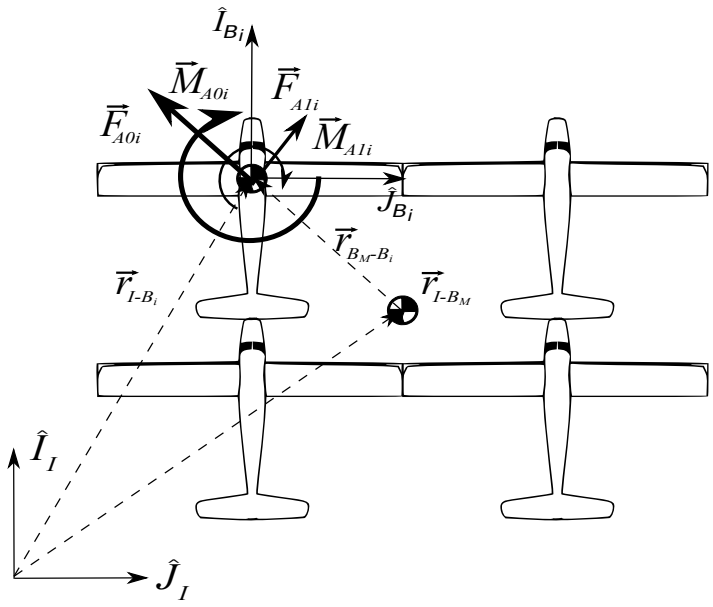

Figure 81: Rigid Body Model

following equation.

$$\vec{r}_{I-B_M} = \frac{1}{m_M} \sum_{i=1}^{N} m_i \vec{r}_{I-B_i} \tag{77}$$

The moment of inertia matrix can then be computed using the parallel axis theorem.

$$I_M = \sum_{i=1}^{N} I_i + m_i S_{B_M}(\vec{r}_{B_i-B_M}) S_{B_M}(\vec{r}_{B_i-B_M})^T \tag{78}$$

The kinematic equations of the meta aircraft are then taken about the composite mass center. These are the same standard equations used in the fully flexible model.

$$\begin{Bmatrix} \dot{x}_M \\ \dot{y}_M \\ \dot{z}_M \end{Bmatrix} = [\mathbf{T}_{IB_M}] \begin{Bmatrix} u_M \\ v_M \\ w_M \end{Bmatrix} \tag{79}$$

$$\begin{Bmatrix} \dot{\phi}_M \\ \dot{\theta}_M \\ \dot{\psi}_M \end{Bmatrix} = [\mathbf{H}_M] \begin{Bmatrix} p_M \\ q_M \\ r_M \end{Bmatrix} \tag{80}$$

The dynamic equations are formed by summing forces and moments about the composite mass center in the body reference frame and equating the result to the time derivative of linear and angular momentum.

$$\begin{Bmatrix} \dot{u}_M \\ \dot{v}_M \\ \dot{w}_M \end{Bmatrix} = \frac{1}{m_M} \begin{Bmatrix} X_M \\ Y_M \\ Z_M \end{Bmatrix} - \begin{bmatrix} 0 & -r_M & q_M \\ r_M & 0 & -p_M \\ -q_M & p_M & 0 \end{bmatrix} \begin{Bmatrix} u_M \\ v_M \\ w_M \end{Bmatrix} \tag{81}$$

$$\begin{Bmatrix} \dot{p}_M \\ \dot{q}_M \\ \dot{r}_M \end{Bmatrix} = [I_M]^{-1} \begin{Bmatrix} L_M \\ M_M \\ N_M \end{Bmatrix} - [I_M]^{-1} \begin{bmatrix} 0 & -r_M & q_M \\ r_M & 0 & -p_M \\ -q_M & p_M & 0 \end{bmatrix} [I_M] \begin{Bmatrix} p_M \\ q_M \\ r_M \end{Bmatrix} \tag{82}$$

The forces and moments in the two equations above contain contributions from weight *(W)*, and aerodynamics *(A)*. Note that the connection forces are removed by assuming the entire system is rigid.

$$\begin{Bmatrix} X_M \\ Y_M \\ Z_M \end{Bmatrix} = \begin{Bmatrix} X_W \\ Y_W \\ Z_W \end{Bmatrix} + \sum_{i=1}^{N} \begin{Bmatrix} X_{Ai} \\ Y_{Ai} \\ Z_{Ai} \end{Bmatrix} \tag{83}$$

$$\begin{Bmatrix} L_M \\ M_M \\ N_M \end{Bmatrix} = \sum_{i=1}^{N} \begin{Bmatrix} L_{Ai} \\ M_{Ai} \\ N_{Ai} \end{Bmatrix} + S_{B_M}(\vec{r}_{B_M - B_i}) \begin{Bmatrix} X_{Ai} \\ Y_{Ai} \\ Z_{Ai} \end{Bmatrix} \tag{84}$$

The individual aerodynamic forces and moments on each aircraft are then computed using equations (11)-(20). As the control system uses control to directly control pitch and roll attitudes of each aircraft, this model is further simplified to a two state system. First, the pitch and roll dynamics are simplified such that $\dot{\theta}_i = q_i$ and $\dot{\phi}_i = p_i$, and then $\ddot{\theta}_i = \dot{q}_i$ and $\ddot{\phi}_i = \dot{p}_i$. Using equation (82) and splitting the forces and moments

into forces and moments that include effects of the aileron and elevator and forces and moments that do not, the equations for the pitch and roll dynamics of the meta aircraft system is approximately equal to the following equation.

$$\ddot{\vec{x}}_M = \vec{F_M} + \sum_{n=1}^{N} G_n \vec{u}_n \tag{85}$$

where

$$\vec{F}_M = \begin{bmatrix} I_{xM} & 0 \\ 0 & I_{yM} \end{bmatrix}^{-1} \left(\begin{Bmatrix} r_M q_M (I_{yM} - I_{zM}) \\ r_M p_M (I_{zM} - I_{xM}) \end{Bmatrix} + \sum_{n=1}^{N} \begin{Bmatrix} (M_{A0n} - (x_n - x_M) Z_{A0n}) \\ (L_{A0n} + (y_n - y_M) Z_{A0n}) \end{Bmatrix} \right) \tag{86}$$

$$G_n = \frac{1}{2} \rho S_n {V_n}^2 \begin{bmatrix} I_{xM} & 0 \\ 0 & I_{yM} \end{bmatrix}^{-1} \begin{bmatrix} b_n C_{l\delta_a} & 0 \\ 0 & (c_n C_{m\delta e} + c_{\alpha_n} (x_n - x_M) C_{L\delta e}) \end{bmatrix} \tag{87}$$

In the equation above $\vec{u}_n = [\delta_{an}, \delta_{en}]^T$ and $\vec{x}_i = [\phi_i, \theta_i]^T$. Note that all rudders are commanded to zero and the thrust commands are all set to the same value of $\delta_{Tn} = K_u(V_T - u_M)$.

5.1.2 Inner Loop Feedback Linearization

The inner loop controller is setup up such that inner loop commands are used to create pseudo controls using standard feedback linearization techniques. If each aircraft can reach the desired pitch and roll commands, the flexibility of the system remains relatively small and the aircraft will act like the rigid system discussed in the previous section. The pseudo control is defined using the equation below[37].

$$\vec{\gamma}_M = \ddot{\vec{x}}_c - K_d(\dot{\vec{x}}_M - \dot{\vec{x}}_c) - K_p(\vec{x}_M - \vec{x}_c) \tag{88}$$

The gains used in the equation above are configuration dependent. In order to obtain these gains a specialized system identification procedure is performed to obtain the maximum pitch and roll rates of the meta aircraft configuration (q_{MAX}, p_{MAX}). Using these values of maximum pitch and roll rate, a first order

approximation can be computed and the natural frequency of the pitch and roll dynamics can be found using the equations below

$$\begin{aligned} t_q &= 0.5236/q_{MAX} \\ \omega_q &= -log(0.004)/t_q \\ t_p &= 0.1745/p_{MAX} \\ \omega_p &= -log(0.004)/t_p \end{aligned} \tag{89}$$

where t_q and t_p are the rise time in seconds to achieve a desired pitch and roll of 30^o and 10^o assuming a constant pitch and roll rate of q_{MAX} and p_{MAX}. The natural frequencies ω_q and ω_p are then computed to obtain a second order approximation to a time response with a rise time of t_q and t_p. The damping ratio is set to 1 to reduce oscillations which directly impacts the amount of flexibility excited in the system. With these definitions the proportional and derivative gains of the inner loop controller are set using the equations below.

$$K_p = \begin{bmatrix} \omega_p^2 & 0 \\ 0 & \omega_q^2 \end{bmatrix}, K_d = \begin{bmatrix} 2\omega_p & 0 \\ 0 & 2\omega_q \end{bmatrix} \tag{90}$$

Finally, the rigid body model is used to cancel out the dynamics using the equation below

$$\vec{\lambda}_M = \vec{\gamma}_M - \vec{F}_M \tag{91}$$

5.1.3 Outer Loop PID Controller

The relationship between outer loop heading and altitude commands to inner loop pitch and roll commands is conventional PID with configuration dependent gains.

$$\begin{aligned} \theta_C &= \tfrac{K_Z}{2V_T}(z_M - z_c) + 0.05\tfrac{K_Z}{2V_T}\textstyle\int(z_M - z_c)dt \\ \phi_C &= -N_{COL}\tfrac{K_\psi}{V_T\eta}(\psi_M - \psi_c) \end{aligned} \tag{92}$$

In the equations above, V_T is the trim velocity of a single aircraft, N_{COL} is the number of columns in

the meta aircraft system ,$\eta = b(p_{MAX} + q_{MAX})/(2c)$, and K_Z and K_ψ are outer loop gains determined from the equations below.

$$\begin{aligned} t_\psi &= 2t_p \\ K_\psi &= -log(0.02)/t_\psi \\ t_z &= 2t_q \\ K_Z &= -log(0.02)/t_z \end{aligned} \tag{93}$$

Here, the rise time of the outer loop dynamics are assumed to be twice as slow as the inner loop dynamics and are also assumed to be first order, hence the 0.02 inside the log() function.

5.1.4 Control Allocation

The control allocation scheme is formulated by concatenating all control surfaces into 1 vector such that

$$\sum_{i=n}^{N} G_n \vec{u}_n = G\vec{v} \tag{94}$$

where

$$\vec{v} = \begin{Bmatrix} \delta_{a1} \\ \delta_{e1} \\ \vdots \\ \delta_{aN} \\ \delta_{eN} \end{Bmatrix} \tag{95}$$

Using equations (85),(91), and (94) an equation relating all individual control surfaces to the pseudo controls can be defined.

$$G\vec{v} = \vec{\lambda}_M \tag{96}$$

The equation above is an equation with $2N$ unknowns and only 2 equations. To solve this equation below a minimization routine is used.

$$min(||\vec{v}||) \; such \; that \; G\vec{v} = \vec{\lambda}_M \tag{97}$$

Using the Lagrange multiplier technique, the solution to this minimization is given by the equation below.

$$\vec{v} = G^T(GG^T)^{-1}\vec{\lambda}_M \tag{98}$$

The equation above is then iterated until all control surfaces are less than or equal to the maximum control deflection allowed by the aircraft. The equations above results in the control effort of the entire meta aircraft system provided that every aircraft has the same pitch and roll attitude. However, since the meta aircraft is flexible, this is rarely true. Therefore, equation (98) is computed for every aircraft and only the control components are used for the ith aircraft. For example, aircraft i will use the controls computed by $\vec{v} = G^T(GG^T)^{-1}\vec{\lambda}_i$ whereas aircraft j will use the controls computed by $\vec{v} = G^T(GG^T)^{-1}\vec{\lambda}_j$. This technique has increased the robustness of this controller. Overall this controller seeks to minimize flexibility in the system by forcing all aircraft to achieve the same pitch and roll attitudes while minimizing control effort.

5.2 Example Simulation Results

In order to show the versatility of the control system described above multiple aircraft configurations are simulated in a variety of longitudinal and lateral maneuvers. The example aircraft used is described in section 2.7. In addition, the joint properties are set to provide a realistic connection joint of this aircraft which is also described in section 2.7.

5.2.1 Wing Tip to Wing Tip Configuration

Example simulation results are shown for altitude and heading angle response of the wing tip to wing tip configuration starting with one aircraft and increasing to 10 aircraft. Here, all aircraft have zero initial

attitudes and angular velocities with a forward speed of 20 m/s. The altitude of each vehicle is 200 m. The x_i and y_i initial conditions are set such that the load between the joints of each aircraft is zero. Each configuration is commanded to an altitude of 210 m and $\psi = 10^o$. Figures 82 and 83 show the average altitude and heading of the meta aircraft configuration. Here, the altitude response of the different configurations is almost identical. This is due to the almost negligible change in the longitudinal modes and the pitch symmetry that was shown when analyzing the flight dynamic modes. The heading response slows down with increasing number of aircraft as the lateral modes become slower due to the increase in lateral size of the aircraft. However, the controller seems to be robust to changes in wing tip to wing tip connected flight. In Figure 83 notice that there is a sometimes large heading angle deviation from a smooth response to 10^o around 3 seconds. This is because at 3 seconds the altitude controller pitches the aircraft in a nose down fashion to level out the meta aircraft. This spike in pitch rate and large change in pitch attitude leads to a hiccup in the heading angle response. This has nothing to do with the heading response of meta aircraft and everything to do with the over actuation in altitude.

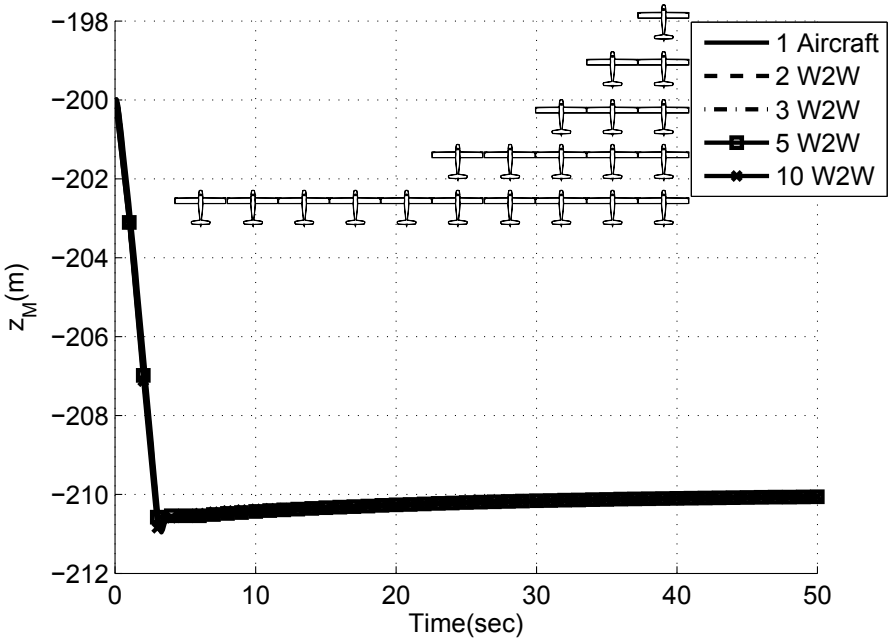

Figure 82: Z_M (m) vs. Time(sec) for Different Wing Tip to Wing Tip Configurations

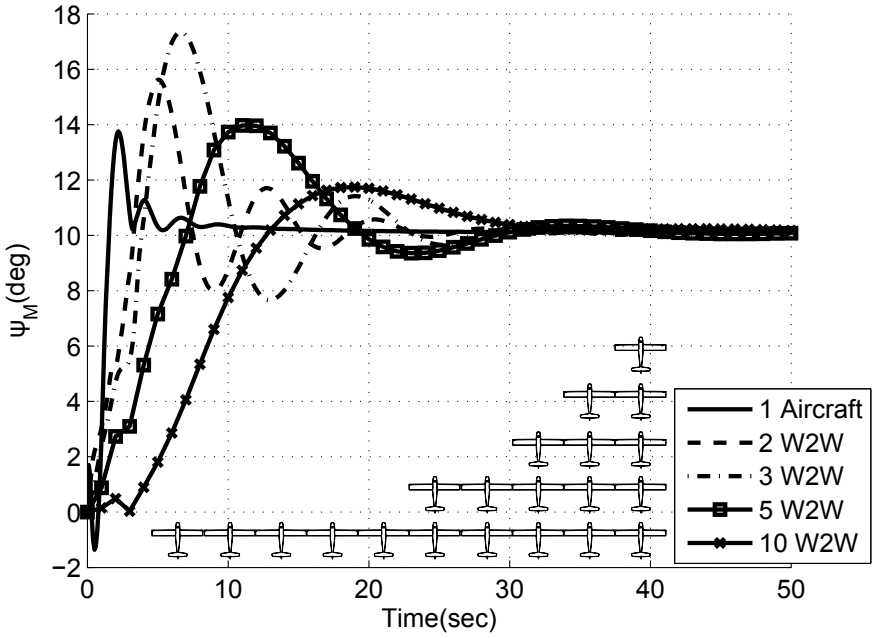

Figure 83: ψ_M **(deg) vs. Time(sec) for Different Wing Tip to Wing Tip Configurations**

Due to the attitude matching controller, the roll, pitch and yaw angles of each individual aircraft are kept fairly similar as shown by Figures 84-86 for a 3 aircraft system. These aircraft show that the pitch and roll response is set such that the angles saturate to 15^o within the first 5 seconds. The pitch angle then oscillates to about 3^o. It is this change in the pitch angle that causes the subtle change in heading angle. The control allocation scheme provides individual control to each aircraft in this configuration. Figures 87 and 88 show the elevator and aileron deflections of each aircraft in the wing tip to wing tip configuration with 3 aircraft. Here, the elevator angles are identical while the aileron angles differ between each aircraft. In addition, the Figure shows that the middle aircraft attains a trim value of zero while the aircraft to its right and its left attain a slight equal and opposite non-zero value. This is a direct consequence of the lifting line model producing non-uniform lift across the system. If the lifting line model were removed the trim aileron deflections would be zero.

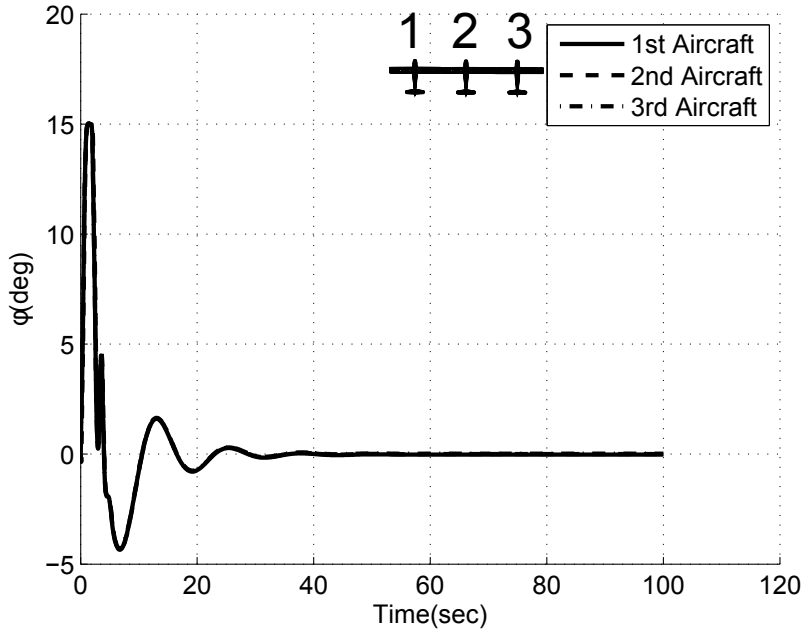

Figure 84: ϕ_i **(deg) vs. Time(sec) for Individual Aircraft in a Three Aircraft Wing Tip to Wing Tip Configuration**

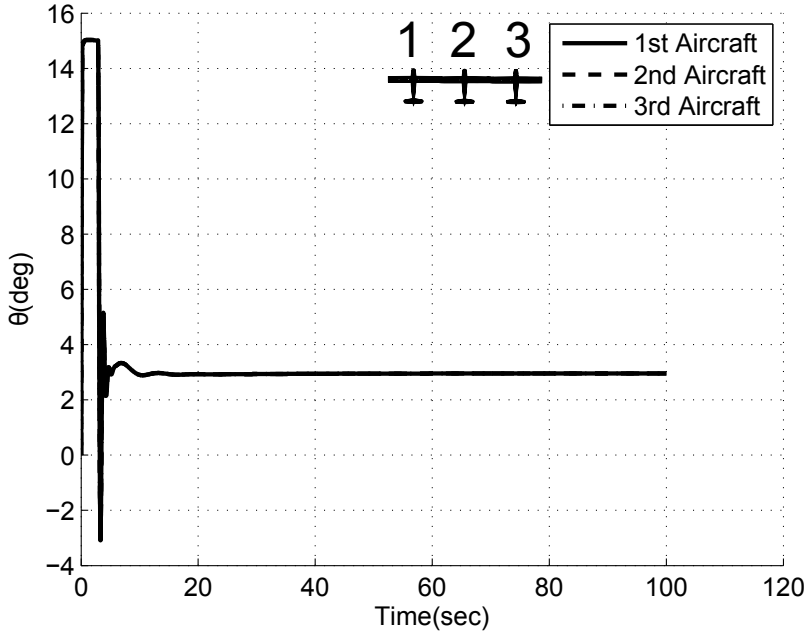

Figure 85: θ_i **(deg) vs. Time(sec) for Individual Aircraft in a Three Aircraft Wing Tip to Wing Tip Configuration**

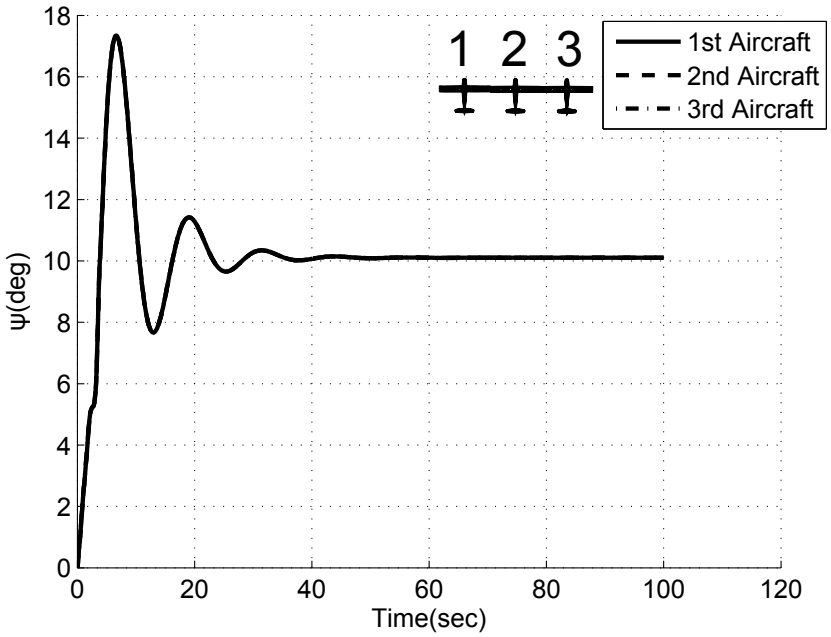

Figure 86: ψ_i **(deg) vs. Time(sec) for Individual Aircraft in a Three Aircraft Wing Tip to Wing Tip Configuration**

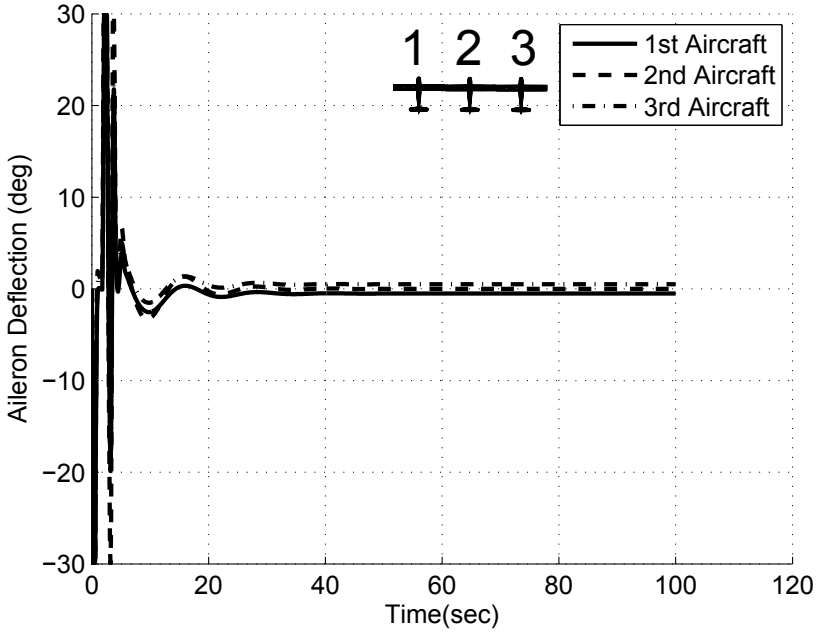

Figure 87: Aileron Deflection (deg) vs. Time(sec) for Individual Aircraft in a Three Aircraft Wing Tip to Wing Tip Configuration

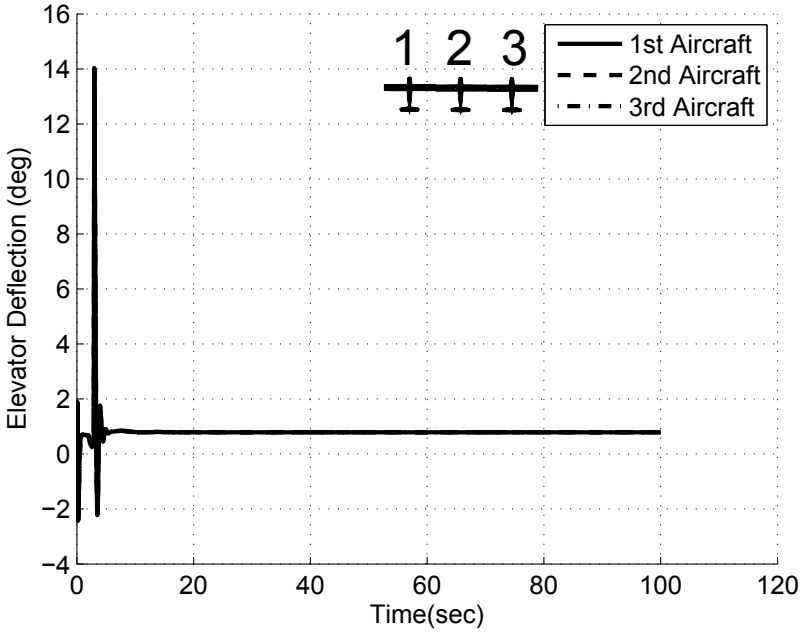

Figure 88: Elevator Deflection (deg) vs. Time(sec) for Individual Aircraft in a Three Aircraft Wing Tip to Wing Tip Configuration

Although the controller is successful in controlling 10 aircraft wing tip to wing tip, note that when 10 aircraft are controlled, significant flexing between aircraft is seen. Figure 89 shows the roll angle for a 10 aircraft configuration. It is clear that multiple flapping modes are being excited by this controller.

5.2.2 Tip to Tail Configuration

When attempting to control aircraft in a tip to tail configuration, it is important to note the change in the flight dynamic modes of the meta aircraft. Figure 90 shows the change in the phugoid mode as a function of number of connected aircraft for the wing tip to wing tip and tip to tail configuration. This data is obtained and explained in section 3.1. When aircraft are connected wing tip to wing tip, the phugoid mode is largely unchanged, however when connected tip to tail, the phugoid mode becomes critically damped at 3 connected aircraft and unstable.

These flight dynamic modes directly effect the control response of the aircraft. Figure 91 shows the response in altitude of aircraft connected tip to tail. Here, the controller used in this simulation successfully

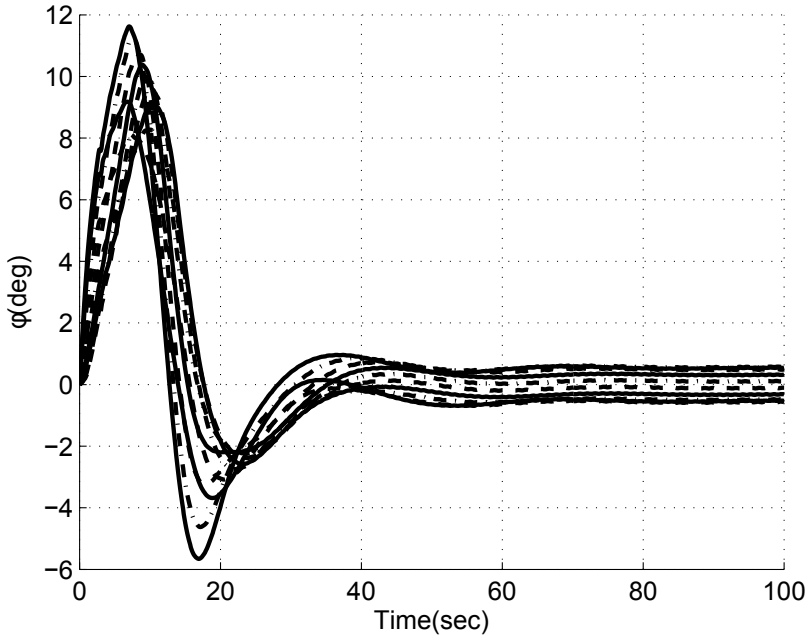

Figure 89: Roll Angle (deg) vs. Time(sec) for Individual Aircraft in a Ten Aircraft Wing Tip to Wing Tip Configuration

trims the altitude from 1 to 3 aircraft; however, once the aircraft has 4 aircraft connected the controller loses its effectiveness and fails to control a 5 aircraft configuration.

However, examining the heading response to aircraft connected tip to tail the controller is successful in controlling all aircraft as shown in Figure 92. Thus, the controller is successful in controlling the heading response of the aircraft but the longitudinal modes change so drastically that the controller is incapable of controlling the meta aircraft system. Still, with three aircraft connected tip to tail, the meta aircraft controller successfully allocates controls for the three aircraft as shown in Figures 93 and 94. Here the aileron deflection are almost identical while the elevator angles are completely different. This is because each elevator applies a different moment to the composite aircraft thus different control are actuated to each aircraft. The control allocation routine is responsible for minimizing the control effort leading to different control deflections based on the location of the aircraft.

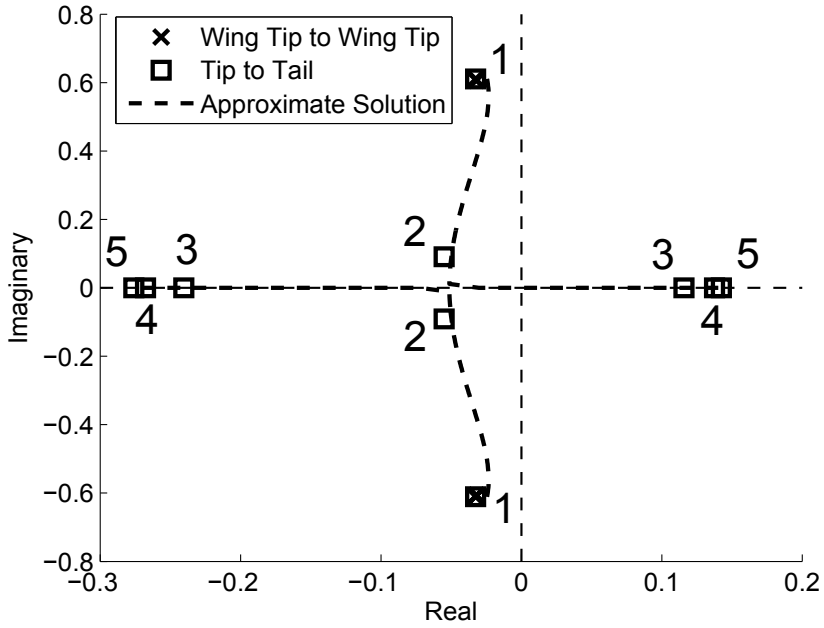

Figure 90: Phugoid Mode as a Function of Number of Connected Aircraft

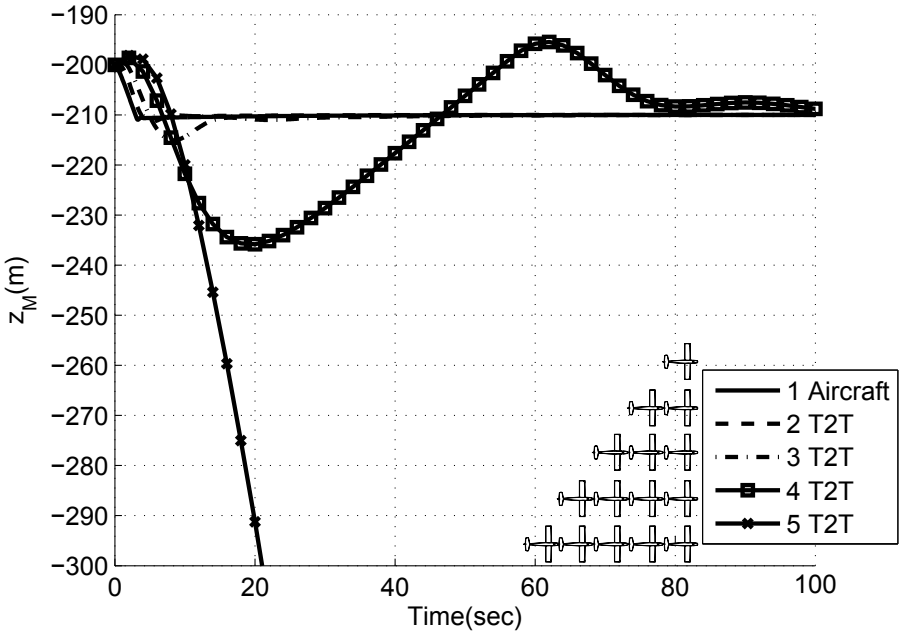

Figure 91: Z_M (m) vs. Time(sec) for Different Tip to Tail Configurations

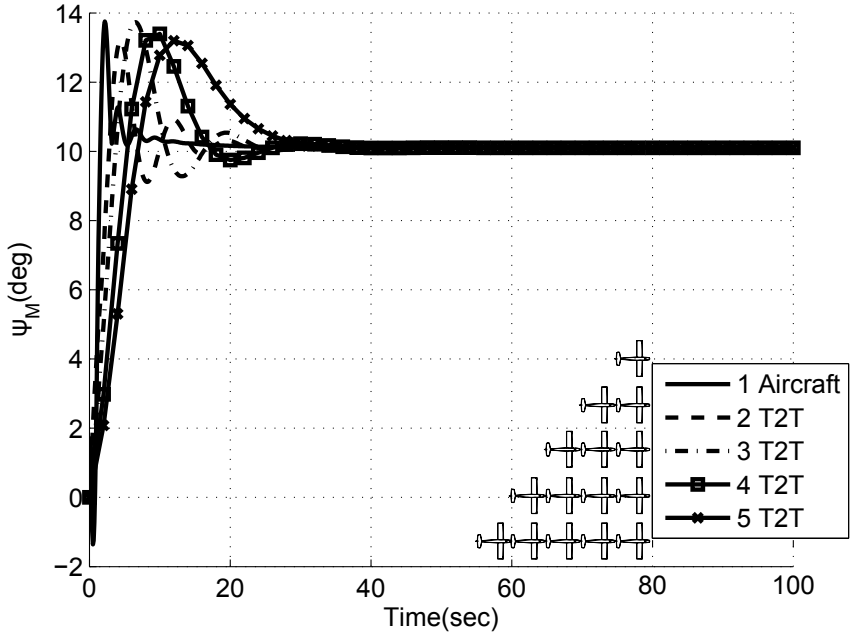

Figure 92: ψ_M **(deg) vs. Time(sec) for Different Tip to Tail Configurations**

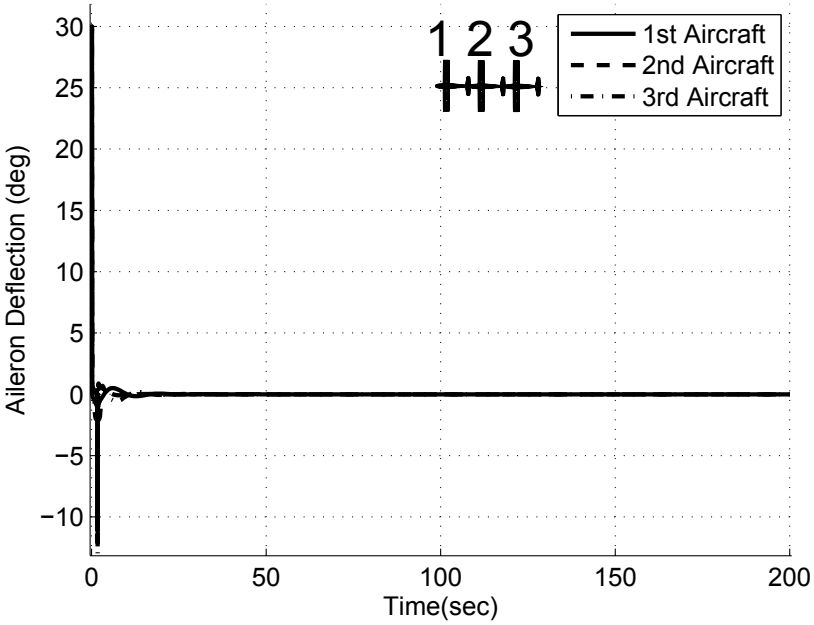

Figure 93: Aileron Deflection (deg) vs. Time(sec) for Individual Aircraft in a Three Aircraft Tip to Tail Configuration

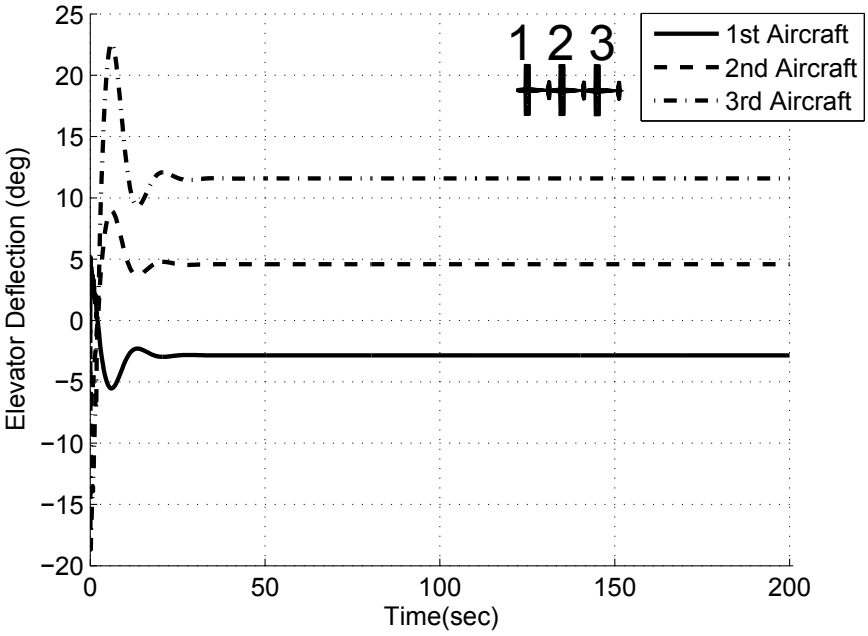

Figure 94: Elevator Deflection (deg) vs. Time(sec) for Individual Aircraft in a Three Aircraft Tip to Tail Configuration

5.2.3 Lattice Configurations

Lattice structures, provide a way to connect more aircraft in a tighter space. Figures 95 and 96 show the control response of two lattice configurations in a 2x2 configuration and 3x3 configuration. Again the controller is robust to these types of configurations as well.

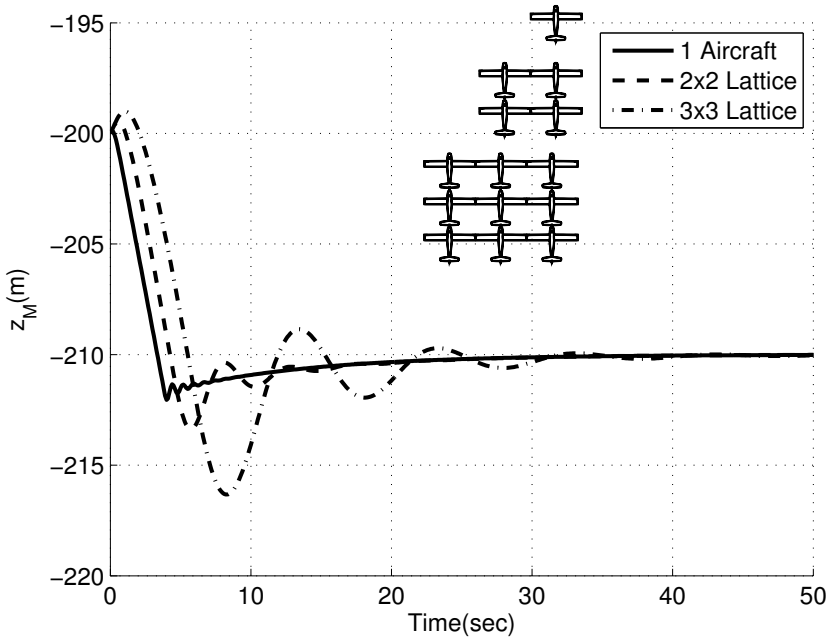

Figure 95: Z_M **(m) vs. Time(sec) for Different Lattice Configurations**

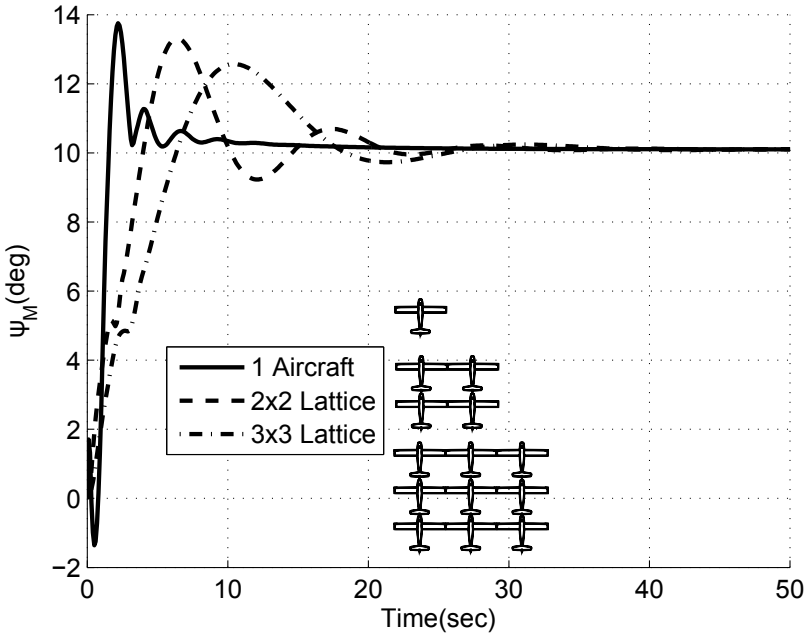

Figure 96: ψ_M **(deg) vs. Time(sec) for Different Lattice Configurations**

5.3 Meta Aircraft Performance

In order to explore the performance of different types of configurations simulations are conducted to observe the mean deviation from a trim point in heavy winds. In addition, the overall increase in L/D is computed for a variety of different configurations. The aircraft used in the following simulations is described in section 2.7 with winds using the atmospheric wind model described in section 2.6.

5.3.1 Tracking Performance in Winds

Gust sensitivity of a single aircraft is a practical design challenge for many aircraft. Often, atmospheric winds reduce the performance of trajectory tracking and can even cause aircraft to fail their mission and not connect. Connecting aircraft together can be a solution to gust sensitivity. To investigate this, the atmospheric wind model, explained in section 2.6, is set to provide mean gusts of $8m/s$ and a turbulence standard deviation of $0.5m/s$. A variety of configurations are flown in this randomized wind field while trying to maintain a steady and level flight path. Since the controller detailed in Section 5.1 fails at controlling four aircraft connected tip to tail, the analysis is truncated to simply a 3x3 grid. Thus, the maximum number of aircraft connected tip to tail and wing tip to wing tip is 3. However, lattice structures are simulated as well with 9 aircraft connected in a 3x3 grid being the largest meta aircraft analyzed.

The simulation is run for 100 wind scenarios for 50 seconds for each configuration and the mean values of the error in the desired altitude and crossrange commands are reported for the entire 50 second simulation. In addition, the mean error in trim pitch, roll and yaw are reported. The next few Figures show the results of this study, however note that the data is slightly rough due to the discrete nature of meta aircraft. That is, it is only possible to simulate discrete configurations and it is impossible to simulate 2.5 aircraft connected wing tip to wing tip for example.

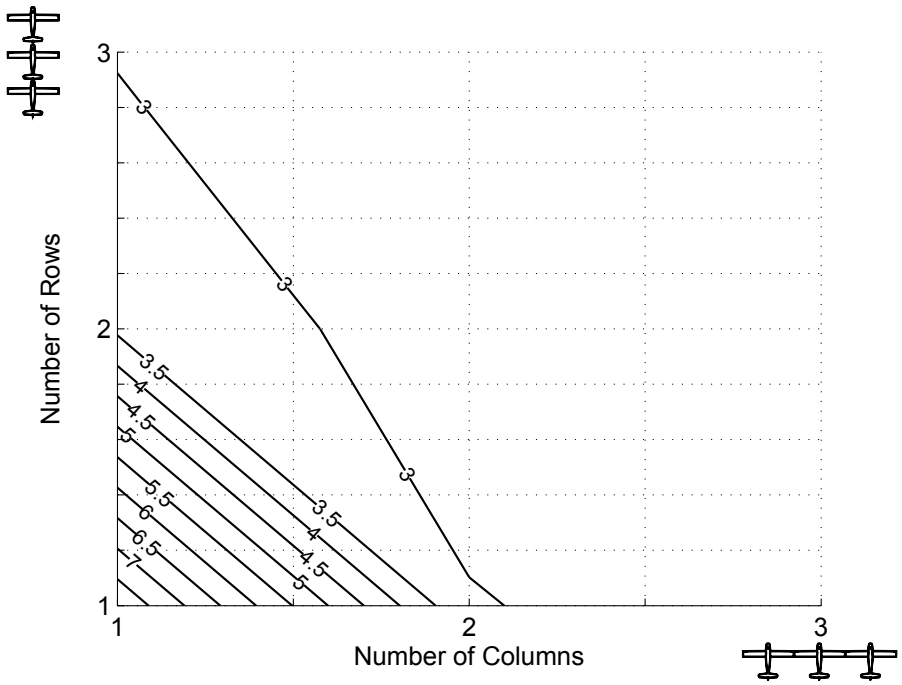

Figure 97: Mean Crossrange Error(m) for Different Meta Aircraft Configurations Flying in 8m/s Winds

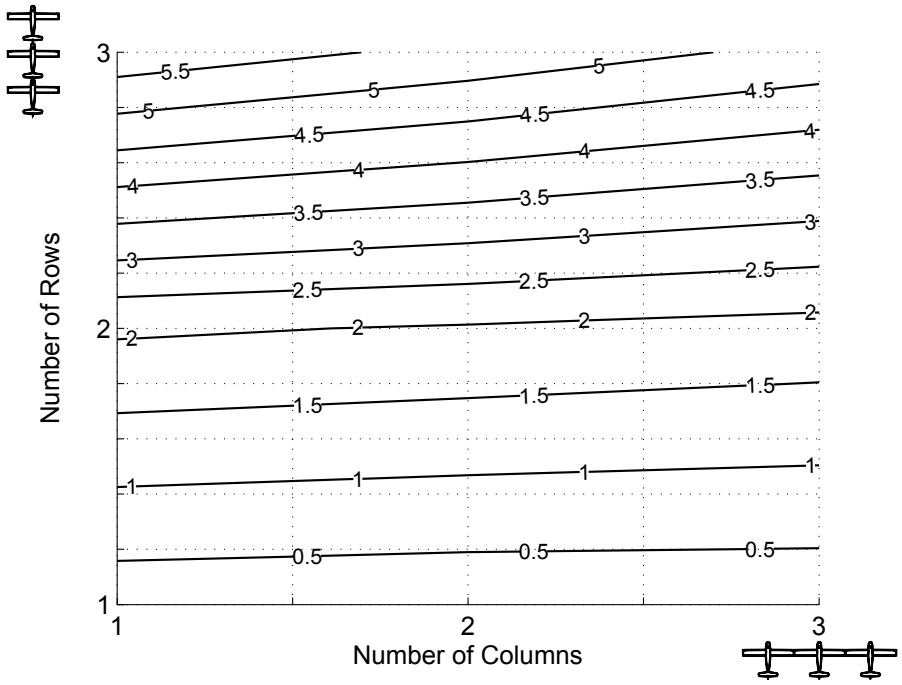

Figure 98: Mean Altitude Error(m) for Different Meta Aircraft Configurations Flying in 8m/s Winds

Figures 97 and Figure 98 show that if trying to maintain a desired altitude the single aircraft is the best configuration. However, crossrange tracking performance is the worst for the single aircraft. Crossrange performance increases when aircraft are connected tip to tail and wing tip to wing tip. However, wing tip to wing tip flight shows no change in performance to altitude whereas tip to tail and lattice configurations show an equal decrease in altitude tracking performance. Figures 99-101 show that wing tip to wing tip flight causes an increase in roll tracking performance, a increase in yaw tracking performance and an increase in pitch tracking performance suggesting that the wing tip to wing tip configuration has a large increase in tracking performance. Tip to tail configurations exhibit a small increase in roll angle tracking performance a decrease in pitch angle tracking performance and an increase in yaw angle tracking performance.

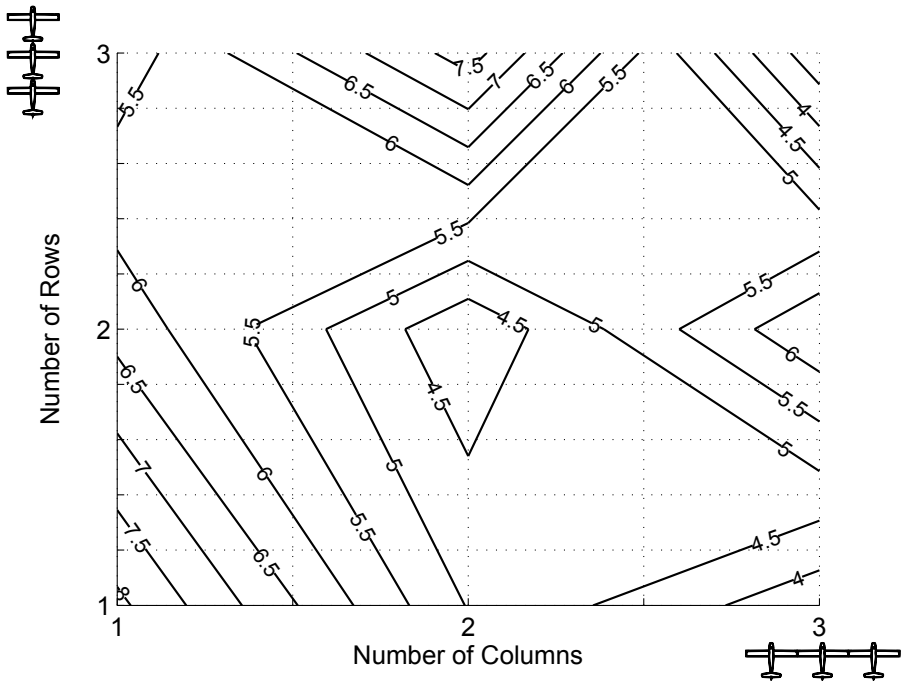

Figure 99: Mean Roll Angle Error(deg) for Different Meta Aircraft Configurations Flying in 8m/s Winds

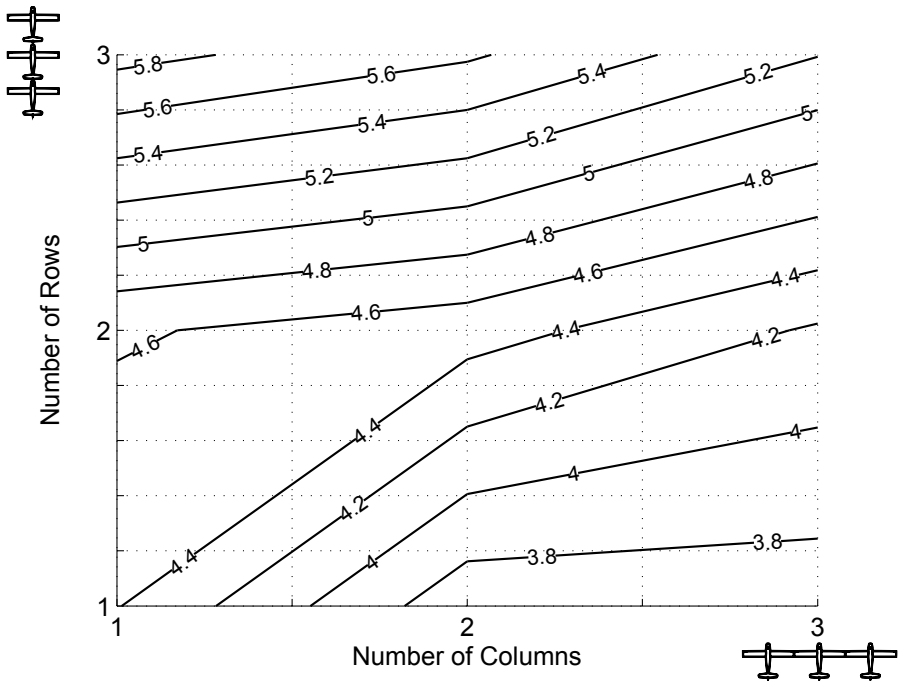

Figure 100: Mean Pitch Angle Error(deg) for Different Meta Aircraft Configurations Flying in 8m/s Winds

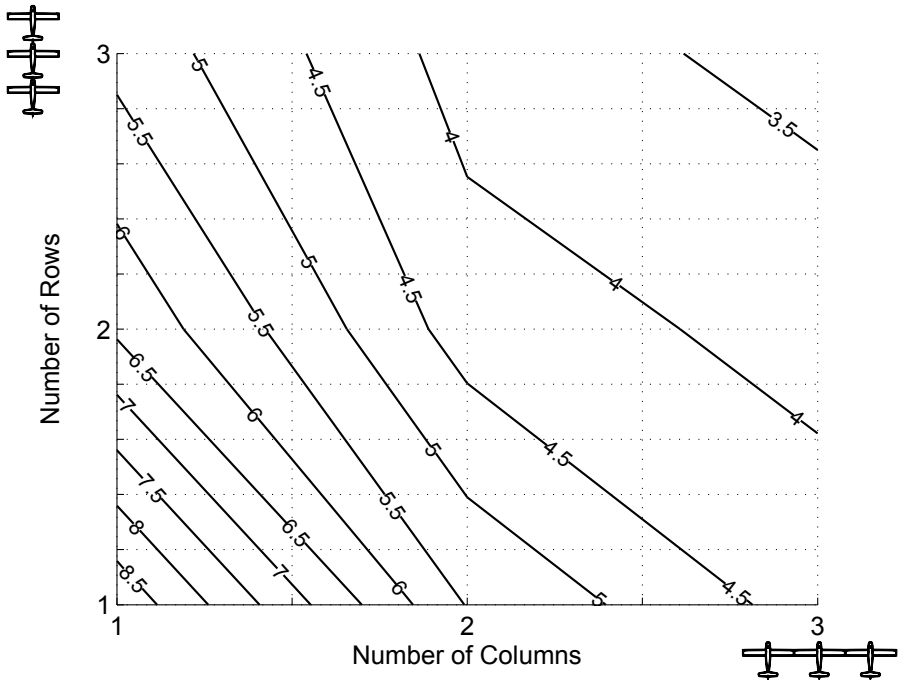

Figure 101: Mean Yaw Angle Error(deg) for Different Meta Aircraft Configurations Flying in 8m/s Winds

5.3.2 Lift to Drag Analysis

Another benefit of flying in a connected configuration is the increase in Lift-to-Drag ratio (L/D). Connecting aircraft wing tip to wing tip reduces the effect of wing tip vortices and thus increases lift which directly impacts range and endurance. In order to compute the interaction between aircraft, all wings are split into aerodynamic elements and a horseshoe vortex is placed at each element. These vortices are used to compute the aerodynamic interaction between aircraft by using strip theory coupled to a vortex lifting line wake model as detailed in Section 2.2. This interaction model can predict the increase in lift on all aircraft. The following simulations detail the overall lift to drag ratio for different configurations. The aircraft used in these simulations is detailed in section 2.7. The initial conditions are steady and level flight with a trim speed of 20 m/s. In the following simulations three values of lift to drag are reported. The individual lift to drag ratio is given by the simple formula

$$L/D_i = \frac{L_i}{D_i} \tag{99}$$

where L_i is the lift produced by one aircraft and D_i is the drag produced by one aircraft in trim. In any given meta aircraft configuration the minimum and maximum Lift to Drag ratio can be computed for each individual aircraft using the equations below

$$\begin{aligned} L/D_{min} &= min(L/D_i),\ i\ \epsilon\ [1, N_{AC}] \\ L/D_{max} &= max(L/D_i),\ i\ \epsilon\ [1, N_{AC}] \end{aligned} \tag{100}$$

Finally, the average Lift to Drag ratio can be computed using the equation below.

$$L/D_{avg} = \frac{\sum_{i=1}^{N_{AC}} L/D_i}{N_{AC}} \tag{101}$$

Figure 102 shows a contour plot of L/D_{avg} over the entire meta aircraft system. Wing tip to wing tip connected flight clearly provides the best overall increase in lift to drag ratio. The lift to drag ratio for a

single aircraft is 6.492 whereas L/D_{avg} for a wing tip to wing tip meta aircraft of 4 aircraft is 6.7218, an increase of 3.5%. Furthermore, the average lift to drag ratio decreases as aircraft are connected tip to tail. This is due to the trailing aircraft flying in the downwash of the leading aircraft reducing lift.

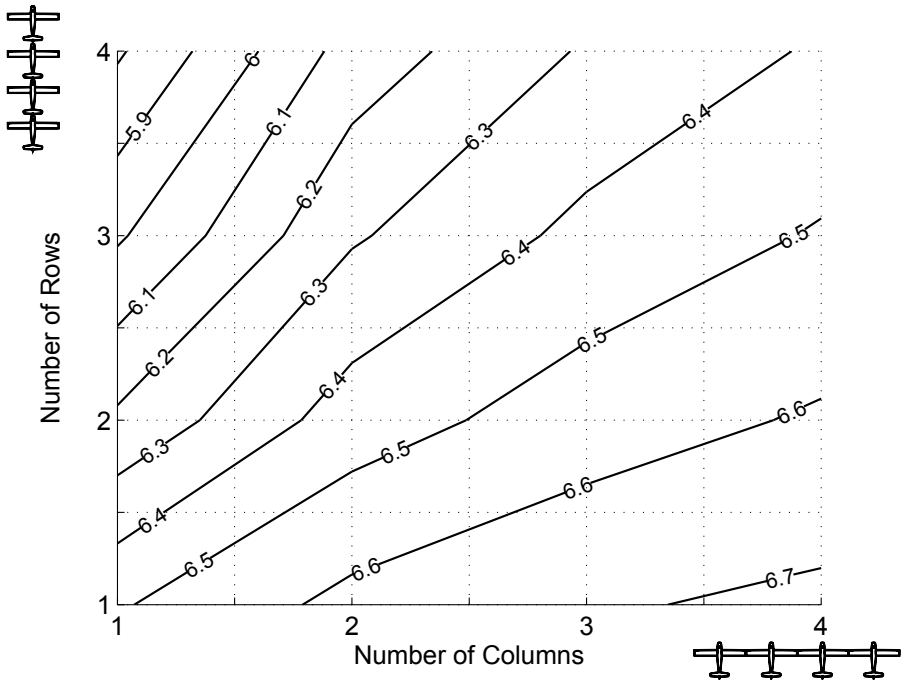

Figure 102: Average Lift to Drag Ratios for Different Meta Configurations(L/D_{avg})

This Figure only shows L/D_{avg} over the entire meta aircraft system as given by equation (101). The minimum and maximum L/D ratio is plotted for the same meta aircraft systems as shown in Figures 103 and 104 using equation (100). Figure 103 again shows that tip to tail and lattice configurations reduce L/D_{min}; however, Figure 104 shows that tip to tail and lattice structures actually have the highest L/D_{max} even though L/D_{avg} is reduced. In tip to tail configurations the lead aircraft have higher L/D_i ratios while the trailing aircraft fly in the downwash and have lower L/D_i ratios.

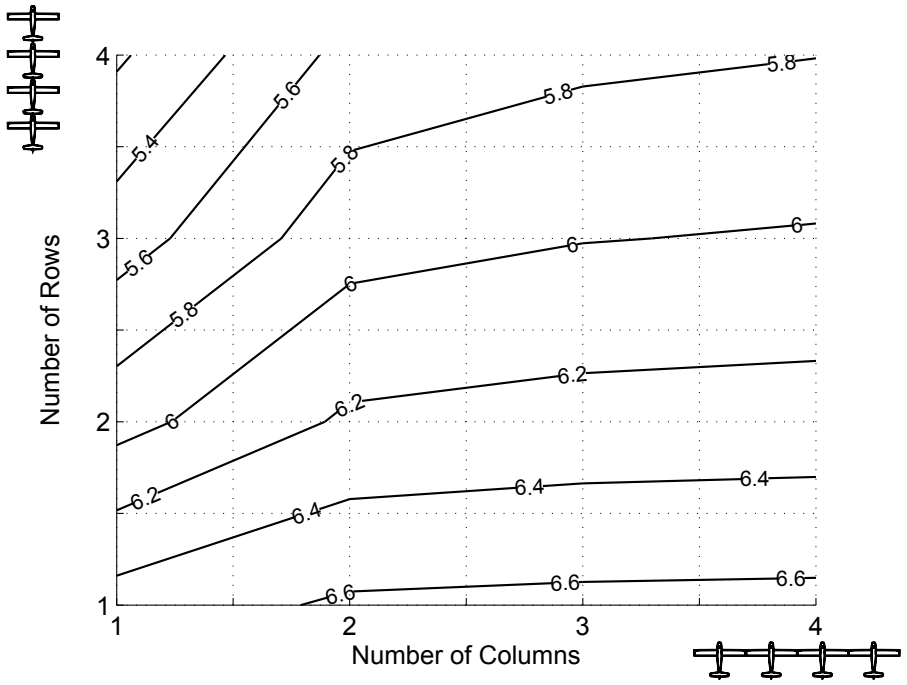

Figure 103: Minimum Lift to Drag Ratios for Different Meta Configurations(L/D_{min})

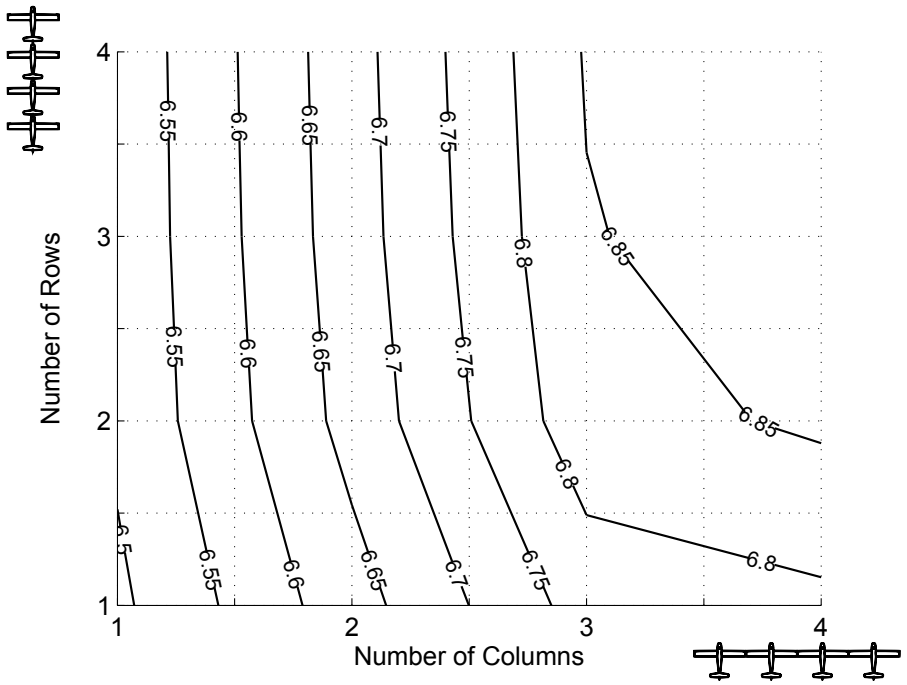

Figure 104: Maximum Lift to Drag Ratios for Different Meta Configurations(L/D_{max})

Although L/D_{avg} accounts for the average Lift to Drag ratio a good test of the increasing benefit is to compute the total percent increase over the entire meta aircraft system using the equation below.

$$P_{total} = N_{AC}(\frac{L/D_{avg}}{L/D_1} - 1) \tag{102}$$

Here L/D_1 is the lift to drag ratio of a single aircraft flying alone. Thus, if 4 aircraft are connected wing tip to wing tip $L/D_{avg} = 6.7218$ and $L/D_1 = 6.492$. This corresponds to an average increase of 3.5%. However, there are 4 aircraft in this configuration thus all 4 aircraft experience the increase of 3.5% and $P_{total} = 3.5*6\% = 21\%$. Figure 105 shows the total percent increase of the same meta aircraft configurations. Again the basic trend is that tip to tail flight reduces the overall percent increase down to -40% whereas wing tip to wing tip increases the overall L/D ratio by up to 15% if 4 aircraft are connected. Lattice structures have a bifurcation point where the percent change goes from positive to negative as denoted by the arrows signifying positive and negative gains.

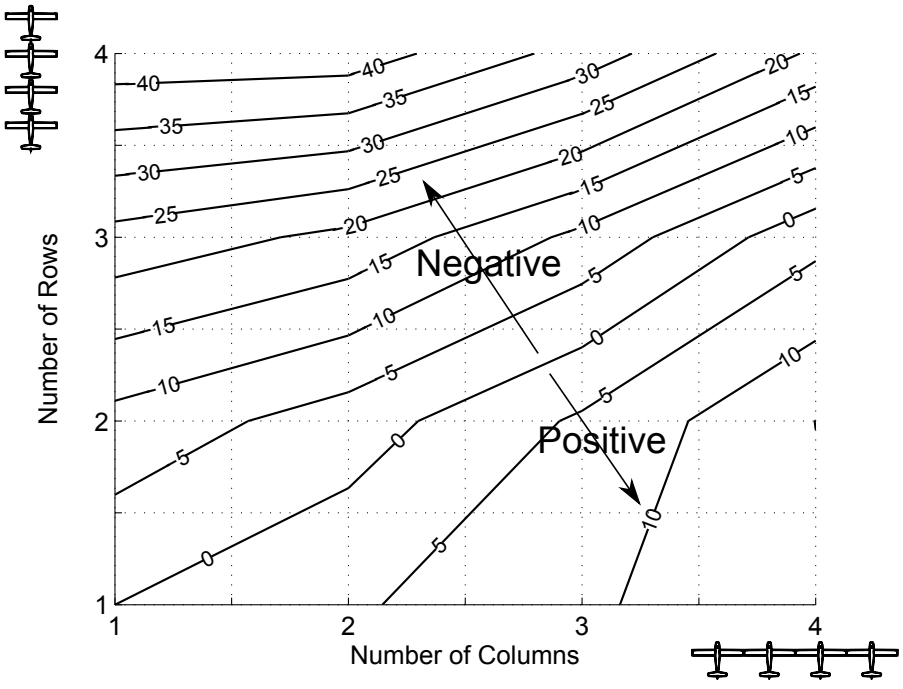

Figure 105: Total Percent Increase in Lift to Drag Ratios for Different Meta Configurations

Note, that the analysis run above is only for a single trim angle of attack of about $\alpha = 2^o$. A more interesting study is to plot the maximum lift to drag ratio for each configuration by solving for this state numerically. The lift-to-drag ratio of every configuration is a function of the angle of attack. For example, Figure 106 shows the lift to drag ratio for a single aircraft as a function of angle of attack. The maximum lift to drag ratio is 10.21 at and angle of attack of 5.25 degrees. The same analysis can be reported for all configurations. Figures 107 and 108 shows the maximum overall lift to drag ratio for every configuration and the angle of attack required for this angle of attack.

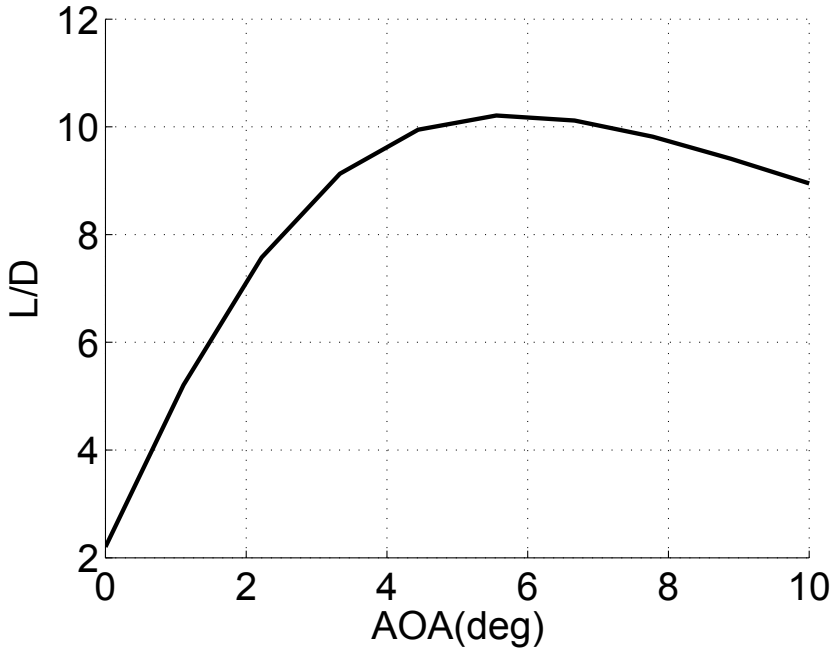

Figure 106: Lift to Drag Ratio of One Aircraft versus Angle of Attack(deg)

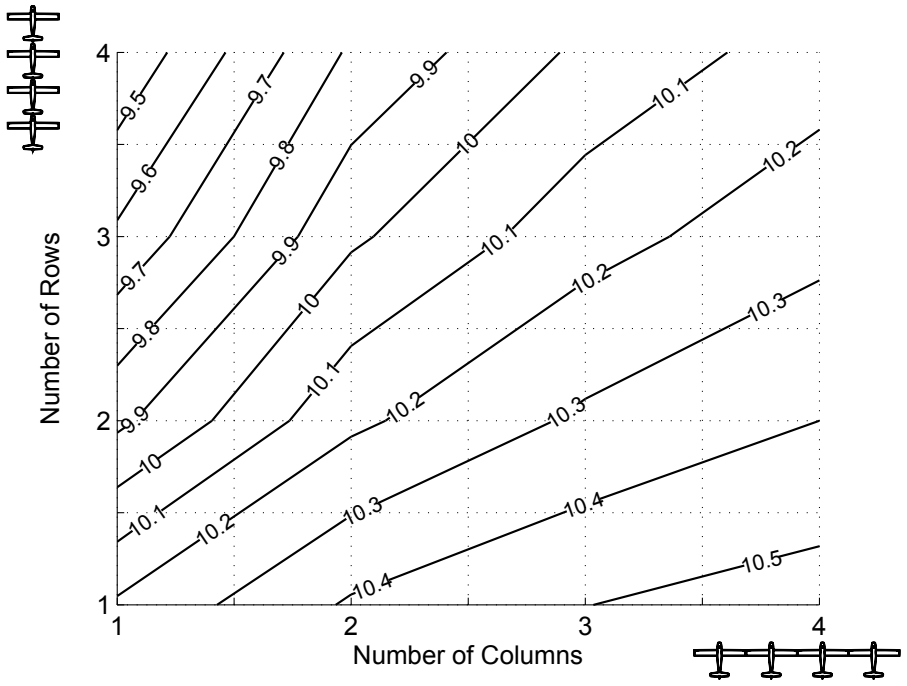

Figure 107: Average Lift to Drag Ratios for Different Meta Aircraft Configurations Flying at Angle of Attack for $(L/D)_{max}$

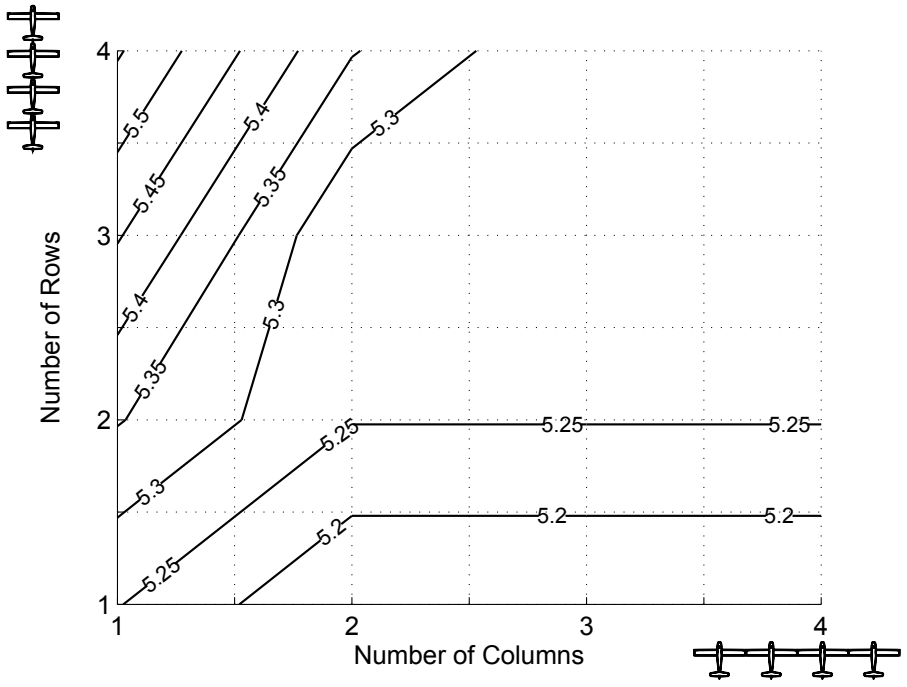

Figure 108: Angle of Attack (deg) for Maximum (L/D)

Figure 107 shows a similar trend as Figure 102. The difference is that the lift to drag ratio of a single aircraft is 10.215 and the lift to drag ratio of 4 aircraft connected wing tip to wing tip is 10.547, an increase of 3.1%. This increase is nearly the same at the trim angle of attack lift to drag ratio. Figure 108 shows that the angle of attack for maximum lift to drag ratio is between 5.1 and 5.5 degrees. The angle of attack required for maximum lift to drag ratio increases for tip to tail aircraft and stays about the same for wing tip to wing tip connected flight.

Figure 109 shows the total percent increase in lift to drag ratio for meta aircraft configurations using equation (102). Looking at Figure 109 and 105 shows that the percent increase is nearly identical regardless of the angle of attack you are flying. This is an important result as the benefit obtained from connecting a meta aircraft is independent of the trim angle of attack. Also, the trim angle of attack is nearly constant leading to simple control design.

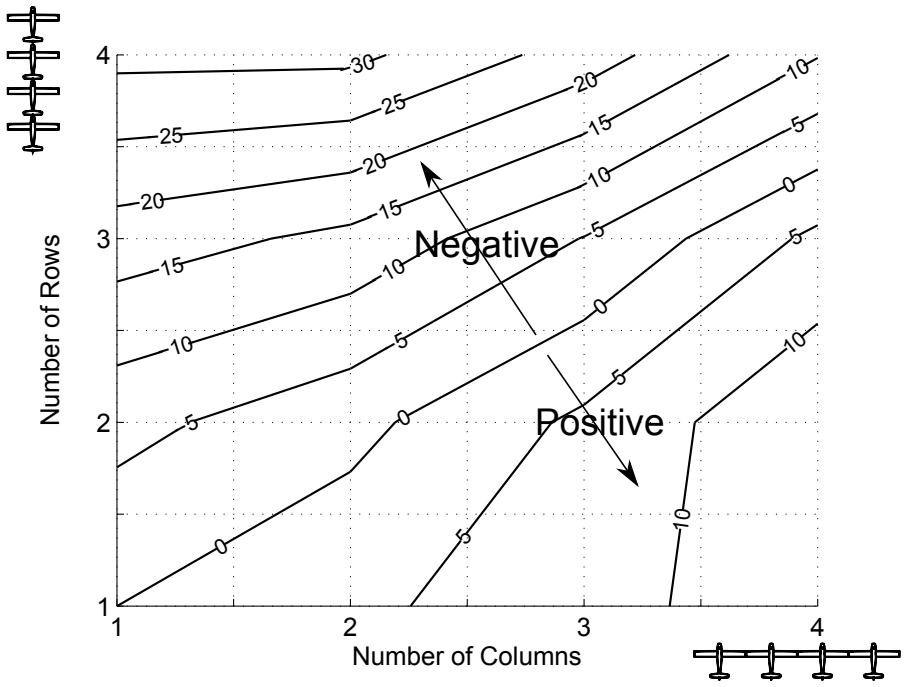

Figure 109: Total Percent Increase in Lift to Drag Ratios for Different Meta Configurations Flying at an Angle of Attack for $(L/D)_{max}$

6 Conclusions and Future Work

6.1 Conclusions

This dissertation explored flight dynamics and control of meta aircraft. The meta aircraft considered here, contains individual flying aircraft that connect in flight to form a larger meta aircraft. Chapter 2 detailed the overall simulation model used throughout the simulation studies. Chapter 3 explored the change in flight dynamic mode shapes of meta aircraft as a function of the configuration. Chapter 4 derived a connection control law for two aircraft attempting to connect in flight and explored controller performance against a variety of different design parameters. Finally, Chapter 5 utilized a control law for a meta aircraft in order to study meta aircraft performance in winds.

The simulation tool explained in Chapter 2 is comprehensive and permits the investigation of flight dynamics and controls of meta aircraft by focusing on key modeling aspects. The dynamic simulation tool was created using a fully non-linear six degree of freedom model where each aircraft is excited by aerodynamics, gravity, magnet and contact loads. The basic connection mechanism for this meta aircraft is passive magnets placed at the wing tips of each aircraft. When aircraft are close, collisions can occur giving rise to contact forces and moments. The simulation includes a non-linear magnetic model and a soft contact model. Furthermore, when aircraft wing tips are close, wing tip vortices interact changing the overall lift distribution of the wings. To model this effect, all wings are split into aerodynamic elements and a horseshoe vortex is placed at each element. These vortices are used to compute the aerodynamic interaction between aircraft by using strip theory coupled to a vortex lifting line wake model. When aircraft are fully connected after a connection event the connection joint changes to a simplified linear magnet routine and a contact model using linear and rotational springs and dampers.

In Chapter 3, the flight dynamics of meta aircraft configurations has been investigated. These fundamental dynamics are different from the basic individual aircraft kernel used to construct the meta aircraft configuration. For wing tip to wing tip connected flight, the flight dynamic longitudinal modes are unaffected

whereas the lateral modes change considerably. This is due to the pitch axis symmetry of wing tip to wing tip connected flight. The roll mode however, declines due to the quadratic increase in roll inertia and the change in roll damping. For tip to tail flight, it is found that the longitudinal modes become over damped after 3 connected aircraft and can even become unstable. The pitch axis symmetry that was encountered in wing tip to wing tip connected flight is seen as a roll axis symmetry in tip to tail connected flight. The roll mode for tip to tail connected flight is nearly constant but declines slightly due to the trailing aircraft that fly in the wake of the leading aircraft causing the roll damping to decline. In addition, the pitch damping of the tip to tail configuration increases in a similar manner to the roll damping in wing tip to wing tip connected flight. This increase in pitch damping seen in tip to tail connected flight coupled with the quadratic increase in pitch inertia causes the longitudinal modes to become critically damped and even unstable.

Meta aircraft also introduces complex flexible modes which increase in complexity as the number of aircraft connected is increased. It is found that these flexible modes are largely dependent on the connection parameters of the joint and the aerodynamics of the aircraft which can alter these modes. These flexible modes are a consequence of relative rotation about the yaw, pitch and roll axes which are called lead lag, twisting (pitch) and flapping modes for wing tip to wing tip flight and snaking, porpoising, and twisting (roll) modes for tip to tail connected flight. It was shown through simulation that the natural frequency and damping can be tuned specifically by changing the rotational stiffness and damping at the joint along each axis highlighting the decoupled nature of each flexible mode. In the future, when designing a meta aircraft, the designer can change the joint characteristics to achieve the desired flexible frequency and damping of all flexible modes.

Chapter 4 explored the connection flight dynamics of a meta aircraft system where the vehicles are connected wing tip to wing tip using passive magnets with a particular focus on modeling the connection event between aircraft in a practical environment. Using a 2 stage control law blending overall tracking using PID with wing tip tracking using MPC, the meta aircraft system is shown to be robust to sensor errors. On the other hand, atmospheric winds cause significant performance degradation in connection rates. There is a direct relationship between tracking performance and percent connection rates. Atmospheric

disturbances with low frequency spatial gusts at intensities found in realistic wind environments cause the largest connection performance decrease. Connection rates are relatively insensitive to axial sinusoidal disturbances, mildly sensitive to lateral disturbances and highly sensitive to vertical wind disturbances. Flying faster increases connection performance in the presence of atmospheric disturbances. Thus, a strategy to maximize connection rates is to fly straight into the wind at the maximum speed while staying away from certain spatial frequencies. If a certain spatial frequency is found turning into the wind will reduce the effect of these frequencies. Increasing the charge density of the magnet, and square magnets all cause increases in the sphere of influence which directly relates to an increase in percent connection rate. An actuator capable of propelling the magnet towards the other aircraft at $10m/s$ can increase percent connection rates by 15%.

Chapter 5 explored the control of meta aircraft in numerous configurations with a focus on the performance of different types of configurations in a realistic wind environment. A control law is formed that adequately controls meta aircraft in a variety of different configurations by using a simplified rigid body dynamics model that alters inner and outer loop gains that are dependent on the meta aircraft configuration. This control law is capable of adequately controlling meta aircraft and is sufficiently flexible to accommodate different configurations. Using this control architecture, the benefits of a meta aircraft from a stability and lift to drag performance perspective are examined. Wing tip to wing tip connected flight increases tracking performance in roll and pitch while decreasing performance in heading. When aircraft are connected, aerodynamic interactions cause a change in the overall lift to drag ratio. Wing tip to wing tip flight has the highest L/D_{avg} while tip to tail flight reduces L/D_{avg} the most.

Overall, this thesis shows that connected aircraft is practical for increasing range and endurance. Based on overall lift to drag ratio, flight dynamic modes, and connection dynamics it would be wise to connect aircraft wing tip to wing tip. Wing tip to wing tip flight has the largest increase in lift to drag ratio as opposed to tip to tail flight that decreases over L/D. All wing tip to wing tip flight dynamic modes change in a safe and stable fashion as opposed to tip to tail flight which exhibits critically damped longitudinal modes. Finally, connection dynamics for wing tip to wing tip connection is the least likely to result in failure. A tip to tail connection would involve the follower aircraft to fly in the more turbulent wake area of the leader

aircraft. Thus, it is concluded that tip to tail connected flight should be avoided unless these shortcoming can be overcome.

6.2 Future Work

The results of this dissertation have established the rich dynamic behavior of meta aircraft and show the feasibility and practicality of a meta aircraft in a realistic design setting. Many opportunities for future work, presented below, could expand upon the findings described here and help to enable the meta aircraft to become a production reality.

1. **Interaction Aerodynamics**

   The flight dynamic analysis indicates that meta aircraft configurations contain unstable spiral modes caused by aerodynamic interactions. If the interaction effect is removed, the instability is removed. This interaction model is a simple panel method lifting line model. A good area of work would be to add in a more sophisticated interaction model such as Computational Fluid Dynamics (CFD) to investigate this instability to completely characterize the aerodynamic effect of connecting aircraft.

2. **Lattice Structure Modes and Mode Shapes**

   Another topic would be to investigate the modes and mode shapes of lattice structures in all of their types ($M > N, M = N, N > M$) to see if there are any trends associated with certain configurations. In addition, it could be that certain lattice structures have unstable longitudinal modes just as the tip to tail modes.

3. **Control Law**

   The basic control mechanism uses a simplified rigid body model that picks up macroscopic effects in different meta aircraft configurations. However, there is still much room for improvement for these types of control system. In addition, no attempt was made to control asymmetric configurations which could potentially be realized when connecting a lattice configuration in flight.

4. Performance Benefit

The performance benefits shown by meta aircraft is also simply taken from a design perspective. It would be an interesting result to see if the increase in performance would outweigh the disadvantages of increase in weight associated with sensor components and connection mechanism. In addition, no effort was made to optimize the time needed to connect aircraft in flight. For some missions, where minimizing time is part of the mission, the time needed to connect in flight will need to be considered.

5. Connection Mechanism

The connection mechanism investigated here is passive magnets. An area of future work would be to change the overall connection mechanism to see if percent connection rates could be improved. Rather than using passive magnets, perhaps an electro-magnet could be used or perhaps a mechanical connection such as a probe and drogue could be used as well.

6. Connection Performance

In terms of increasing connection with existing tools, other methods may increase percent connection rates such as using larger aircraft or winglets so that the collision interface is larger. In addition, it may be possible to create a leader control law rather than focusing on the follower control law.

7. Damaged Aircraft

Trade studies were run while examining the amount of force produced during a collision. The study revealed that the largest force exerted on each vehicle occurs during connection. Namely, the magnetic force that pulls the aircraft together is so large that it is much larger than any other contact force during the connection maneuver. Future work will have to verify that the aircraft used for connection can withstand the large contact force produced by the passive magnets placed at wing tips.

8. Larger Meta Aircraft

Another topic that is worth investigating is attempting to connect meta aircraft to other meta aircraft or single aircraft to larger meta aircraft. It may be that connecting to larger meta aircraft is easier as

the meta aircraft size increases.

9. **Full Mission Scenario**

   Furthermore, simulating a full mission scenario where multiple aircraft take off, form a lattice structure, disconnect and perform a mission all has interesting challenges from an implementation perspective.

10. **Different Aircraft**

    Finally, an over-arching area of future work would be to run simulations with different aircraft models to see if overall trends hold. Perhaps larger aircraft have a different sensitivity to wind gusts and increase percent connection rates but perform terribly as a meta aircraft. In addition, it may be found that meta aircraft is better suited for micro machines on the order of a few hundred grams rather than 6 kg.

References

[1] Yoo D., Lee C., Tahk M., *Optimal Resource Management Algorithm for UAV Missions in Hostile Territories* Journal of Aerospace Engineering. 2013.

[2] *AeroEnvironment Inc.*, http://www.avinc.com/uas/small_uas/raven/ cited Sep. 19 2013

[3] *General Atomics*, http://www.ga-asi.com/products/aircraft/predator.php cited Sep. 19 2013

[4] *UAVs: The New Frontier for Weather Research and Prediction* Weatherwise News. http://www.weatherwise.org/Archives/Back%20Issues/2012/March-April%202012/UAVs-full.html cited Sep. 19 2013

[5] *Earth Science and Climate Monitoring — NASA Using Unmanned Aerial Vehicles To Eye Hurricane Power* http://www.spacenews.com/article/features/36256earth-science-and-climate-monitoring-nasa-using-unmanned-aerial-vehicles-to cited Sep. 19 2013

[6] Wieselsberger, C., *Beitrag zur Erklarun des Winkelfluges einiger Zugvogel* Zietschrift fur Flugtechik und Motoluftshiffahrt 5, 1914, pp. 225-229.

[7] Slater G., *Dynamics of Self-Spacing in a Stream of In-Trail Aircraft* AIAA Guidance, Navigation and Control Conference and Exhibit. California, USA. August 2002

[8] Weitz L., Hurtado J., *Investigating Time-Delay Effects for Multivehicle Formation Control* Journal of Aerospace Computing, Information, and Communication. Vol 5, Sep 2008

[9] Allen M., Ryan J., Hanson C., Parle J., *String Stability of a Linear Formation Flight Control System* AIAA Guidance, Navigation and Control Conference and Exhibit. California, USA 2002.

[10] Fowler J., D'Andrea R.,*Distributed Control of Close Formation Flight*, IEEE Conference on Decision and Control, Nevada, USA. Dec. 2002

[11] Gibbs J., Vlachos P., Telionis D., *Experimental Determination of Lift and Lift Distributions for Wings in Formation Flight*. AIAA Aerospace Sciences meeting and Exhibit. Nevada USA. Jan. 2005

[12] Vachon M., Ray R., Walsh K., Ennix K., *F/A-18 Aircraft Performance Benefits Measured During the Autonomous Formation Flight Project* AIAA Flight Mechanics Conference. California. 2002.

[13] Ray R., Cobleigh B., Vachon M., John C., *Flight Test Techniques used to Evaluate Performance Benefits During Formation Flight*. AIAA Flight Mechanics Conference. California. 2002.

[14] King R., Gopalarathnam A., *Ideal Aerodynamics of Ground Effect and Formation Flight* AIAA Aerospace Sciences Meeting. Nevada 2004.

[15] Seanor B., Campa G., Gu Y., Napolitano M., Rowe L., Perhinschi M., *Formation Flight Test Results for UAV Research Aircraft Models* AIAA Intelligent Systems Technical Conference Illinois. 2004.

[16] Ning S., Flanzer T., Kroo I., *Aerodynamic Performance of Extended Formation Flight* Journal of Aircraft Vol 48, No. 3,Jun 2011.

[17] Venkataramanan S., Dogan A., Blake W., *Vortex Effect Modeling in Aircraft Formation Flight* AIAA. AFM Conference TX 2003.

[18] Tandale M., Bowers R., Valasek J., *Trajectory Tracking Controller for Vision-Based Probe and Drogue Autonomous Aerial Refueling* Journal of Guidance, Control and Dynamics. Vol. 29, No. 4, Aug. 2006

[19] Mammarella M., Campa G., Napolitano M., Seanor B., Fravolini M., Pollini L., *GPS/MV based Aerial Refueling for UAVs* AIAA Guidance, Navigation and Control Conference and Exhibit. Honolulu, USA. Aug 2008.

[20] Valasek J., Gunnam K., Kimmett J., Tandale M., Junkins J., *Vision-Based Sensor and Navigation System for Autonomous Air Refueling* Journal of Guidance Control and Dynamics. Sep 2005.

[21] Nalepka J., Hinchman J., *Automated Aerial Refueling: Extending the Effectiveness of Unmanned Air Vehicles* AIAA Modeling and Simulation Technologies Conference and Exhibit. California, USA 2005.

[22] Fravolini M., Ficola A., Campa G., Napolitano M., Seanor B., *Modeling and control issues for autonomous aerial refueling for UAVs using a probe-drogue refueling system.* Aerospace Science and Technology 8 (2004) 611-618.

[23] Burns B., Major USAF *Autonomous Unmanned Aerial Vehicle Rendezvous for Automated Aerial Refueling. Thesis. Air Force Institute of Technology 2007.*

[24] Murray D., Basu A., *Motion Tracking with an Active Camera* IEEE Transactions on Patter Analysis and Machine Intelligence Vol 16. No. 5 May 1994.

[25] Goldin J., *Perching Using a Quadrotor with Onboard Sensing* PhD Thesis. Utah State University. 2011.

[26] Wenzel K., Rosset., Zell A., *Low-Cost Visual Tracking of a Landing Place and Hovering Flight Control with a Microcontroller* Journal of Intelligent Robot Systems. Aug 2009.

[27] Morris J., *Automated Spacecraft Docking using a Vision-Based Relative Navigation Sensor* Masters Thesis. Texas A&M University 2009.

[28] Ozkan B., Ozgoren M., Mahmutyazicioglu G., *Comparison of the Linear Homing, Parabolic Homing and Proportional Navigation Guidance Methods on Two-Part Homing Missile against a Surface Target.* Journal of Science 23 (1): 81-87 (2010).

[29] Yakimenko O., *Direct Method for Rapid Prototyping of Near-Optimal Aircraft Trajectories* Journal of Guidance Control and Dynamics Vol 23 No 5 Sep 2000.

[30] Evans J., Hodge W., Liebman J., *Flight Tests of an Unmanned Air Vehicle with Integrated Multi-Antenna GPS Receiver and IMU Towards a Testbed for Distributed Control and Formation Flight*, Stanford University

[31] Rysdyk R., *UAV Path Following for Constant Line-of-Sight* AIAA Conference Sep 2003 California.

[32] Richards A., How J., *Aircraft Trajectory Planning with Collision Avoidance Using Mixed Integer Linear Programming* AIAA Conference 2002.

[33] Bellingham J., Tillerson M., Alighanbari M., How J., *Cooperative Path Planning for Multiple UAVs in Dynamic and Uncertain Environments*

[34] Park S., Deyst J., How J., *A New Nonlinear Guidance Logic for Trajectory Tracking.* AIAA.

[35] Bortoff S., *Path Planning for UAVs* American Control Conference. Illinois. 2000.

[36] Ward M., Montalvo C., Costello M., *Performance Characteristics of an Autonomous Airdrop System in Realistic Wind Environments* AIAA GNC/AFM/MST/ASC/ASE 2010 Conference.

[37] Slotine J., Weiping L., *Applied Nonlinear Control*, Prentice Hall, NJ 1991 pp 209-211, pp 276-283

[38] Dunbar W., Murray R., *Model Predictive Control of Coordinated Multi-Vehicle Formations* IEEE Conference on Decision and Control March 8, 2002.

[39] Shim D., Kim H., Sastry S., *Decentralized Nonlinear Model Predictive Control of Multiple Flying Robots* IEEE. Conference On Decision and Control. Hawaii USA. Dec. 2003.

[40] Haddad W., Leonessa A., Chellaboina V., Fausz J., *Nonlinear Robust Disturbance Rejection Controllers for Rotating Stall and Surge in Axial Flow Compressors* IEEE Transactions on Control Systems Technology, Vol 7 No 3 May 1999.

[41] Krohling R., Rey J., *Design of Optimal Disturbance Rejection PID Controllers Using Genetic Algorithms* IEEE Letters 2001.

[42] Han J., *From PID to Active Disturbance Rejection Control* IEEE Transactions on Industrial Electronics Vol. 56, No. 3 March 2009.

[43] Alexis K., Nikolakopoulos G., Tzes A., *Experimental Model Preditive Attitude Tracking Control of a Quadrotor Helicopter subject to Wind-Gusts* Control and Automation Conference Morocco 2010.

[44] Vassilvitskii S.,Yim M.,Suh J., *A Complete, Local and Parallel Reconfiguration Algorithm for Cube Style Modular Robots* International Conference on Robotics and Automation, Washington DC, May 2002.

[45] White P., Zykov V., Bongard J., Lipson H., *Three Dimensional Stochastic Reconfiguration of Modular Robots* Computational Synthesis Laboratory, Cornell University, Ithaca, NY

[46] Yim M., Zhang Y., Duff D., *Modular Robots* Xerox Palo Alto Research Center (PARC) IEEE Spectrum, Feb 2002

[47] Casal A., Yim M., *Self-Reconfiguration Planning for a Class of Modular Robots* Xerox Palo Alto Research Center, Stanford University

[48] Anderson R., *Building a Modular Robot Control System using Passivity and Scattering Theory* IEEE Internation Conference on Robotics and Automation, Minneapolis, MN 1996.

[49] Leylek E., Costello M., *Benefits of Autonomous Morphing Aircraft in Loiter and Attack Missions* AIAA AFM Conference 2010.

[50] C.E.Bud Anderson. *Dangerous Experiments*. Flight Journal, pages 6572, December 2000. vii, 1, 9, 10, 11, 12, 13, 100

[51] Magill S., "Compound Aircraft Transport: Wing Tip-Docking Compared to Formation Flight", Ph. D. Dissertation, Department of Mechanical and Aerospace Engineering, Virginia Polytechnic Institute and State University. Blacksburg, VA 2002.

[52] Magill S., Schetz J., Mason W.,*Compound Aircraft Transport: A Comparison of Wing tip-Docked and Close-Formation Flight*, Aerospace Sciences Meeting and Exhibit, Jan. 2003

[53] Moore J., and Maddalon D., "Multi-Body Transport Concept", *AIAA 2nd International Very Large Vehicles Conference* May 17-18 1982, Washington, DC

[54] Aurora Flight Sciences., "Aurora's Odysseus" *Aurora Flight Sciences* Manassas, VA. 2014 [http://www.aurora.aero/Development/Odysseus.aspx] Accessed 2/13/14

[55] Noll, Brown, Perez-Davis, Ishmael, Tiffany and Gaier, *Investigation of the Helios Prototype Aircraft Mishap*. Volume I Mishap Report. NASA Headquarters. Jan 2004.

[56] Oung R., Bourgault F., Donovan M., D'Andrea R., *Feasibility of a Distributed Flight Array*, IEEE International Conference on Decision and Control, China Dec 2009.

[57] Oung R., Bourgault F., Donovan M., D'Andrea R., *The Distributed Flight Array*, IEEE International Conference on Robotics and Automation, Alaska, USA. May 2010.

[58] Roberson R., *Dynamics of Multibody Systems* Springer-Verlag 1992.

[59] Shabana A., *Flexible Multibody Dynamics: Review of Past and Recent Developments* Multibody System Dynamics. 1: 189-222, 1997.

[60] Szidarovszky F., Bahill T. A., *Linear Systems Theory* Second Ed. CRC Press LLC Boca Raton, FL 1998

[61] Narendra K., George K., *Adaptive Control of Simple Nonlinear Systems using Multiple Models*. Proceeding of the American Control Conference, AK May 8th, 2002.

[62] Narenda K., Annaswamy A., *A New Adaptive Law for Robust Adaptation Without Persisten Excitation* IEEE Transactions on Automatic Control Vol. AC-32, No. 2 Feb 1987.

[63] Chowdhary G., Kingravi H., How J., Vela P., *Nonparametric Adaptive Control of Time-varying Systems using Gaussian Processes* MIT. Aerospace Control Laboratory: Technical Reports 2013.

[64] Chowdhary G., *Concurrent Learning for Convergence in Adaptive Control without Persistency of Excitation* PhD Thesis, Georgia Institute of Technology. December 2010.

[65] Chowdhary G., Wu T., Cutler M., How J., *Rapid Transfer of Controllers between UAVs Using Learning-Based Adaptive Control* Laboratory of Information and Decision Systems and with Dept. of Aeronautics and Astronautics at the Massachusetts Institute of Technology, Cambrige MA 2013.

[66] Hassan K., Chowdhary G., Vela P., Johnson E., *A Reproducing Kernel Hilbert Space Approach for the Online Update of Radial Bases in Neuro-Adaptive Control* Neural Networks and Learning Systems, IEEE Transactions on Vol. 23 , Iss. 7 2012.

[67] Liu C., Li C., He Z., *Adaptive Control of a Morphing Aircraft through Updating the Number of Actuators.* AIAA GNC Conference Minneapolis, MN Aug. 2012.

[68] Wang L., *Stable Adaptive Fuzzy Control of Nonlinear Systems* IEEE Transactions on Fuzzy Systems. Vol 1. No 2. 1993.

[69] Yang Z., Blanke M., Verhaegen M., *Robust Control Mixer Method for Reconfigurable Control Design using Model Matching* IET Control Theory Appl., Vol 1., No. 1, January 2007.

[70] Richter Jan., *Reconfigurable Control of Nonlinear Dynamical Systems* Springer 2011.

[71] Siddigui Bilal., *Reconfigurable Flight Control for Fighter Aircraft Using MPC: Fault Tolerant Flight Control Design for Aircraft Utilizing Robustness Characteristics of Model Predictive Control* VDM Verlag Dr. Muller 2010.

[72] Enns R., Si J., *Helicopter Flight-Control Reconfiguration for Main Rotor Actuator Failures* Journal of Guidance Control and Dynamics. Vol 26. No 4. Aug 2003.

[73] McLean D., Asiam-Mir S., *Reconfigurable Flight Control Systems* University of Southampton, UK

[74] Marzat J., Piet-Lahanier H., Damongeot F., Walter E., *Model-based fault diagnosis for aerospace systems: a survey* Journal of Aerospace Engineering, JAERO1217

[75] Zhang Y., Jian J., *Bibliographical review on reconfiguration fault-tolerant control systems.* Annual Reviews in Control 32 (2008) 229-252.

[76] Vetter T., Wells S., Hess R., *Designing for damage-robust flight control design using sliding mode techniques* Proceedings of the Institution of Mechanical Engineers, Part G: Journal of Aerospace Engineering. 2003

[77] Hess R., Wells S., *Sliding Mode Control Applied to Reconfigurable Flight Control Design* AIAA Aerospace Sciences Meeting. Reno, Nevada Jan 2002.

[78] Wells S., Hess R., *MIMO Sliding Mode Control for a Tailless Fighter Aircraft, An Alternative to Reconfigurable Architectures* Dept. of Mechanical and Aeronautical Engineering. University of California.

[79] Ahmad H., Young T., Toal D., Omerdic E., *Control Allocation in Transport Vehicles* Part G: Journal of Aerospace Engineering.

[80] Wendlandt J., *Control and Simulation of Multibody Systems* PhD Thesis. Mechanical Engineering. University of California at Berkeley. 1997.

[81] Jung D., "Hierarchical Path Planning and Control of a Small Fixed-Wing UAV: Theory and Experimental Validation", Ph.D. Dissertation, Department of Aerospace Engineering, Georgia Institute of Technology, Atlanta, GA 2007

[82] Jung D., *Hierarchical Path Planning and Control of a Small Fixed-Wing UAV: Theory and Experimental Validation* PhD Thesis, Georgia Institute of Technology. December 2007.

[83] Brumbaugh R., *An Aircraft Model for the AIAA Controls Design Challenge* NASA Contractor Report, California, Dec. 1991.

[84] Etkin B., *Dynamics of Atmospheric Flight*, Dover, New York, 2000, pp. 121-152

[85] Phillips W., *Mechanics of Flight 2nd Edition* John Wiley & Sons, Inc 2010. pp 715-952.

[86] Anderson D., *Fundamentals of Aerodynamics 4th Edition*, McGraw Hill Series. 2007. pp 307-316,342-348

[87] Bertin J., Smith M., *Aerodynamics for Engineers 3rd Edition*, Prentice Hall. 1998, pp 291-311

[88] Selig M., *Modeling Full-Envelop Aerodynamics of Small UAVs in Realtime* AIAA Atmospheric Flight Mechanics Conference. 2010. Toronto, Ontario, Canada

[89] Anderson J., Corda S., Van Wie D., *Numerical Lifting Line Theory Applied to Drooped Leading-Edge Wings Below and Above Stall* Journal of Aircraft Vol 17. No. 12 Article No. 80-4129 1980.

[90] Akoun G., Yonnet J., *3D Analytical Calculation of the Forces Exerted Between Two Cuboidal Magnets*, IEEE Transaction on Magnetics, Vol, Mag-20, No. 5, Sep 1984

[91] Allag H., Yonnet J., *3-D Analytical Calculation of the Torque and Force Exerted Between Two Cuboidal Magnets*, IEEE Transactions on Magnetics, Vol 45, No. 10, Oct 2009

[92] Agashe J., Arnold D., *A Study of scaling and geometry effects on the forces between cuboidal and cylindrical magnets using analytical force solutions*, Journal of Physics D: Applied Physics, April 2008.

[93] Bobbio S., *Electrodynamics of Materials: Forces, Stresses, and Energies in Solids and Fluids* Academic. California, USA. 2000

[94] Melcher R.,*Continuum Electromechanics* Cambridge, MA MIT Press. p 57. 1981

[95] Wagner B., Benecke W., *Magnetically driven microactuators: design considerations* Microsystems Technologies vol 90 ed H Reichl (Berlin:Springer) p 838. 1990

[96] Goyal, S., Pinson, E., and Sinden, F.,*Simulation of Dynamics of Interacting Rigid Bodies Including Friction 1: General Problem and Contact Model* Engineering with Computers, Vol. 10, No. 3, 1994,pp. 162-174.

[97] Beyer E., Costello M., *Measured and Simulated Motion of a Hopping Rotochute*, Journal of Guidance, Control, and Dynamics, AIAA Feb. 2009.

[98] Beyer E., Costello M., *Performance of a Hopping Rotochute* International Journal of Micro Air Vehicles. Vol 1. No 2. 2009.

[99] *The Weather Research and Forecasting Model*, http://www.wrf-model.org cited Jul. 14 2012

[100] Beal T., *Digital Simulation of Atmopsheric Turbulence for Dryden and von Karman Models* Journal of Guidance, Control and Dynamics. Vol 16, No. 1, Jan-Feb 1993.

[101] Gage S., *Creating a Unified Graphical Wind Turbulence Model from Multiple Specifications* AIAA Modeling and Simulation Technologies Conference and Exhibit. 11-14 Aug. 2003 TX.

[102] Brier G., *The Statistical Theory of Turbulence and The Problem of Diffusion in the Atmosphere*. Journal of Meteorology U.S. Weather Bureau, Washington, Feb 1950.

[103] Barr N. et al., *Wind Models for Flight Simulator Certification of Landing and Approach Guidance and Control Systems* Boeing Commercial Airplane Company. National Technical Information Service, U.S. Department of Commerce. Springfield, VA. 1974.

[104] Lin Y., Li Q., Su T., *Application of a new wind turbulence model in predicting motion stability of wind-excited long-span bridges* Journal of Wind Engineering and Industrial Aerodynamics. 49. 1993.

[105] Batchelor, G.K. *The Theory of Homogeneous Turbulence*, Cambridge University Press, London, England, 1953 pgs 14-39

[106] Shinozuka M., Jan C., *Digital Simulation of Random Processes and its Applications* Journal of Sound and Vibration. Vol 25. pgs 111-128. 1972.

[107] Strang G., *Linear Algebra and Its Applications* 4th Ed pgs 318-322 Thomson Brooks/Cole. 2006. pgd 318-322

[108] Ciornei M., Diaconescu E., Glovnea M., *Experimental Investigations of Wood Damping and Elastic Modulus* Universitatea Stefan Cel Mare, Romania. 2009.

[109] Russell D., *Bending Modes, Damping, and the Sensation of Sting in Baseball Bats* Engineering of Sport 6, Internation Sports Engineering Conference 2006.

Carlos J. Montalvo

MONTALVO was born in Pensacola, FL and grew up in Alpharetta, GA only 45 minutes away from Georgia Institute of Technology. In 2009 he received a Bachelors of Science Degree in Aerospace Engineering from Georgia Tech and went on to obtain his Masters in Flight Mechanics and Controls in August of 2010. He has worked in numerous internships including Raytheon Missile Systems, AREAI-Inc and Earthly Dynamics Corporation. His technical interests include control and flight dynamics of novel aerial systems.